UNIVERSITÀ DEGLI STUDI DI TRENTO

Doctoral School in Civil, Environmental and Mechanical Engineering

Topic 3. Modelling and Simulation

Stefano Signetti

Computational models for impact mechanics and related protective materials and structures

2017 - Doctoral thesis

UNIVERSITY OF TRENTO - Italy
Department of Civil, Environmental
and Mechanical Engineering

Doctoral School in Civil, Environmental and Mechanical Engineering
Topic 3. Modelling and Simulation - XXIX cycle 2014/2016

Doctoral Thesis - June 2017

Stefano Signetti

Computational models for impact mechanics and related protective materials and structures

Supervisors
Nicola M. Pugno, University of Trento

Cover image: View of an orbital debris hole made in the panel of the Solar Max experiment (credits: NASA).

University of Trento
Doctoral School in Civil, Environmental and Mechanical Engineering
http://web.unitn.it/en/dricam
Via Mesiano 77, I-38123 Trento
Tel. +39 0461 282670/2611 - *dicamphd@unitn.it*

勝って兜の緒を締めよ

Katte kabuto no o wo shimeyo
After the victory, tighten the helmet
(Japanese proverb)

Acknowledgements

I would like to thank my PhD supervisor, Prof. Nicola Pugno, for the continuous encouragement, for the hard training and for the many wide-spectrum and fruitful opportunities of collaborations with top level research groups and scientist during these years. These collaborations were fundamental to reach important scientific results as well as for my professional growth as a scholar.

I thank the external referees, Prof. Seunghwa Ryu (Korean Advanced Institute of Science and Technology, Daejeon, South Korea) and Dr. Ettore Barbieri (Queen Mary University of London, United Kingdom) for the time dedicated to the review of this thesis and for their valuable and constructive comments which leads to several improvement to this outcome.

I also gratefully acknowledge the financial support from the European Union's Seventh Framework Programme FP7 (project BIHSNAM, "Bio-Inspired Hierarchical Super Nanomaterials", grant agreement nr. 279985, p.i. Prof. Nicola Pugno).

Trento, 19th June 2017

Stefano Signetti

Summary

The mechanics of impacts is not yet well understood due to the complexity of materials behaviour under extreme stress and strain conditions and is thus of challenge for fundamental research, as well as relevant in several areas of applied sciences and engineering. The involved complex contact and strain-rate dependent phenomena include geometrical and materials non-linearities, such as wave and fracture propagation, plasticity, buckling, and friction. The theoretical description of such non-linearities has reached a level of advance maturity only singularly, but when coupled -due to the severe mathematical complexity- remains limited. Moreover, related experimental tests are difficult and expensive, and usually not able to quantify and discriminate between the phenomena involved. In this scenario, computational simulation emerges as a fundamental and complementary tool for the investigation of such otherwise intractable problems. The aim of this PhD research was the development and use of computational models to investigate the behaviour of materials and structures undergoing simultaneously extreme contact stresses and strain-rates, and at different size and time scales. We focused on basic concepts not yet understood, studying both engineering and bio-inspired solutions such as those reported in the following.

Multilayer composite armours (e.g., Kevlar®-based) are commonly employed for impact protection thanks to their high toughness per unit mass. Looking for possible improvements to the current armours design, we studied, through non-linear finite element method (FEM) impact simulations, the role of different multilayer arrangements in terms of adhesive interaction and stacking sequence. Among the most important results, we demonstrated how the addition of layer is not always beneficial, leading in some cases to a decrease in the specific energy absorption of the target. The properties of the inter-layer adhesive are responsible of this behaviour, affecting the target deformation, fracture, and fragmentation. As a consequence, optimal adhesive properties emerge for maximizing the protective capability of the armour. Simulation on multilayers, graded in terms of strength and stiffness, confirms the effectiveness of common solutions in natural armours, having progressively stiffer and stronger materials towards the impact front face. At last, the target thickness compaction is shown to be able to further increase the impact protection capability, in agreement with the scaling of material strength predicted by the Linear Elastic Fracture Mechanics. As validation of the used approaches in these studies, a numerical-experimental-analytical comparison is also proposed for each case.

The above mentioned concepts were extended and investigated also for two-dimensional (2D) materials at the nanoscale. For this purpose, a continuum FEM model was developed and calibrated on *ab initio* impact simulations on single layers of graphene and hexagonal boron-nitride (h-BN), allowing to calculate the intrinsic impact strength of these 2D materials. Implementing in the model surface effects -mainly van der Waals interactions between the layers- which become predominant at the nanoscale, we were able to perform simulation on few-layer graphene, h-BN and hybrid multilayers, finding good agreement with *ab initio* simulations and to investigate the scaling of the energy absorption across dimensional scales. Thanks to this solution it is possible to treat also microscopic areas at an acceptable computational cost, thus overcoming the intrinsic limitations of atomistic simulations.

As 3D structured evolution of 2D membranes, we investigated the mechanics of hollow aerographite tetrapodal networks, whose extremely high porosity and, consequently, outstanding specific strength and stiffness make them ideal candidate for the realization of lightweight composite for impact protection from small fragments. Our simulations demonstrate how the non-linear constitutive response of single tetrapods, with reversible deformation even at high compressive strain levels, is governed by the formation of buckling hinges in the hollow tubular joints or along the arms of the tetrapods. The constitutive behaviour was generalized for tetrapods of different geometry and size scale, allowing the modelling of networks of different densities subjected to compressive loads. Comparison with *ab initio* microscopy experiments confirms the validity of the approach.

Finally the mechanical behaviour of modified honeycomb structures made of a metallic alloy subjected to compressive crushing and experiencing yielding, elastic-plastic instability, and fracture is studied through numerical simulations. These structures were realized by substituting the joint between the walls of the traditional honeycomb with hollow cylinders of variable radius, whose geometry can be optimized in order to maximize the specific energy absorption of the cellular structure. Optimal geometrical configuration emerges and the results are in good agreement with compression experiments. In principle, these obtained structures could be designed and realized, thanks to the proposed numerical model, also with other materials and at different size scale.

Papers

The main results presented in this thesis are part of the following publications in international journals:

1. S. Signetti, N.M. Pugno. Evidence of optimal interfaces in bio-inspired ceramic-composite panels for superior ballistic protection. *Journal of the European Ceramic Society*. 34:2823-2831, 2014;

2. S. Signetti, N.M. Pugno. New frontiers in modeling and design of bio-inspired armors. *Frontiers in Materials*. 2:17, 2015;

3. Q. Chen, Q. Shi, S. Signetti, F. Sun, Z. Li, F. Zhu, S. He, N.M. Pugno. Plastic collapse of cylindrical shell-plate periodic honeycombs under uniaxial compression: experimental and numerical analyses. *International Journal of Mechanical Sciences*. 111:125-133, 2016;

4. S. Signetti, F. Bosia, N.M. Pugno. Computational modeling of the mechanics of hierarchical materials. *MRS Bulletin*. 41:694-699, 2016;

5. R. Meija, S. Signetti, A. Schuchardt, K. Meurisch, D. Smazna, M. Mecklenburg, K. Schulte, D. Erts, O. Lupan, B. Fiedler, Y.K. Mishra, R. Adelung, N.M. Pugno. Nanomechanics of individual aerographite tetrapods. *Nature Communications*. 8:14982, 2017;

6. S. Signetti, N.M.Pugno. Impact mechanics of multilayer composite armours: analytical modelling, FEM numerical simulation, and ballistic experiments. *To be submitted*;

7. S. Signetti, S. Taioli, N.M. Pugno. Hybrid 2D materials armours. *To be submitted*.

Contents

List of Figures

List of Tables

Chapter 1

Introduction

1.1 Armours and technology

The protection of structures and devices from the penetration high-energy impacting masses is still a challenge for theoretical research, as well as relevant in several areas of applied technology, such as materials science and engineering, automotive, aerospace, and defence. For example, spacecrafts are commonly exposed during their operation to hypervelocity collisions of micrometeoroids or orbital debris (velocities $\geq 7-8\,\mathrm{km/s}$) [14], leading to surface degradation, on-board instrumentation failures, up to complete perforation and structural damage. Other important requirements in space structures are an extreme resilience of vital systems, since multiple faults are not allowed in space mission (Figure 1.1), and the limit of the overall mass due to related transportation issues and costs. These engineering targets are always in competition, with the result that a compromise with the acceptable level of risk of failure must be taken. Thus the objective does not limit to the mere maximization of protection, which would be straightforwardly achievable with a massive armour.

For some decades, the answer to these tasks has been -and still largely is- the adoption of composite materials [15, 16] based on the combination of synthetic fibres (e.g., Kevlar®, Dyneema®) and thermoset resin, which have allowed to effectively reach protection levels and low weights previously unimaginable with metallic targets. However the ageing and degradation of these materials, especially in extreme environments, must be properly assessed [17, 18]. When dealing with high penetrating projectiles, an hard ceramics front layer may be also employed: impactors are first blunted and worn down by the ceramic which also spreads the load over a larger area; then the composite tough backing layers absorbs the residual kinetic energy by fibre/matrix failure and delamination [19–22]. Nowadays, in the era of nanomaterials we are moving towards 2D materials, like graphene, coupling high resistance [23] and flaw tolerance at the nanoscale [24, 25], which could represent a breakthrough in protection levels [12, 26]. Complementary or alternatively,

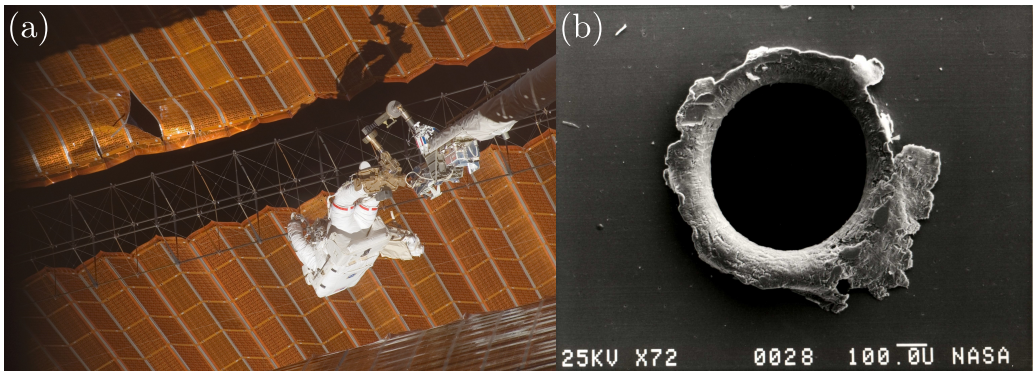

Figure 1.1: Damage by micrometeoroid impact (Credits: NASA Orbital Debris Program Office). (a) Astronaut Scott Parazynski during extravehicular activity (EVA) on 3rd November 2007 to make a critical repair on a perforated Solar Array Wing of the International Space Station. During the spacewalk, the astronaut also cut a snagged wire risking 100 V electricity. (b) Image of an hole by orbital debris in a panel of the Solar Max experiment. The impact craters on the aluminum exterior ISS handrails for spacewalks may have particularly sharp edges, representing a real risk of damage to the gloves of pressure suits. A new generation of composites based on bio-inspired and 2D nanomaterials will be fundamental for reducing risk of fatal hazard in long human space missions, e.g. to Mars.

the same goal may be pursued through smart structural solutions to be employed even with traditional materials above mentioned, with all advantages that this option implies in terms of consolidated manufacturing techniques and costs. Nature, having worked over the ages for optimizing defensive mechanisms against predators attacks or shock loads, is one of the most inspiring sources in this sense [27].

Upon impact, several complex physical phenomena take place: elastic–plastic deformation and wave propagation, fracture and fragmentation, heat generation (by yielding and friction), the change of material properties due to strain-rate effects up to phase transformation. Their occurrence and magnitude depend on the impact velocity that may be very low or up to extreme values ($\geq 3\,\mathrm{km/s}$ for hypervelocity impact), with increasing challenges for armours protective capabilities as well as for their accurate modelling and design. The theoretical description of the basic aspects of impact mechanics [28–31] has reached a level of advanced maturity only singularly but when coupled, due to the severe mathematical complexity, it is in a sort of stalemate. With high speed calculators and the development of computational methods (e.g., finite element method, meshless methods), simulation [32] has become the favourite design tool, allowing optimization studies. The technological and economic limits in large scale production of nanomaterials and the difficulties in their manipulation or in their structural arrangement into complex bio-inspired structures require a systematic and reliable design process able to provide

a tentative optimum. The large variety of parameters to be considered in the study of toughening mechanisms in biological materials due to their heterogeneity, the numerous levels of hierarchy, and the complexity of the constitutive laws (also strain-rate dependent) make experimental tests scarcely viable [33]. Moreover, with mere experiments is nearly impossible to investigate the whole design space. The traditional stand-alone experimental approach for armour design according to the philosophy "add material until it stops" it is not viable any more, since the addition of mass can result in even suboptimal configuration [11]. In this scenario, computational models can be powerful tools helping the design of new energy absorbing materials. Although important progress has been made in the past decades to simulate damage and failure phenomena taking place at impact, penetration, and fragmentation, much work remains to be done. The advent of nanomaterials and bio-inspiration is further questioning the capabilities of these tools and also stimulates the research in this field.

1.2 Biological armours

Many current-day animals possess armour, whose scope is to provide defence from the puncturing teeth of their predators. These include mammals (e.g., armadillo and pangolin [34]), reptiles (e.g., alligators, crocodiles, and turtles [2]), and various fishes [35, 36]. Despite the wide variation in the structure and materials composition, there are various common aspects: the armour is generally composed of discrete rigid plates connected to the body and to each other by soft collagen fibrils and muscular tissue, which serve as back substrate [27]. This solution is able to provide effective protection together with the required flexibility [37] for locomotion.

Among these, the dermal structure of the *Arapaima gigas* (Figure 1.2a) is one of the most widely studied bioarmours in literature due to its unique characteristics [35, 36]. Their scales are composed by inner layers of mineralized collagen fibrils arranged in lamellae forming a Bouligand pattern [38] and by a highly mineralized outer layer that both dissipate energy by fracture mechanisms. There are at least three different orientations of collagen layers providing a certain grade of isotropy in the tensile and bending response. Tensile tests of notched *Arapaima gigas* scales [35] have shown how the layers of collagen fibrils separates with some of them that fracture, while others remain intact. This represents an effective crack bridging, another extrinsic toughening mechanism [39] which is widely exploited in many cross-ply fibre reinforced polymers [40].

Other kind of common toughening mechanism rely on the optimized hierarchical structure. For example the mineral layer of alligator scales [41] relies on the presence of voids with optimal disposition and density that are able to deviate the crack pattern thus increasing the toughness. Probably the most known mechanism of this type belongs to the nacre [42]. Its microstructure (Figure 1.2b) is mostly made of microscopic ceramic tablets densely packed and bonded together by a thin layer of biopolymer. Material properties

are properly calibrated and coupled in synergy with the structural arrangement, so that the crack propagation is constricted within the polymer phase by continuing changing the direction of propagation. When the crack has completely pass through a further reservoir of toughness is available due to the interlocking between the lamellae. This hierarchical structure coupled with material of different characteristics (e.g., stiffness) is another common characteristic in natural structures and has been demonstrated to be the key for such extreme toughness and flaw tolerance [43]. The importance of material mixing has been demonstrated to be fundamental also through numerical simulations [44] showing that hierarchy per se is not beneficial for increasing strength and toughness, but must be necessarily coupled with material heterogeneity within the same hierarchical lever or at different scales. These concepts have been widely exploited for the realization of bio-inspired composites with enhanced toughness [1].

The effective protection of these armours does not rely only on the optimized hierarchical microstructure. Also the macroscopic arrangement has an important role especially in mitigating the pain in the inner tissues of the animal. The scale-based structure has been implemented in different animals to provide the required flexibility with different variants. In the armadillo carapace [45] the elements are hexagonal in the pectoral part and not ovelapped, with collagen fibres connecting to the adjoining osteoderms. In the alligator gar (*Atractosteus spatula*) and Senegal bichir (*Polypterus senegalus*), the bony scales have some overlap and the exposed (non-overlapped) regions are covered with hard ganoine [41]. In the red-eared slider turtle (*Trachemys scripta elegans*) sutures forming a zig-zag pattern ensure a minimum of non-bone area and of flexibility [46]. This hierarchical sutures (Figure 1.2c) provide a further way for energy dissipation through local deformation and friction, and could represent a further source of optimization in bio-inspired armours [3]. The analysis of scales subjected to transverse compression and the evaluation of the distribution of stresses have been carried out in a fundamental work by Vernerey and Barthelat [47]. They concluded that the scale mechanism provide a strain-stiffening mechanism being a strategy to prevent structural damage and failure. Comparing different scales, ligament rigidity, and grade of overlap they demonstrated how it is possible to obtain a wide spectrum of constitutive responses, optimized for the specific load. It is interesting to mention that the scale armour concept has been used since antiquity from humans. Individual elements (in metal or leather) sewn or laced to a backing in a form of overlapping rows resembling the scales of a fish/reptile have been extensively used by Roman, Bizantine, and Japanese warriors.

Different kind of loads corresponds to different structures. While against puncturing predators teeth and high concentrated loads the presence of voids generally represents a weakness in the armour, a porous structure may be beneficial under distributed loads, allowing high energy dissipation through the activation of buckling deformation mechanisms in the struts of the lattice. This solution is particularly frequent in non-animal armours where the problem of flexibility and armour ergonomics (e.g., thickness) is of

second importance. A meaningful example is the hierarchical structure of the foamy peel of the Pomelo fruits (*Citrus maxima*) [4] that, although their mass of 1 to 2 kg, are able to withstand impact forces resulting from falls of over 10 meters ($\approx$ 100-200 J) without damage. The fruit toughness is due to the graded hierarchical fibre-reinforced composite foam (Figure 1.2d). The foam's struts, which are cells from the biological point of view, consists of liquid-filled cores and shells (cell walls) with relatively high strength. Recently an effective aluminum-based cast composite inspired by this structure has been proposed [5].

It emerges that when dealing with bio-inspired armours, complex architectural geometries and multiscale fracture and instabilities phenomena may arise through the different hierarchical levels. These must be properly model in order to achieve reliable predictions on their behaviour ad on their protective capability and to perform optimization analyses as well. In the next section computational models to describe the mechanics of hierarchical material for armours and to model impact phenomena at different size scales are discussed.

1.3 Computational methods

A clear understanding of the constitutive behaviour of biological hierarchical material presented in the previous section and of their structural arrangement -or of their bio-inspired engineered counterpart as well- is fundamental for their implementation in an impact simulation model. Computational methods for the characterization of hierarchical materials and for the modelling of their their impact mechanics need to span the various size and time scales of the problems involved. These can be divided schematically into three broad categories:

1. nanoscale methods such as density functional theory and molecular dynamics, to achieve characterization of the basic one-dimensional (1D) and two-dimensional (2D) constituents of hierarchical composites and evaluate the role of defects at this scale;

2. micro-/meso-scale fibre bundle model, lattice-spring model, discrete and meshless methods to reconstruct the role of hierarchy and material mixing in characteristic mechanical properties of composites, also including statistics;

3. meso- and macro-scale finite element methods and discrete/meshless methods to model complex mechanical problems at the continuum level in solids.

Figure 1.3 depicts the overall scenario of computational methods in mechanics for an ideal multiscale characterization of materials for impact analysis. The methods are here briefly discussed in the following subsections.

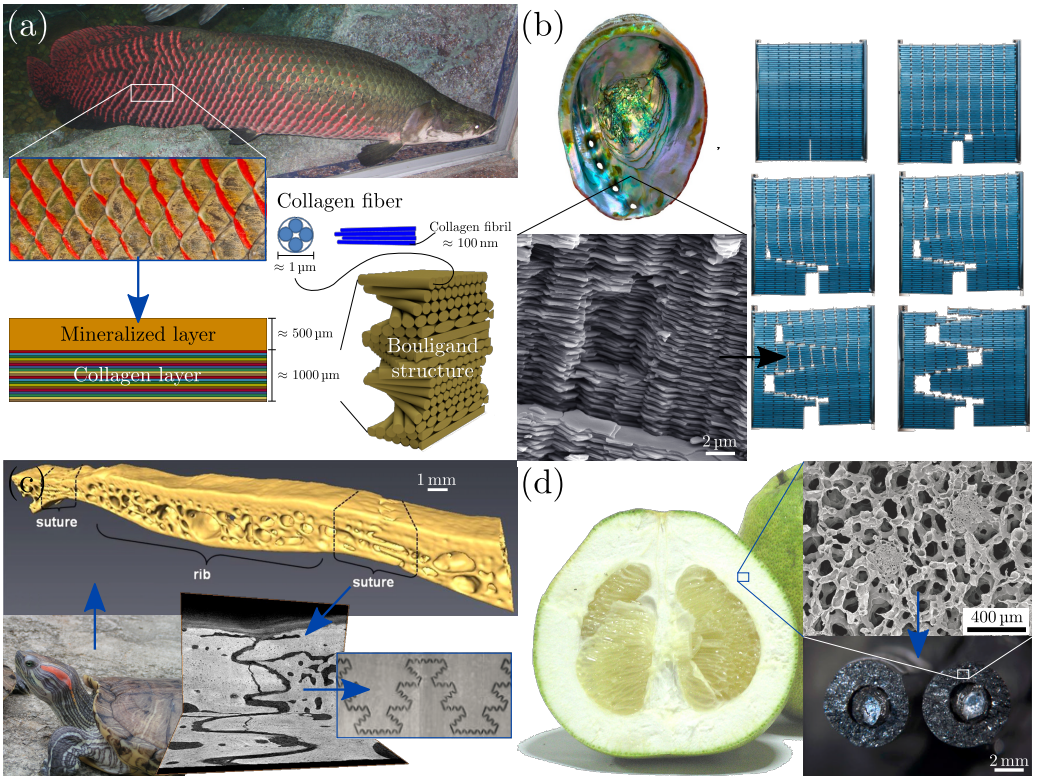

Figure 1.2: Examples of natural armours and energy absorbing structures. (a) Multilayer and hierarchical structure of the *Arapaima gigas* scales. (b) Block microstructure of the nacre and example of bio-inspired composite produced via additive manufacturing showing extreme toughness a flaw-tolerance characteristics. Cracks follow a long path through the specimen thus dissipating large amounts of energy (image adapted from ref. [1]). (c) Red-eared slider turtle (*Trachemys Scripta Elegans*) outer shell showing zig-zag suture between adjacent non-overlapped scales and example of bio-inspored hierarchical suture interface. Micro-CT image adapted from ref. [2], image of hierarchical artificial interface adapted from ref. [3]. (d) Hierarchical foamy peel of the Pomelo (*Citrus Maxima*) with an example of aluminum-based Pomelo inspired composite. SEM image of the foam adapted from ref. [4], image of the composite adapted from ref. [5].

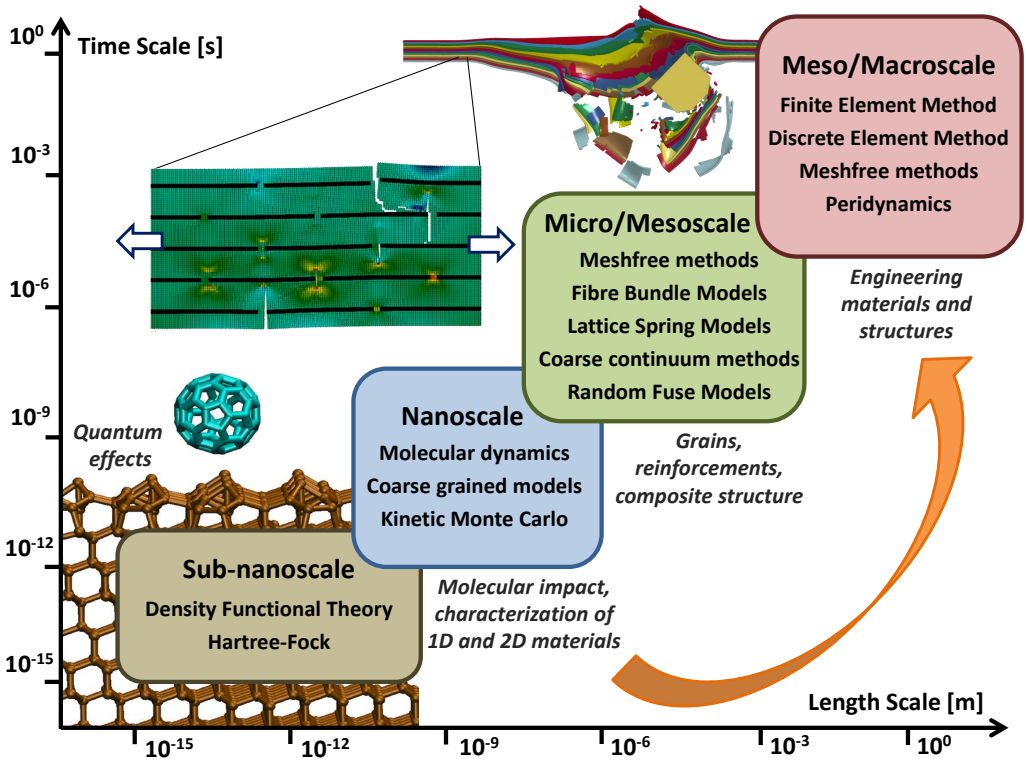

Figure 1.3: Computational approaches to perform multiscale characterization of hierarchical biological and bio-inspired materials for application in armours and to model impacts at different scales. Regions of applicability in spatial and time scales are indicated. Characteristic simulation are shown for the three main dimensional scales: (1) nanoscale DFT simulation of graphene production by supersonic beam epitaxy of a fullerene molecule (image taken and adapted with permission under CC-BY license from ref. [6]), (2) mesoscale hierarchical lattice spring model (HLSM) simulations to investigate the tensile and fracture properties of a matrix embedding rigid inclusion (images taken and adapted with permission under CC-BY license from ref. [6]), and (3) macroscale FEM impact simulation of a steel fragment penetrating a Kevlar®-based multilayer composite armour.

1.3.1 Atomistic simulations

The employment of nanomaterial, such as carbon nanotubes or graphene flakes, in hierarchical bio-inspired composites requires the full understanding of the mechanical behaviour starting from the lowest dimensional level (Figure 1.4). Molecular dynamics (MD) is a simulation technique that consists of numerically solving the classical Newton's equation of motion for a set of atoms, which are characterized by their position, velocity, and acceleration. After the definition of the initial conditions of the system (initial temperature, number of particles, density, time steps, etc.) the initial equilibrium of the system is found and then the perturbation to be studied is introduced into the system. Each atom is considered as a classical particle that obeys Newton's laws of mechanics in relation to the interaction with other atoms which are defined by the so called interatomic potentials (or force fields) that describe attractive and repulsive forces in between pairs or larger groups of atoms [48]. Potentials may be defined at many levels of physical accuracy; those most commonly used are based on molecular mechanics which can reproduce structural and conformational changes but usually cannot reproduce chemical reactions. When finer levels of detail are needed, potentials based on quantum mechanics (density functional theory, DFT) are used; some methods attempt to create hybrid classical/quantum potentials where the bulk of the system is treated classically but a small region is treated as a quantum system, usually undergoing a chemical transformation.

DFT framework, based on quantum theories of electronic structure, is currently the most commonly employed quantum mechanics method, which has evolved into a powerful tool for computing electronic ground-state properties of a large number of nanomaterials. The entire field of DFT method relies on the theorem that the ground-state energy of a many-electron system is a unique and variational functional of the electron density, and this conceptual proposal is implemented in a mathematical form to solve the Kohn–Sham (KS) equations. Due to the level of complexity the use of this method, the computational cost limit the analyses to systems of few atoms. A further method to overcome system size limitation called density functional tight binding (DFTB) consists of a series of models that are derived from a Taylor series expansion of the KS-DFT total energy [49]. The basic advantage is that the terms appearing in the total energy expression are parametrised to reproduce accurately high-level electronic structure calculations for several different bonding conditions and can be calculated in advance, saving then in computational cost (up to about 2 orders of magnitude) [50]. The DFTB method has been applied to study large molecules (e.g. biomolecules), clusters, nanostructures and condensed-matter systems with a wide range of elements.

Atomistic method does not limit to the characterization of mechanical properties of one- and two-dimensional materials [51]. Impact-like phenomena such as the graphene synthesis via C_{60} supersonic beam epitaxy have been investigated via DFT [52] (Figure 1.3) while with MD it is possible to perform simulation of the impact of even microscale projectiles on graphene sheets [12, 53].

1.3.2 Models for predicting multiscale properties of hierarchical materials

Various multiscale models have been developed to capture the mechanisms involved in the optimization of global material mechanical properties beginning from nanoscale. One example is represented by the so-called fibre bundle models (FBM) [54] which are particularly appropriate for the simulation of fibrous materials, often occurring in biomaterials as seen in Section 1.2. With these approach material structure at a certain size scale is modelled as a network of fibres arranged in parallel (same level) and in series (different levels) subjected to uniaxial tension, with statistically Weibull-distributed yield and fracture strengths or strains. Usually, an equal-load-sharing hypothesis is adopted [54], while when fibres fracture stresses are redistributed uniformly among the remaining in the bundle. Heterogeneous media are modelled by assigning different mechanical properties the fibres of each bundle. A hierarchical extension is represented by the hierarchical fibre bundle model (HFBM) [8], whereby the input mechanical behaviour of a subvolume or "fibre" at a given hierarchical level is statistically inferred from the average output deriving from reiterated simulations at the lower level, down to the lowest hierarchical level (Figure 1.4). Results from this and other numerical implementations of HFBM show that specific hierarchical organizations can lead to increased damage resistance (e.g., self-similar fibre reinforced matrix materials) or that the interaction between hierarchy and material heterogeneity is fundamental, since homogeneous hierarchical bundles do not display improved properties [44]. The effect of defects at the different scale levels can also be accounted for.

Similar approaches, appropriate for 2D or 3D simulations, are the lattice spring models (LSM) or random fuse models [55], which provide a continuum description of the media through a network of discrete elements (springs). These have been used to simulate plasticity, damage propagation, and statistical distributions of "avalanches" of fracture events in heterogeneous materials [55]. The hierarchical lattice spring model (HLSM), extends the classical LSM [6] (Figure 1.3). Other analytical theories such as the quantized fracture mechanics (QFM) [56] or atomistic methods such as MD can be integrated with these multiscale approaches, for instance, to determine constitutive laws at the lower scale as a function of atomic structure, defect content, or molecular organization.

Both theoretical and numerical models have shown that reinforcement organization in biological or bio-inspired composite materials can increase damage tolerance, avoiding direct crack path propagation and drastically improving the global response. Studies have focused on the influence of the structure, reinforcement shape, aspect ratio, dispersion, organization, and of mechanical properties of the constituents at various scale levels, iteratively deriving higher scale mechanical properties from lower ones, until a global material response is obtained [57]. The combined multiscale use of different computational techniques such as HFBM and HLSM has also proved to be successful in reproducing the macroscopic behaviour of artificial nanocomposites such as gelatin-graphene oxide fibres [58]. Mesoscale models allow the design of composite materials exhibiting tailored

fracture properties, drawing inspiration from mineralized biological composites [59].

Another common property of biomaterials that can be easily studied been studied and simulated is the self-healing and its effects on the elastic, fracture, and fatigue properties of materials. Self-healing can be incorporated in HFBM/HLSM models by replacing fractured fibres with intact ones (simulating the process of healing) with custom mechanical properties, volume fractions, replacement rates, and locations as damage evolves during simulations. The main control parameter is the "healing rate" defined as the ratio of the number of healed and fractured fibres in a given fixed time interval. Both "distributed" and "local" healing processes can be simulated, in case fractured fibres are replaced either over the whole structure or at specific locations where damage is accumulated, respectively [60].

Thus, HFBM and HLSM are useful in providing advanced constitutive response, including fracture, damage, and self-healing, to be used as input in finite element simulations that can, therefore, be limited at the upper scale (Figure 1.3). Thus, a series of parametric studies, each replicating thousands of experiments, can be performed efficiently.

1.3.3 Finite element method

One of the most widely used computational methods at the meso- and macro-scale is the finite element method (FEM). The finite element formulation of the problem results in a system of algebraic equations, yielding approximate solutions at a finite number of points over the continuum domain. To solve the problem, it subdivides a large problem into smaller sub-domains that are called finite elements. The simple equations that model these finite elements are then assembled into a larger system of equations that models the entire problem. FEM uses variational methods from the calculus of variations to approximate a solution by minimizing an associated error function. Avoiding to describe in detail the theory behind the formulation of basic and advanced non-linear finite element which is beyond the scope of this thesis and that can be found in several fundamental books [61, 62] we here address some common issues in the modelling of high-velocity impact and large deformation problems.

Nowadays, commercial software offers robust non-linear FEM tools for the analysis of these types of large-scale problems at an acceptable computational cost, implementing advanced and highly-optimized contact algorithms capable of simulating high-energy impact conditions [63]. To solve time dependent ordinary and partial differential equations with finite element analysis, either an explicit or an implicit solution schemes can be used. The first usually represent an advantage in high-velocity impact simulations, and actually is the one used, since the equation of motion is solved step by step by computing nodal accelerations rather than displacement, thus saving computational time and memory for the determination and allocation of the stiffness matrix. The advantage is more important as the number of degrees of freedom of the model increases. Moreover, this method is much more stable under severe materials (soft media) and geometrical non-linearities

(such as the ones deriving from contacts). However, this scheme has its counteracting disadvantage: the solving technique is only conditionally stable, which means that a minimum time step must be guaranteed. If the solution becomes unstable the error will rapidly increase with every time step and the solution will become invalid. An explicit method usually needs to have 100 to 10000 times smaller time steps than an implicit technique, that is unconditionally stable, to avoid this kind of errors. The time step Δt for this method is limited by the time that the elastic shock wave, that arises from the loading, takes to transmit through the smallest element in the mesh of the model:

$$\Delta t = \frac{l_c}{c} \tag{1.1}$$

where l_c is the smallest distance between any two nodes in the model and $c = \sqrt{\frac{E}{\rho(1-\nu^2)}}$ is the sound speed in a bidimensional material, here assumed for sake of simplicity linear, elastic and isotropic (thus defined by the elastic modulus E and the Poisson's ratio ν). This distance generally corresponds to the edge with minimum length in solid element and thin shell element, to the thickness in thick-shell element formulation, and to the length of a monodimensional beam element. As consequence, finer discretizations result in increased computational time both due to the higher degrees of freedom to be computed and to the higher number of iterations, which are inversely proportional to the timestep Δt. As consequence, it is very difficult to couple disparate scale levels in the same simulation since the element size and the time step will be governed by the lowest dimensional scale. From Equation (1.1) it emerges that $\Delta t \sim (E/\rho)^{-1/2}$, thus bulk materials coupling extreme high modulus and low density may represent an issue in terms of computational cost. On the other hand, materials with high specific modulus are the ideal candidates for impact protection since the energy dissipation capability of a material under ballistic impact can be assessed by the magnitude of the Cuniff's parameter $U = \frac{\sigma\varepsilon}{2\rho}\sqrt{\frac{E}{\rho}}$ [64, 65], which basically is the product of the material toughness times the wave speed in the considered medium. Common timesteps for impact simulations on systems at the centimeter scales are of the order of 10^{-8}s which represents a limit for the last time of the physical phenomenon to be modelled. However, this problem is partially mitigated due to the fact that the maximum characteristic time of an high-velocity impact event, is of the order of few milliseconds. When dealing with low velocity impacts, a common practice, is to fictitiously increase the mass of the system (procedure generally known as "mass scaling") in order to maximize the minimum timestep required for stability. However this practice must be properly evaluated and only exploited when the kinetic energy of the system is sufficiently low to be considered negligible in the specific problem, such as in quasi-static simulations.

Given the fine discretization that may be required in order to accurately simulate impact phenomena, usually under integrated elements are preferred over fully integrated formulations to reduce the computational cost of the model and compensate the previous issues. For the function to be integrated to find the solution of the finite element problem,

a number of points are calculated, known as Gaussian coordinates, whose position within the element is optimized for the highest grade of precision of the quadrature rule used to approximate the integrals. For each of these points, the function is multiplied by an optimised weight function. Then these are added together to calculate the integral. Reduced integration uses a lesser number of Gaussian coordinates when solving the integral. Clearly, the more Gaussian co-ordinates for each element, the more accurate the answer will be, but this has to be weighed up against the cost of computation time. For example, the stiffness matrix has to be calculated in just one integration point of the element in case of "one-quadrature rule" rather than the four of a 2x2 Gauss integration. The use of fewer integration points should produce a less stiff element. This sometimes is beneficial since it counteracts the overestimated stiffness of some elements, derived from their formulation, and in some particularly non-linear problems such as plasticity, creep or incompressible materials the slight loss of accuracy is counteracted by the improvement in approximation to real experimental behaviour.

Sometimes the reduction of of the stiffness matrix leads into its singularity generating the so called *hourglass* modes of deformation, also known as "sporious" or "zero-energy" modes. These deformation modes are associated with null energy and can easily propagate through the mesh, producing meaningless results. It typically manifests as a patchwork of zig-zag or hourglass like element shapes (hence the name), where individual elements are severely deformed, while the overall mesh section can be nearly undeformed. It is quite common to experience severe hourglassing that may be visually apparent without magnification of the displacements. Generally this kind of modes are mostly prone to be generated by concentrated loads or contact pressures. Hourglass can be faced in several methods: by inserting an artificial stiffness to the hourglass deformation modes (the default way utilised in static/quasi-static problems), by inserting an artificial viscosity (preferred for dynamic and high-velocity impact problems), by using fully integrated elements (but more expensive and less robust) and by refining the mesh (computationally expensive). Sometimes proper boundary conditions can avoid the formation of these modes due to displacements compatibility conditions. The basic hourglass control methodologies have been pioneered by Belytschko and co-workers [66]. The employment of the first two solutions, which have a negligible additional computational cost, require a careful check in order to verify that the fictitious forces introduced to contain spurious mode of deformation are associated to a contained work that could drag physical energy from the system. For this, according to a widely acknowledged "rule of thumb", the hourglass energy must be lower than 10% (but the lower is better) of the strain energy to consider the simulation accurate. This condition must hold both for the whole model and for each of his sub-parts defined by different structural elements, material model or kind of element.

Some of the remaining issues of grid-based methods in modelling impact and large deformations problems are related to dealing with material separation (fragmentation) and capturing inhomogeneities in the deformation, leading to fracture and material failure.

One possible solution to treat fracture are erosion algorithms: in these approaches the elements of the model are deleted from the simulation when the material reaches the imposed failure condition in a prescribed number of integration points. The energies of the deleted elements are properly stored and accounted in the energy balance, but these portions of material are not able to interact any more with the rest of the medium. Stress concentration arise around the created discontinuities and fractures can then nucleate and propagate as subsequence of element deletions. It is clear how the propagation pattern of fracture is highly dependent to the size and geometry of the mesh. While this approach can be acceptable in impact simulations of ductile materials, leading to satisfying results for sufficiently fine meshes, it represents an intrinsic big limit when dealing with of brittle materials or in those model whose scope is to characterize the fracture properties (e.g., toughness) by subjecting the specimen to tension, without imposing a-priori a defect in the structure. To a certain extent, these problems are addressed by meshfree (or meshless) methods reviewed next.

1.3.4 Meshless methods and peridynamics implementation

Mesh-free methods are numerical techniques in which there is no fixed connectivity between the discretization nodes, and they are advantageous when simulating impact failure, penetration, and fragmentation. The level of non locality of interaction is defined by the "horizon" radius δ which defined the nodes within the generated spatial sphere to be assigned as neighbour of the reference node. Mesh-free methods can be developed for continuum (solids and fluids) or for particle-based (granular materials) formulations.

A new non local method for modelling continuous media, the so-called peridynamics, has been proposed [67] specifically for modelling multiple interacting fracture in the dynamic regime. Unlike the partial differential equation of the standard theory, the integral equation of peridynamics are applicable even when cracks and other singularities appear in the deformation field. Thus, continuous and discontinuous media can be modelled with a single set of equations allowing the spontaneous formation and propagation of discontinuities. Peridynamics naturally leads into a meshless framework which is well suitable for the simulation of high energy impacts involving penetration and fragmentation [68]. This has already been implemented in the acknowledged molecular dynamics code LAMMPS (Large Atomistic Massive Molecular Package Software) [69] giving it computational mechanics capability enabling simulations at mesoscopic or even macroscopic length and time scales [70]. Peridynamics especially suits for the modelling of elastic-brittle materials, however successful simulations have already been perform also on viscoelastic materials, thin membranes, and rods [71]. Since the theory is relatively recent its effective application to a wide class of bio-materials (e.g., hyperelastic-like or experiencing large deformation) has yet to be performed and both the theoretical and the numerical framework have been treated in a limited number of works. However the literature in the field is in constant and high-rate update. Recently, the successful coupling

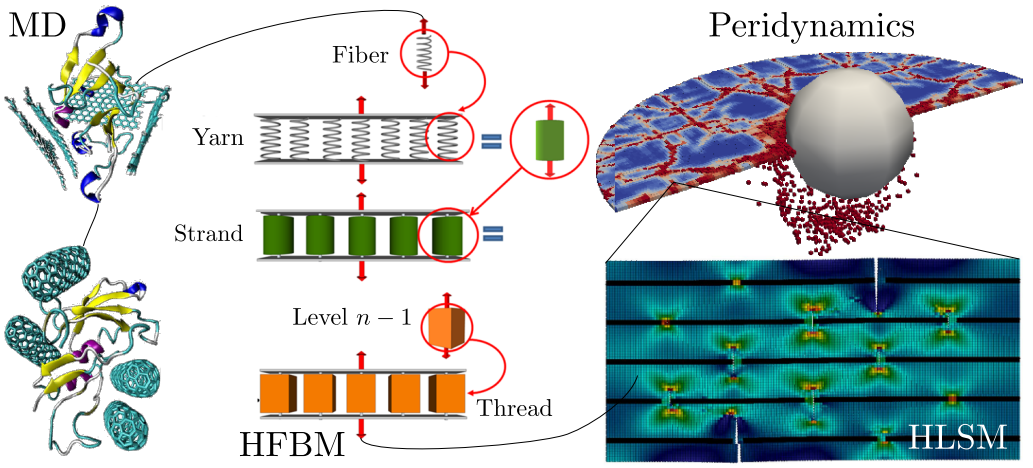

Figure 1.4: Schematical representation showing the merging of different computational methods at different scale levels for the characterization of biological and bio-inspired hierarchical materials for impact simulations. Each method is used to derive the mechanical properties to be used as input in the upper hierarchical level (MD and HLSM images adapted from refs. [6–8] with permission).

with a finite element scheme has been obtained also for impact applications [72], showing the concrete possibility of a real multiscale approach from atomistic to continuum in treating such phenomena.

Chapter 2

Impact mechanics of multilayer composite armours

An analytical and a finite element method (FEM) models were developed to study the impact properties of multilayer composite armours subjected the ballistic impact of projectiles with arbitrary angle of incidence, shape, size, and frictional characteristics. The proposed equations adapt and extend acknowledged impact models based on the conservation of energy to multilayer targets. The effect of thickness compaction during the production process is also included in the model. It emerges that an increase of the curing pressure can enhance the impact strength. This improvement in impact performance can be quantitatively predicted with good approximation according to the Linear Elastic Fracture Mechanics. Dynamic FEM simulations were used to complementary analyse failure modes and damage within the impacted target. Both approaches were validated by extensive ballistic tests on composite targets and used to investigate the role of the layer stacking arrangement. Vemar Helmets S.r.l. (Grosseto, Italy), in the person of the CEO Nicola Simoni and of the project responsible Roberto Vannucci, is gratefully acknowledged for having shared data and photographic documentation of the experimental ballistic tests.

2.1 Introduction

Armours used for personal protection are generally manufactured with fibre-matrix composites due to their lightness and good ballistic properties, namely the capability to absorb the kinetik energy of an impacting projectile. These multilayer structures are generally formed by assembling layers of unidirectional (UD) or woven fabrics made of high performance fibres embedded in a thermosetting resin, which confers the desired shape to the object [15]. The high-strength fibres used in making fabrics include aramid materials (Kevlar®, Twaron®, Technora®), high-performance polyethilene (Spectra®,

Dyneema®), and more recently polybenzoxaloze (Zylon®). These fibres are characterized by an high tensile modulus over density ratio (E/ρ), failure strength σ and strain to failure ε, that make them ideal for impact applications. Indeed, according to the dimensional analysis carried by Cuniff [64, 65] the limiting penetration velocity of an homogeneous elastic barrier scales as $U^{1/3}$ where $U = \frac{\sigma\varepsilon}{2\rho}\sqrt{\frac{E}{\rho}}$ is basically the product of the material specific toughness times speed of the elastic waves in the considered medium. In case of need of protection against high velocity and penetrating projectiles (e.g., armour piercing projectiles) a hard face ceramic layer can be introduced in order to damage and shatter the fragment [73], while the dissipation of the residual kinetic energy is demanded to the backing multilayer composite package [21, 22]. This solution can be considered, in a certain sense, bio-inspired since it can be found in many examples of natural dermal armours previously cited [27, 36, 74] composed by an external hard mineral layer and a fibrous and multilayer collagen substrate. Other critical issues are the multi-hit capability and close-shot spacing [21].

Performing empirical tests has been for a long time the most straightforward method to achieve a specific task of performance, but it is generally costly, time-consuming and often not sufficient for obtaining a significant and systematic amount of data for optimization. Numerical simulations are relatively cost and time effective, but require a relatively high computing power and resources depending on the level of detail, and may present some intrinsic limits especially when dealing with problems involving complex dynamic fracture. Analytical methods become convenient as an important alternative if closed-form mathematical equations can be set up to describe the dominant physical and phenomena that occur during the impact event, so long as the assumptions inherent in the model are applicable. Several studies about the analytical modelling of ballistic impact of multiple layered fabric panels [31, 75–81] are available in literature. General continuum mechanics principles, such as Newton's second law of motion, are commonly adopted in the analyses.

It is well known that while fibre properties are important, the structural assembly plays a key role in determining the ballistic performance of multilayer armours. For example the orientation and the geometry of the yarns can significantly change the constitutive response of the ply. The importance of compaction in the curing process for the final quality of composite laminates is widely acknowledged in the industry sector. An interesting and comprehensive work can be found in [82]: there the role of the textile orientation, of the component geometry and of their interaction on the resin flow in the mould, and then on the final quality of the component, is experimentally studied. However, the a self-consistent theory for explaining the role curing procedure for composites on impact performances has, to best of the author's knowledge, still to be reported and included in related models.

The aim of the work was to study the role of the structural assembly on the protection capability of multilayer armours and on its scaling for different configurations. We focused

on the role of layers stacking sequence with the effect of different through-thickness strength distributions and on the effect of thickness compaction during the production processes. Analytical and numerical results are validated by extensive experimental data of several impact scenarios, such as heterogeneous targets and oblique collision.

2.2 The analytical impact model

2.2.1 Base model

The proposed model is valid for axisymmetric and rigid short-rod projectiles colliding hybrid multilayer targets at the high-velocity regime ($\approx 300-3000\,\mathrm{m/s}$ [30]). The variables considered in the penetration model are:

- the geometry of the target, namely the number and thickness of layers;
- material properties of the target;
- projectile geometry, mass, velocity and angle of incidence;
- frictional characteristics between the projectile and the target

The dissipations by mean of heat energy, delamination, and mechanical waves generated in the ballistic penetration are neglected in this model. In particular, energy dissipation by mean of heat generation due to material internal friction and friction between the projectile and the target is not considered in the model, being acknowledged that this form of dissipation can be neglected for the projectile velocity regimes and for thin targets [16-20], as the ones investigated in this study. Assuming the conservation of linear momentum according to Newton's second law of motion, the reduction of the instantaneous velocity v of a projectile impacting on a bulk target can be estimated if the net resisting force F applied on the projectile of mass m is known:

$$m\frac{\mathrm{d}v}{\mathrm{d}t} = mv\frac{\mathrm{d}v}{\mathrm{d}h} = -F, \tag{2.1}$$

where h is the instantaneous depth of penetration of the projectile in the target. This differential equation has to be integrated assuming an expression of F. Considering the dissipation of the projectile kinetic energy in a volume of target material defined by the impactor projected radius radius R, F can be assumed as a first approximation to be constant and equal to $\eta\sigma\pi R^2$, where σ is the material ultimate compressive strength and $\eta \geq 1$ is a corrective factor which has the physical meaning of ratio between the actual damaged area and the projected area. This means that the relation between the the residual projectile kinetic energy (K_{res}) and its initial impact value (K_0) is linear, with unitary slope and intercept Ft. In the reality, this slope is generally lower than the unity due to

additional dissipations, such as delamination, mechanical waves and the formation of ejecta. Moreover, assuming a constant expression for F, the material strain rate-effect are not taken into account and then the material strength is assumed to be equal to its nominal static value. To include rate dependence, the armour material strength can be rewritten as a quadratic form of the impact velocity V [83]:

$$\sigma = \sigma_0 \left[a_0 + a_1 \left(\frac{v}{V^*} \right) + a_2 \left(\frac{v}{V^*} \right)^2 \right], \tag{2.2}$$

where $V^* = \sqrt{\sigma_0/\rho}$ [84], is a characteristic velocity function of the the static monoaxial compression strength of the material σ_0 and of its density ρ in the undeformed state; a_0, a_1 and a_2 are dimensionless coefficient that modify the plate strength taking into account the projectile shape effect [85]:

$$a_0 = A_0 \left(1 + \frac{2}{R^2} J_0 \right), \tag{2.3a}$$

$$a_1 = A_1 \left(1 - \frac{2}{R^2} J_1 \right), \tag{2.3b}$$

$$a_2 = A_2 \left(1 - \frac{2}{R^2} J_2 \right), \tag{2.3c}$$

where A_0, A_1 and A_2 are experimentally determined coefficient for different constitutive models [84, 86]. If unknown, they could be obtained by the best fitting of experimental ballistic curves in the penetration regime (i.e, projectile residual velocity vs. its initial impact value, $V_{\text{res}} - V_0$) with the analytical model developed here. J_0, J_1 and J_2 are shape function of the impactor profile and defined as follows [85], according to the scheme of Figure 2.1:

$$J_0 = \mu \int_0^L y \, \mathrm{d}x, , \tag{2.4a}$$

$$J_1 = \mu \int_0^L y y_{\mathrm{x}} \left[1 - \frac{y_{\mathrm{x}} + \mu}{\sqrt{1 + {y_{\mathrm{x}}}^2}} \right] \mathrm{d}x, , \tag{2.4b}$$

$$J_2 = \mu \int_0^L y y_{\mathrm{x}} \left[1 - \frac{y_{\mathrm{x}} \left(y_{\mathrm{x}} + \mu \right)}{1 + {y_{\mathrm{x}}}^2} \right] \mathrm{d}x, , \tag{2.4c}$$

where y_{x} is the derivative of the profile function along the axial direction of the projectile and μ is the dynamic friction coefficient between the impactor and the target. Thus, with Equations (2.24) it is possible to take into account the role of projectile size, shape and friction on its penetrability with equal initial kinetic energy. Note that for $R \to \infty$ the shape effect given by Equations (2.3) vanishes and that when $a_1 = a_2 = 0$ (no strain-rate effect

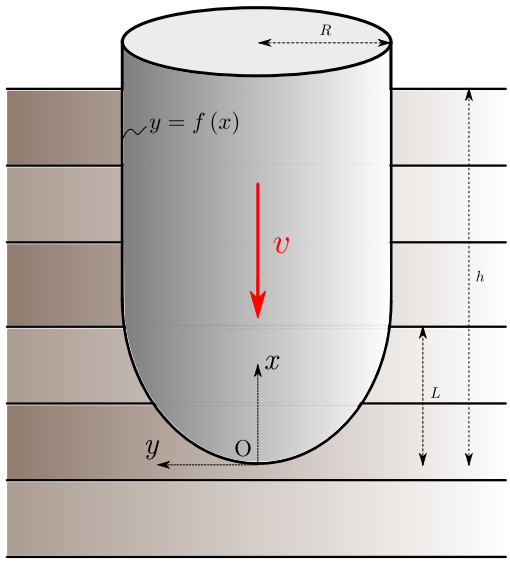

Figure 2.1: Notation for the analytical model. y is the function describing the projectile shape, L is the coordinate at which $y \equiv R$, ind h the current depth of penetration reached by the projectile.

considered) is $\sigma = \sigma_0 a_0$ is the static compression strength corrected only by the projectile shape factor.

Let now consider a multilayer target, subjected to normal impact, made of a sequence of N layers of different incompressible elastic-perfectly plastic, homogeneous and isotropic materials. Let call with V_i the exiting velocity after the passage of projectile through the i-th layer. The compressive failure strength of the materials is $\sigma_i(V_i)$, depending on the instantaneous impact velocity according to Equation (2.2). The thickness t_i can also be different for each layer. Equation (2.1) yields to:

$$\int_{V_{i-1}}^{V_i} mv\,\mathrm{d}v = \int_0^{t_i} F_i\,\mathrm{d}h, \tag{2.5}$$

and introducing the strain-rate dependence formulation for the plate strength σ according to Equation (2.2) ($\eta = 1$):

$$\int_{V_{i-1}}^{V_i} mv\,\mathrm{d}v = -\int_0^{t_i} \sigma_{0,i}\pi R^2 \left[a_0 + a_1\left(\frac{v}{V_i^*}\right) + a_2\left(\frac{v}{V_i^*}\right)^2\right]\mathrm{d}h, \tag{2.6}$$

and then

$$\frac{m}{\sigma_{0,i}\pi R^2}\int_{V_{i-1}}^{V_i} \frac{v}{\left[a_0 + a_1\left(v/V_i^*\right) + a_2\left(v/V_i^*\right)^2\right]}\,\mathrm{d}v = -\int_0^{t_i}\mathrm{d}h. \tag{2.7}$$

Solving the integral of Equation (2.7) it is possible to find the velocity V_i after the passage of the impactor through the i-th layer; at $V_i = 0$ it is possible to determine the final depth of penetration H, by summation, as:

$$H = \frac{m}{\sigma_{0,i}\pi R^2}\int_0^{V_{i-1}} \frac{v}{\left[a_0 + a_1\left(v/V_i^*\right) + a_2\left(v/V_i^*\right)^2\right]}\,\mathrm{d}v + \sum_{n=1}^{i-1} t_i. \tag{2.8}$$

The integrals in the Equations (2.7) and (2.8) are not of easy solution. In order to obtain a closed-form solution we assume that $a_{1,i} = 0$ coherently with experimental results presented in the literature [16, 85, 86]. Thus, is $\sigma_i = \sigma_{0,i}\left[a_{0,i} + a_{2,i}\left(v/V_i^*\right)^2\right]$ and Equation (2.7) can then be rewritten, multiplying and dividing by the constant factor $2a_{2,i}/(V_i^*)^2$, as:

$$\frac{m(V_i^*)^2}{2a_{2,i}\sigma_{0,i}\pi R^2}\int_{V_{i-1}}^{V_i} \frac{2a_{2,i}\left(v/(V_i^*)^2\right)}{\left[a_{0,i} + a_{2,i}\left(v/V_i^*\right)^2\right]}\,\mathrm{d}v = -\int_0^{t_i}\mathrm{d}h. \tag{2.9}$$

By recognising in the integral at the left-hand side the derivative of al logarithmic function, the velocity V_i of the projectile after the passage of the i-th layer can be determined as a function of the exiting velocity of the precedent layer V_{i-1}:

$$V_i = \sqrt{\frac{(V_i^*)^2}{a_{2,i}}\left\{exp\left[-2a_{2,i}\frac{\sigma_{0,i}\pi R^2 t_i}{m(V_i^*)^2}\right]\left[a_{0,i} + a_{2,i}\left(\frac{V_{i-1}}{V^*}\right)^2\right] - a_{0,i}\right\}}, \tag{2.10}$$

which is valid until the expression under the square root is positive or equal to zero. If the previous condition is not satisfied, it means that the projectile has been stopped by the i-th layer and the corresponding final depth of penetration H can be calculated as follows, accordingly to Equation (2.8):

$$H = \frac{m(V_i^*)^2}{2a_{2,i}\sigma_{0,i}\pi r^2}\ln\left[1 + \frac{a_{2,i}}{a_{0,i}}\left(\frac{V_{i-1}}{V^*}\right)^2\right] + \sum_{n=1}^{i-1} t_n. \tag{2.11}$$

Consistently, the higher impactor mass m or velocity V_0 result in higher perforation depth H, while higher target strength σ and impactor imprint radius R to lower depth of penetration.

Considering the more general case of oblique impact with angle of incidence θ, and yaw angle (angle between the striker axis and the velocity vector) assumed to be zero, the rear of the impact front nearly becomes of elliptical shape $\pi c_i d_i$ with mayor and minor semi-axes given respectively by [19]:

$$\begin{cases} c_i = R\sec\beta + \sum_{j=1}^{i-1} t_j \tan\theta \\ d_i = R + \sum_{j=1}^{i-1} t_j \tan\theta \end{cases} \tag{2.12}$$

where θ is the angle of the cone of diffusion of damage through the thickness, which is $\approx 45^\circ$ for composite materials [19], c_i is the semi-axis in the plane of striker impact motion and d_i the minor one along its orthogonal direction. Thus, the resisting force for the i-th layer becomes $F_i = \sigma\pi c_i d_i$ and, posing $R_i = \sqrt{c_i d_i}$ in the Equation (2.6) and following, a further generalization of the model for non normal impact is obtained. Thus, by increasing the projected volume, in the oblique impact configuration the capacity of the projectile to perforate the target expected to reduce with increasing impact incidence θ.

2.2.2 Effect of thickness compaction

Apart from the strain-rate effects, the ratios σ/ρ and E/ρ, respectively the specific material strength and stiffness, can be considered as material constants, independently from the thickness reduction. Let consider the compaction during the production process that occurs in the cleavage and curing of woven textile-epoxy composites. Assuming a compressible material, the lateral confinement implies $\rho \propto t^{-1}$ and, consequently, the characteristic strength σ_0 of the material scales in the same way, namely $\sigma_0 \propto t^{-1}$. However, in this way, we neglect the defects, always present, within the material. The well-known energetic approach proposed by Griffith [87] for the problem of a tensioned plate of unitary thickness with a crack of length $2a$ yields to the Linear Elastic Fracture Mechanics (LEFM) relation of dependence between the characteristic specific material strength and the half-length of the crack:

$$\frac{\sigma_{0,\mathrm{C}}}{\rho} = \sqrt{\frac{EG_{\mathrm{C}}}{\rho^2\pi a}}, \tag{2.13}$$

where G_{C} is the material fracture energy, that is the energy required for the propagation of a crack of unitary surface and $K_{\mathrm{C}} = \sqrt{EG_{\mathrm{C}}}$ is the material fracture toughness. The characteristic crack length is proportional to the minimum dimension of the body, that is the upper limit of the defect dimension: in our specific case this limit is coincident with the layer thickness t. Recalling that $\rho \propto t^{-1}$, Equation (2.13) yields to the following scaling law for the material strength due to compaction effects:

$$\sigma_{0,\mathrm{C}} \propto t^{-\frac{3}{2}}, \tag{2.14}$$

that clearly shows the beneficial effect of compaction on the material strength, and thus on the armour toughness. As a result of this, we have introduced the scaling law of Equation (2.14) in the model by mean of a compaction rate κ: this coefficient is defined as the ratio between the layer thickness after compaction and the nominal thickness of the non-compacted material, thus $0 < \kappa < 1$. The nominal value of σ_0 is scaled according to the level of compaction as follows:

$$\sigma_{0,\mathrm{C}} = \sigma_0 \kappa^{-\frac{3}{2}}, \tag{2.15}$$

where $\sigma_{0,C}$ identifies the compaction dependent material strength. The coefficient κ could be correlated to some characteristic parameters of the production process, for example to the magnitude of pressure and temperature.

On the other hand, in the case of composites we have to consider the formation of microcracks due to excessive compaction, especially if the pressing occurs after the partial or complete setting of the epoxy resin. This yields to a progressive and distributed damage and then to a decrease of the Young's modulus of the matrix phase and of the overall composite as well. This behaviour suggests to push the machine pressure, when possible, to values near to the matrix compressive strength limit $\sigma_{0,m}$, that is approximately $80 \div 120$ MPa for an epoxy resin [88], before material degradation. According to the authors knowledge, the actual values of pressure currently used in cleavage ($\approx 150 \div 200$ bar, $15 \div 20$ MPa) are very far from this limit and the use of higher pressures should be actually investigated in this direction.

Under a different approach, as demonstrated in a previous work [89], fracture dissipates energy in a fractal domain whose dimension is intermediate between an euclidean surface (D=2) and a volume (D=3):

$$K_{\text{abs}} = e^{(D)} (\lambda A t)^{D/3}, \tag{2.16}$$

where D is the fractal exponent ($2 \leq D \leq 3$), $e^{(D)}$ is the dissipated energy per fractal unit volume, and λ is the ratio between the actual damaged volume and the overall impacted volume ($At = \pi R^2 t$, in case of axisymmetric projectile). Assuming $e^{(D)}/\rho$ as a material constant, it follows:

$$\left[\frac{\zeta m V_0^2 \rho / e^{(D)}}{2\rho} \right]^{3/D} = \lambda A t, \tag{2.17}$$

where ζ is the percentage of energy dissipated by mechanical waves outside the impact zone. Defining $M = \rho A t$ as the penetrated material mass, it is possible to determine the critical areal density needed to stop the projectile as a function of the material density:

$$\frac{M}{A}\Big|_{\text{crit}} = \rho t\Big|_{\text{crit}} = \left[\frac{\zeta m v^2 \rho / e^{(D)}}{2\rho} \right]^{3/D} \frac{\rho}{\lambda A} \propto \rho^{1-3/D}. \tag{2.18}$$

Since $1 - 3/D \leq 0$, it is again demonstrated beneficial role of thickness compaction. Note that $D = 3$ ($e^{(D=3)} \approx \sigma_C$) corresponds to the classical absence of scaling $\sigma/\rho \propto t^0$ =const., the LEFM scaling $\sigma/\rho \propto t^{-1/2}$ corresponds to $D = 2$ ($e^{(D=2)} \approx G_C$), while $D = 2.5$ ($e^{(D=2.5)} \approx K_C$) is an intermediate situation.

2.3 Finite element model

Each of the targets is modelled as circular plate with a radius of 60 mm. Indeed, due to high localization, a radius greater than 6 times the radius R of the impactor is acknowledged to

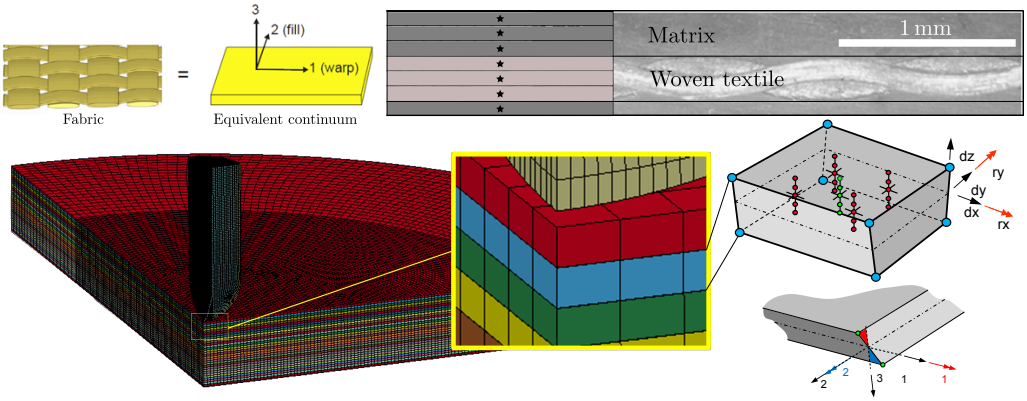

Figure 2.2: Schematic representation of the modelling of the composite part of the analysed armour. The real woven fabric immersed in the thermoset resin is modelled as a continuum equivalent medium. The two phases of the composite, fibres and matrix, are considered in the model ply introducing to each through-thickness integration different material models or properties according to the volume fraction of each phase. As consequence of the production techniques the ply can approximated as formed by an inner core with the properties of the woven and the outer part filled by the matrix, as confirmed by the SEM photograph.

be sufficient to avoid edge effect on the results. Where allowed by the particular symmetry conditions, just a quarter or half of the plate were simulated.

For modelling the composite backing thick-shell elements were used (Figure 2.2). This kind of elements are more suitable with respect to solids to capture the bending of thin medium with a limited number of through thickness element and can be used in those situation where the aspect ratio of the element does not allow the use of classical thin shell element formulations [61]. Being also the thickness a geometrical quantity, unlike in the classical thin shell formulations, another advantage is the computation of deformation in the out of-plane dimension, making this element formulation particularly suitable for treating the high compressive contact stresses generated by transverse impact. In the layered variant of the thick shell formulation it is possible to assign an arbitrary number of integration point in the element thickness and attribute to each of them a different constitutive law (woven textile or matrix) according to the volumetric fraction of the textile (Figure 2.2).

The time-step Δt used in for integration of the solution is selected on the basis of the mesh size for allowing the wave propagation through the medium. Being c the propagation velocity of the elastic wave in a 3D linear elastic isotropic and homogeneous material

given by:

$$v_c = \sqrt{\frac{E(1-\nu)}{\rho(1+\nu)(1-\nu)}}, \tag{2.19}$$

and the minimum time-step is computed as:

$$\Delta t = \frac{l_c}{c}, \tag{2.20}$$

where c is the minimum characteristic edge size among all elements of the model. For the thick shell elements used in our simulations is $l_c = V/A_c$, where V is the volume of the of the critical element in the mesh which minimizes Δt and A_c the larger face area of the same element. Being the shorter edge usually the thickness of the thick shell, l_c generally corresponds to the element height itself. To be precautionary -on a time-step basis- the wave speed velocity was computed for all simulations on the stiffer phase of the composite, that is the fibre fraction, maximizing c and thus minimizing Δt. Although the so determined Δt (Equation (2.20)) is sufficient to ensure convergence and stability of the solution, it was multiplied by a factor of 0.9. The initial time-step is automatically adjusted during the simulations by taking into account the deformation of the elements, which may reduce the current l_c with respect to the initial value of the undeformed state. The convergence test for the model of plate 8 (see Table 2.2 in the Appendix II) with respect to the mesh size is shown in Figure 2.3 as a characteristic example, demonstrating the convergence for the used characteristic mesh size of 0.1 mm.

The mesh size was also selected to allow the correct propagation of elastic and shock waves through the medium, so that their wavelength $\lambda = c/f$ is larger than the mesh size (characteristic frequency is $f = 10^5$ Hz [19]). In our case this results in λ = 0.8-1.2 mm, depending on the elastic properties of each material, and thus this value represents an upper bound for the allowed mesh size. Moreover, the 2x2 Gauss scheme adopted in the plane further reduces the nodal wavelength by a factor ≈1/3, and for a mesh size of 0.1 mm it results that the nodal wavelength is 0.26-0.4 λ. In this sense, the convergence shown in Figure 2.3 for a mesh size of 0.1 mm -showing no significant difference with a mesh size of 0.05 mm (nodal wavelength ≈1/6 of the elastic wavelength)- confirms the validity of our approach. Through the element thickness a total of 10 integration points are used, thus the out of plane mesh size is even more precautionary.

For modelling both the fibre and the matrix fraction of the textile an orthotropic material model was used. It allows to set the behaviour in tension, compression and shear along to the two orthogonal in plane directions and the out-of plane one. The model implements a linear-elastic branch followed by a nonlinear post peak softening behaviour: the residual strength in compression, tension and shear can be defined as a fraction of the maximum material peak stress allowing for post-peak dissipation capability. The equations which define the failure criteria used for the model are presented in detail in the paper by Matzenmiller and co-workers [90]. The material properties of the fibre and

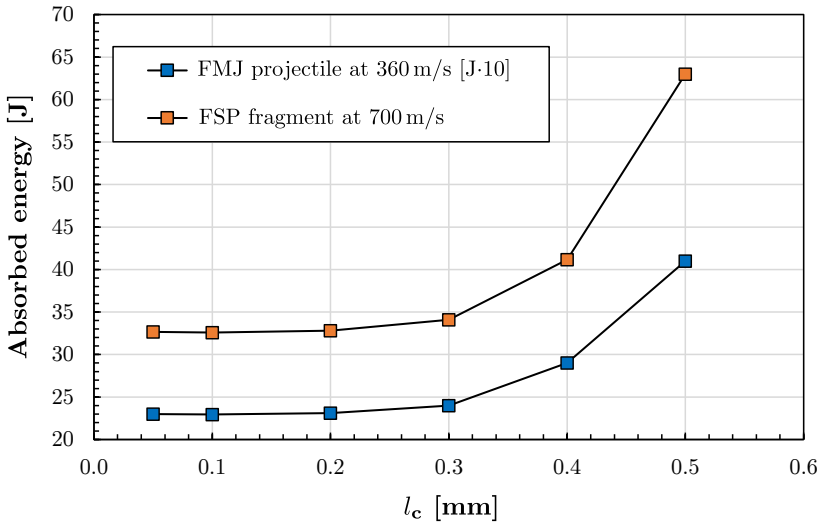

Figure 2.3: Convergence of the absorbed energy by the target as a function of the thick shell element in-plane edge size executed for 1 layer of material of plate 8 (see Table2.2 in the Appendix II). Below the impact area the thick shell elements have aspect ratio 1:1 with $l_c = 0.1$ mm.

the matrix were obtained from the technical sheets of the producers (see Table 2.2 in the Appendix II for textile products specification).

The adhesive contact interactions between the different plies are implemented with a so called *tiebreak* contact. Considering a couple of adjacent nodes belonging to two subsequent layers, these are initially bonded together and the contact interface can sustain tractions. A stress-based constitutive law is implemented to define the constitutive behaviour of the interface. The adhesive interface fails when it is satisfied the following condition:

$$\left(\frac{s_\perp}{\sigma_\perp}\right)^2 + \left(\frac{s_\parallel}{\sigma_\parallel}\right)^2 \geq 1, \tag{2.21}$$

where $s_\perp$ and $s_\parallel$ are the current normal and tangential stress between two welded interface nodes, while $\sigma_\perp$ and $\sigma_\parallel$ are their corresponding limit values, which may be different, defining an elliptic domain. To fully define the constitutive behaviour of the interface it is also necessary to set a critical separation δ_0 for the two opening modes of the interface, after which the force can decrease until a failure nodal separation δ_f accounting for progressive damage (Figure 2.2) or suddenly drop to zero ($\delta_f = \delta_0$). Note that the Equation (2.21) is analogous to a cohesive zone model where stresses are placed by the current and critical fracture energies G. Here the stress based solution is used due to the fact that in the dynamic regime is not easy to experimentally measure the critical

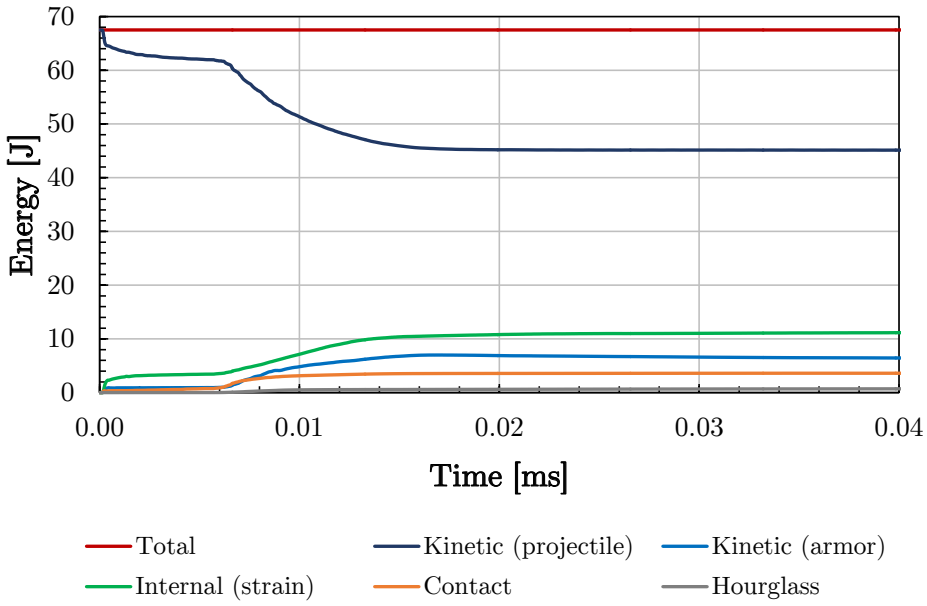

Figure 2.4: Evolution of system energies over time in impact simulation.

fracture energies and thus perform a calibration of the FEM model, also due to the lack of standardized methods. Once the nodes separate the contact locally switches to a penalty algorithm and the layers can mutually interact with friction. The kinetic law used in the contact model to compute the current friction coefficient as a function of the static and dynamic values, μ_0 and μ_∞ respectively, assumes the following typical velocity-weakening expression:

$$\mu = \mu_0 + (\mu_0 - \mu_\infty) e^{-v/v_{\text{crit}}}, \tag{2.22}$$

and is a function of the relative velocity v of the sliding nodes and the same friction law applies for the contact between the projectile and the parts of the target.

From simulations it is possible to extract several quantities ranging form kinetic and strain energy of the various part of the model (projectile and layers), to the stress and strain state within the impacted target, and the energy dissipated by frictional contact and delamination. Figure 2.4 shows a typical energy balance output of an impact simulation showing the various contribution which causes the loss of projectile kinetic energy.

2.4 Results

2.4.1 Models validation

In order to validate the developed analytical and finite element models a series of 43 plates composed of different laminates made of traditional (carbon, Kevlar®, and glass) and innovative (Twaron®, Innegra®, Dyneema®) fabrics were tested under ballistic experiments with the Remington 9 mm Parabellum projectile [10] and the FSP fragment 0.22 in [9]. Results are also compared with a reference steel spherical projectile of radius 5 mm and mass 4.1 g. The analytical model has been implemented in a code which allows to calculate in an automated way the velocity profile of the impacting projectile through the target, the corresponding depth of penetration, and the expected critical target thickness in order to stop the projectile of given shape and kinetic energy. The geometrical characteristics of the tested projectiles and the corresponding shape functions according to Equations (2.24) are reported in the Appendix I of this Chapter. Table 2.2 in the Appendix II reports the geometrical characteristics of each target with the corresponding constituent materials according to the producers identification, the weight of resin and textile from which is possible to determine the fibre volume fraction, and the parameters characterizing the curing and cleavage process, that is the temperature, the forming pressure and the duration of the process. The thermosetting resin, wherever used, is the same for all plates and is a Bakelite® EPR L 1000 with density 1135 $\mathrm{kg/m^3}$ and tensile strength of 72.3 MPa.

The analytical predictions on the role of compaction provided by Equation (2.18) are depicted in Figure 2.5 which shows the variation of the normalized critical target mass $M/A\big|_{\mathrm{crit}}$ -namely the critical target areal density- as a function of the compaction ratio κ. In the same figure the result of the analytical model incorporating LEFM for the three characteristic projectile analysed are reported. A beneficial effect of compaction in increasing energy absorption capability, thus reducing the critical target areal density, clearly emerges. The beneficial effect of compaction is predicted to affect mostly the protection against the Remington 9 mm, which shows the higher increase in energy absorption due to thickness reduction among the three considered impactors. The fragment still confirms to a be a critical issue for the protective capability of the targets, being the less sensitive to target compaction. Considering the absorption capability per unit thickness, for example we predict that a compaction of 20% ($\kappa = 0.8$) would correspond to an increase of 11.8 % of the armour critical energy, namely of the minimum impact energy to perforate the target, with $D = 2.0$, +4.5 % for $D = 2.5$, while the classical theory $D = 3$ cannot predict any increase in the absorption capability at different size scale. The obtained results for the three tested projectiles provide an intermediate situation between $D = 2.0$ and $D = 2.5$ (Figure 2.5).

Regarding the experimental ballistic tests each plate was leant against a block of soft wood, to stop the exiting projectile and measure from the depth of penetration the residual projectile velocity, knowing the perforation depth for a direct shot without interposed

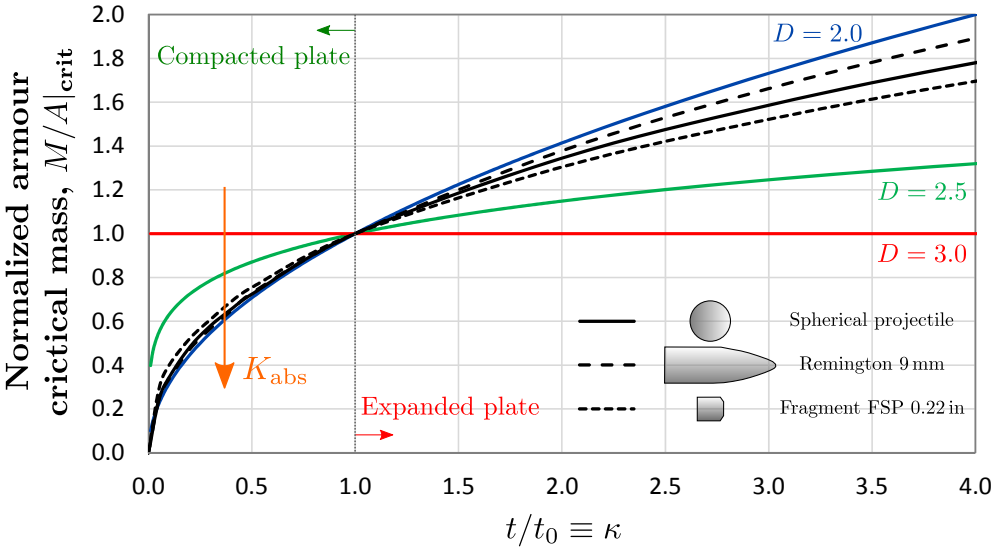

Figure 2.5: Scaling of the critical armour mass (minimum mass required to stop a projectile with a certain kinetic energy), normalized with respect to the critical mass for the nominal uncompacted plate $\kappa = 1$, as a function of the the compaction level κ. The three characteristic cases of fractal theory are compared to the result of the analytical impact model which implements LEFM, computed for the three analysed projectiles (frictionless contact assumed).

target. The two different tested projectiles were shot from a Trabzon gun at a distance of 5 m far from the targets. The impact velocities for the projectile and the fragment are reported in Table 2.2 in the Appendix as V_0 together with the plate characteristics and the output of analytical and FEM calculations. The results are in good agreement, despite the uncertainness in the material characterization, the statistical variation of properties due to the quality of the production process and the approximation of the analytical model which assumes material damage and fracture as predominant dissipation neglecting heat and propagation of the mechanical waves. A mismatch in only two targets (21 and 23, Table 2.2 in Appendix II) that actually had some issue during the curing procedures, as confirmed by the producer, further corroborates the predictive capability of the models.

Figure 2.6a reports the reconstruction of ballistic curves $V_{\text{res}} - V_0$ for the Angeloni aramid 170 based multilayers, namely the plates 8, 11, 13, and 15 (Appendix II). The curves at different compaction ratio κ are obtained with the analytical model. It emerges how, for a given impact velocity, the compacted plate is associated to a lower residual velocity of the impacting projectile. Figure 2.6b depicts the experimental images of the considered plates. Analytical predictions are compared with the experimental points and with the FEM simulation results for the uncompacted plate 11 ($\kappa = 1$) and for the compacted plate 8 ($\kappa = 0.83$). Looking at experimental data and photographs, the plate 8 is the only among the considered targets that is not perforated, despite the slightly higher impact velocity (+10 m/s) to which it is subjected. The best performance of plate 8 with respect to 13 and 15 could be explained with the greater cleavage temperature that could interact with the machine pressure to reduce defects allowing more homogeneous resin flow.

Finally, the model has been tested for also non normal impact configurations. Figure 2.7 shows the experimental results of oblique impact testing performed on the target 5 under different impact incidence θ ranging from 0° to 46°. Parallel, FEM simulations of configurations from 0° to 75° were performed and both results are compared with the trend predicted by the analytical model. The analytical predictions are in good agreement with both experiments and simulations. For incidence near to a pure tangential impact $\theta = 90^\circ$ the difference between the theory and the simulated impact becomes consistent: indeed, the inglobation and rotation of the projectile occur and the real phenomena progressively depart from hypotheses of the analytical model. In addition, the failure mechanism changes from a purely compression and shear rupture to a tension tear (inset in Figure 2.7) involving mainly the in-plane plate tensile strength, which is 2/3 times its corresponding compressive value for these kind of composites. In the analysed domain, the results are consistent with other experimental and numerical works on thin metallic target found in literature [91], which show a significant variation on the absorbed energy with respect to the normal impact configuration starting from incidence angles greater than $45 - 50^\circ$, with a trend up to 80° which is in qualitatively in good agreement with the analytical and numerical predictions of this work as depicted in Figure 2.7.

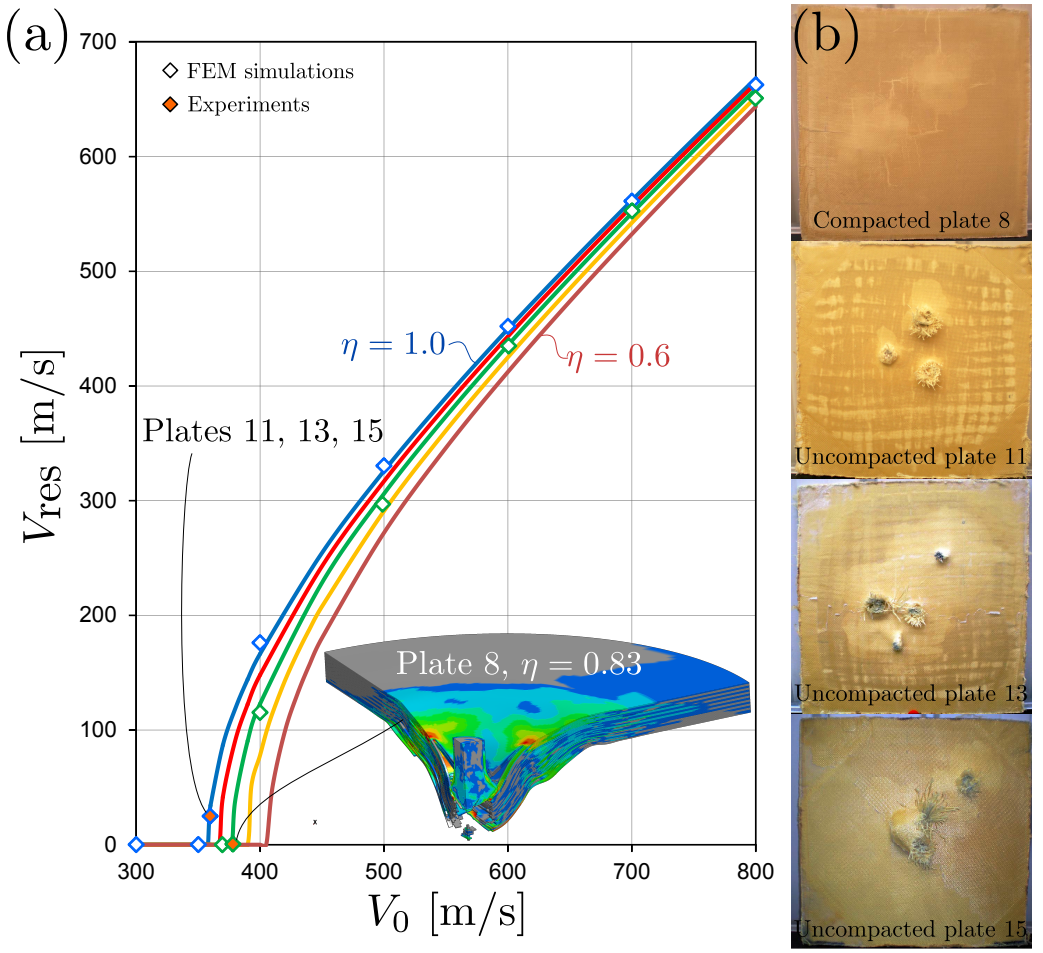

Figure 2.6: (a) Analytical ballistic curves at different compaction ratio κ compared with the results of finite element simulations (empty dots) and experiments on plate 8, 11, 13, 15 (filled dots), and corresponding (b) experimental images of the rear faces of targets after the impact of a Remington 9 mm projectile at 350 m/s. Images courtesy of Vemar Helments S.r.l, Italy.

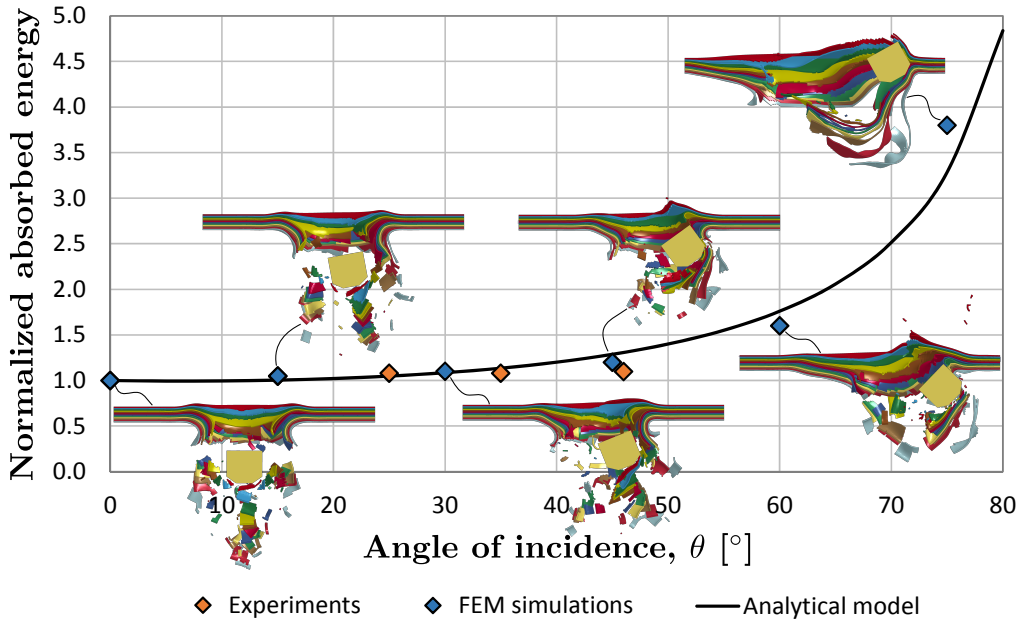

Figure 2.7: Analytical vs. numerical analysis of oblique impact showing the energy absorption (K_{abs}) normalized with respect to the normal impact case ($K_{\text{abs},0}$). The values refer to the plate 5 impacted at 360 m/s by the FSP. A visualisation of the simulations for each of the analysed incidence angle is depicted.

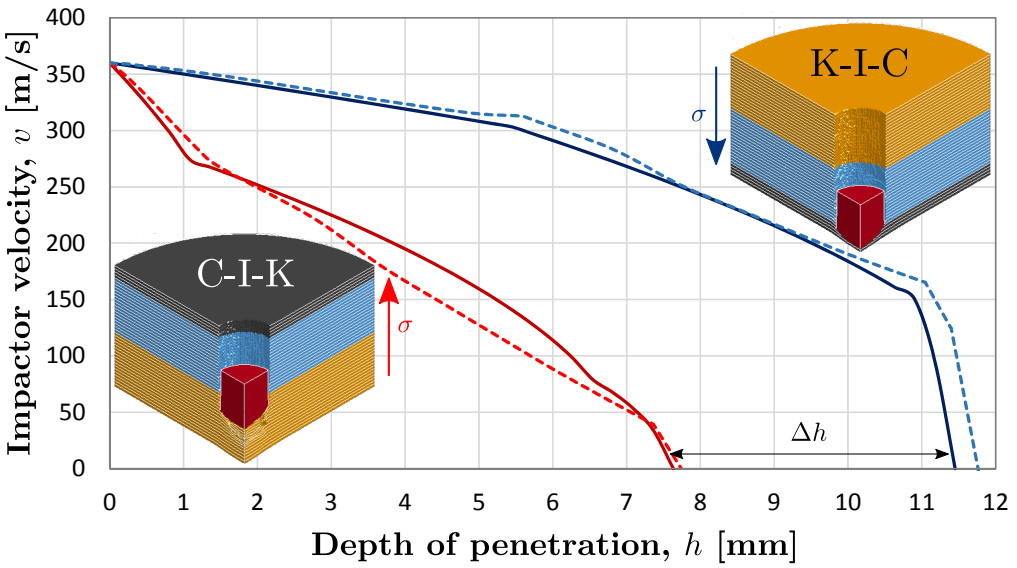

Figure 2.8: Evolution of the projectile velocity with its penetration depth for the plate 34 (heterogeneous stacking of Kevlar, Innegra and carbon-based composites) impacted by two opposite faces. Continuous line refers to the results of the analytical model, while the dashed line to FEM simulation. The graded solution with stronger materials at the front face provide the lowest depth of penetration, thus possesses the higher critical penetration energy.

2.4.2 Energy absorption scalings

Considering strain-rate effects on material strength introduced by Equation (2.2) in the form of quadratic dependence to the instantaneous relative velocity between the projectile and the target, it is expected that the absorption capacity of the backing layer progressively decreases due to the deceleration that the projectile experiences when perforating the target. In this scenario, the stacking sequence of the layer is also expected to affect the energy absorption, and then the projectile residual velocity. Indeed, assuming two materials with failure strength σ_1 and σ_2, with $\sigma_1 \geq \sigma_2$ and with the same quadratic scaling on the strain-rate, the model would predict that a plate with stacking sequence 1-2 would absorb more energy than the configuration 2-1. Hybrid plate 34 was a good candidate for the verification of such behaviour since composed by a total of 44 layers of three different material: 20 layer of Kevlar®, 20 of Innegra® and 4 of Carbon T300 with progressively increasing strength faced by the projectile (configuration denoted as K-I-C). Figure 2.8 shows the impactor velocity profile vs. its penetration h obtained from the analytical model and the FEM simulation on the two configuration. The actual

configuration K-I-C is compared then to the result for the opposite configuration C-I-K. Both experiments, analytical model and the numerical simulation provide a null residual velocity for the actual K-I-C configuration and a perforation of $\approx$ 42 layers over 44. For the C-I-K sequence, with decreasing material strength faced by the projectile, the model and the simulation predict again both no perforation with a total penetration of 29 only layers corresponding to a depth $H_{\text{C-I-K}} \approx 7.9\,\text{mm}$. Thus, a graded stacking with progressively decreasing material strength emerges to enhance the protection capability, as confirmed by both by our analytical model and the FEM simulation. Moreover, the velocity vs. penetration depth curves obtained by the two different tools are in very good agreement, thus the developed analytical model could be exploited for quick but reliable design and verification of protective capability of armours.

It is of primary interest in multilayer armours to know how the energy absorption capability scales with the addition of materials in order to understand if the material coupling is synergistic or not. A further consequence of previous considerations on strain-rate effects is that also in homogeneous target the back layers are espected to provide less energy absorption capability when moving through the thickness. Thus, considering a specific impact condition (i.e., projectile velocity, mass, geometry and incidence) with the addition of layer the total absorption capability, would certainly increase, but the total absorbed energy by the number of layer is expected to decrease. Generally speaking, we can express this concept by the following equation:

$$\frac{K_{\text{abs}}}{N} \propto N^{\alpha} \tag{2.23}$$

In Equation (2.23) a scaling exponent $\alpha > 0$ indicates a synergistic behaviour in which single layers interacts to mutually enhance their specific contribution. On the other hand, for $\alpha = 0$, the total absorbed energy is the mere sum of single-layer contributions, while for $\alpha < 0$ a sub-optimal behaviour is identified in which increasing the number of layers leads to an inefficient behaviour. The latter is the expected situation according to the hypothesis of our model, net of other source of dissipation such as mechanical waves or heat. Although, this scaling ($\alpha \leq 0$) can appear counter-intuitive, it is evidenced by experimental tests in literature. A meaningful example, which inspired this study, is the work by Jacobs and Van Dingenen [92] which investigated the penetration capabilities of armours with different areal density, obtained by changing the number of layers N. Two broad families of armours are studied in that work and addressed as "hard armours" and "soft armours". The first, which were subjected to curing during the production process, shows both positive and negative scaling in relation to the materials and impact condition. The latter, made by a simple packing of layers and not subjected to curing pressure and high temperature, thus possessing a very weak interlayer strength, showed negative values of α in all the tested configurations. Thus, it is evident how the characteristics of the interface, governed by the manufacturing process, have a fundamental role for the realization of an efficient multilayer armour.

To investigate this behaviour we studied the role of interface strength parameters, namely $\sigma_{\parallel}$ and $\sigma_{\perp}$ on the scaling exponent. An independent variation of the two parameters within the range $[0; \sigma_t]$, where σ_t is the homogenized tensile strength of the composite, was operated on a series of targets, based on the material of plate 8 and with variable number of layers (2, 4, 6, 8, 10, 12). Thus, it was assumed that the adhesive strength cannot overcome, reasonably, the strength of the material constituting the plies. The results are reported in Figure 2.9 showing the variation of α in the investigated domain. It is demonstrated how through the interface tuning it possible to obtain positive value of α that can even be maximized for certain interface parameters. $\alpha < 0$ is associated to very weak or very strong interfaces, confirming the behaviour observed experimentally in ref. [92]. The higher value of α, obtained for adhesive parameters in an intermediate configurations of normal and shear adhesive strength $\approx 0.5 \div 0.6 \cdot \sigma_t$, is around 0.15 (at V_0=350 m/s) which corresponds to an overall energy absorption 12% higher than the sum of the single layer (constant scaling) in the case that the number of layers is doubled. The role of the interface on the energy absorption is well elucidated by the insets images in Figure 2.9a. For very strong interfaces the target behaves as a monolithic plate, the projectile is able to pass concentrating the damage under its projected area and the deformation of the layers is limited. On the opposite, the optimal configuration is able to provide enough stability to the plate but guaranteeing delamination and deformation of the layers which contribute to energy dissipation. Different impacting velocities were also tested. Figures 2.9b-c show how the α exponent tends to flatten towards the constant scaling when increasing the impact velocity. Indeed, positive α tends to decrease due to the increasing localization for $V_0 \to \infty$, while the negative values tend to increase since the deceleration seen the projectile decreases and thus strain-rate differential tends to vanish. In conclusion, the effectiveness of the adhesive interface is not universal but depends on the system under consideration, namely the projectile impact kinetic energy, the material constituting the target, the ratio between the projectile characteristic dimension and the target thickness. The obtained results is of importance since demonstrates the existence of optimal interfaces that could be exploited for enhancing, even significantly, the protection capability of multilayer armours. While the precise quantification of the correlation between the parameters and setup used in the production process and the obtained interface properties could be a difficult task, bio-inspired structured interfaces (even hierarchical) with designed and controlled properties [3] could be proposed as viable and effective solution for this scope.

2.5 Conclusions

An analytical impact model to study the ballistic properties of multilayer armours has been developed. Shape, size, friction, and angle of incidence of the projectile are taken into account. The model, based on energy balance considerations, provides the residual velocity of perforating projectiles or the depth of penetration in case the impactor is stopped by the

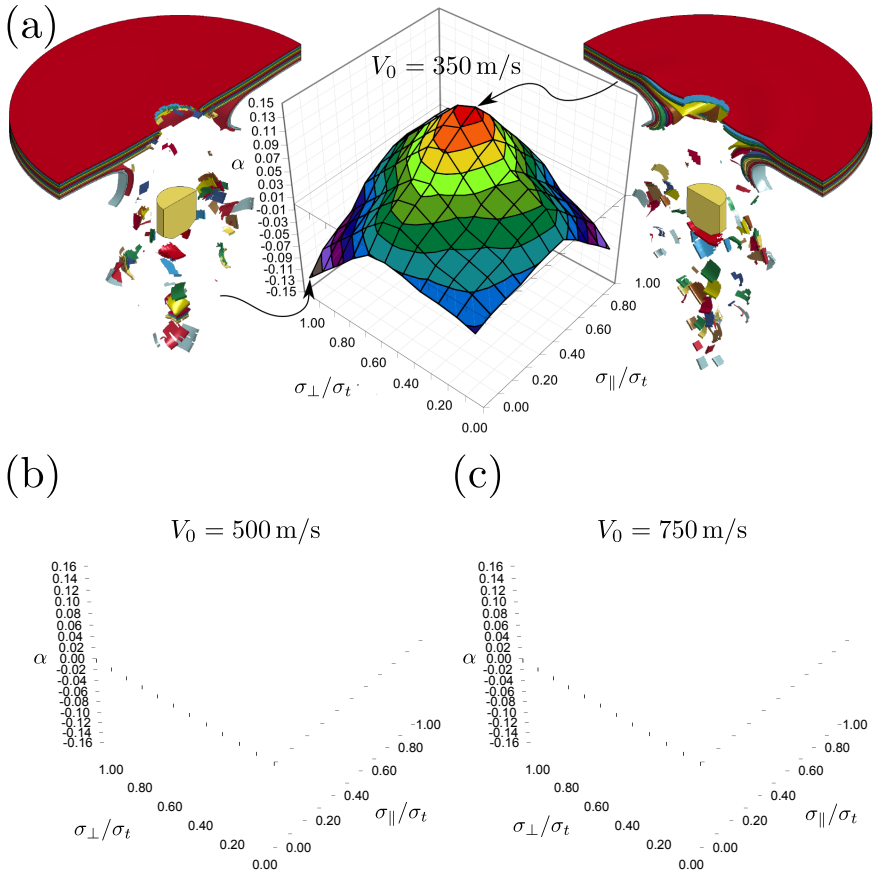

Figure 2.9: Scaling of the absorbed energy K_{abs} in perforated multilayer panels for different values of the interface adhesive normal limit stress $\sigma_\perp$ and shear $\sigma_\parallel$, normalized with respect to the homogenized tensile stress of the plate σ_t. Three cases corresponding to different projectile impact velocity are reported. (a) Case corresponding to V_0=350 m/s: the images of the target for the optimal and the worst configuration are reported showing the capability of the interface strength to govern the deformation behaviour of the multilayer. Each point of the graphs was computed extracting the scaling exponent from sets of 6 simulations with different number of layer N resulting in overall 726 simulations for each graph. Such a number of experimental trials would be extremely difficult to perform. (b) Variation of the scaling exponent α at V_0=500 m/s. (c) Variation of the scaling exponent α at V_0=700 m/s.

target. The scaling of armour thickness according to Linear Elastic Fracture Mechanics allows also to explain and quantify the beneficial effect of the thickness compaction observed in experimental ballistic tests. The analytical model and FEM simulations have been validated via an extensive ballistic experimental campaign on multilayer composite targets, being the prediction of residual velocity and damage in good agreement. Indeed, a mismatch of model results in only two plates over a total of 43 analysed let also to identify those plates with some issues in the production process. We find that a graded distribution of layers with different material strength in the thickness provide higher protection when the projectile first encounter plies with the higher failure strength. These observations explain common structural arrangements of biological armour and can be exploited in the design and optimization of lightweight protective structures. Through FEM simulations we have then showed that the energy absorption of the plate can be maximized for a specific impact configuration by setting proper interface strength parameters. These results give effective guidelines for the further optimization of currently employed multilayer armours.

Appendix I: Shape functions for the studied projectiles

In general, the integrals of Equations (2.24) must be solved numerically. In the case of a spherical projectile these shape yield the following closed-form expressions, integrating the curve $y = \sqrt{(x-R)^2 - R^2}$ for $x \in [0;R]$.

$$J_0 = \frac{\pi}{4}\mu R^2, \tag{2.24a}$$

$$J_1 = \left(\frac{1}{6} - \frac{\mu}{3}\right) R^2, \tag{2.24b}$$

$$J_2 = \left(\frac{1}{4} - \frac{\pi}{16}\mu\right) R^2. \tag{2.24c}$$

Note that there is no difference in the values of the shape functions between hollow and filled projectiles of equal external profile. Computed values for the three particular tested projectiles are reported in Table 2.1.

Table 2.1: Geometrical characteristics and resulting shape functions for the three studied projectiles.

Projectile type	Function [mm]	Domain [mm]	m [g]	R [mm]	J_0 [mm^2]	J_1 [mm^2]	J_2 [mm^2]
Spherical	$y=\sqrt{(x-R)^2-R^2}$	$x\in[0;R]$	4.110	5.000	19.635μ	$4.167-8.333\mu$	$6.250-4.909\mu$
FMJ 9 mm	$y=x^{1/3}$	$x\in[0;11.5]$	8.040	4.515	35.278μ	$6.315-8.825\mu$	$8.089-2.863\mu$
FSP 0.22 in	$y=0.7x+12.7$	$x\in[0;2.1]$	1.102	2.731	2.045μ	$0.035-0.113\mu$	$0.065-0.092\mu$

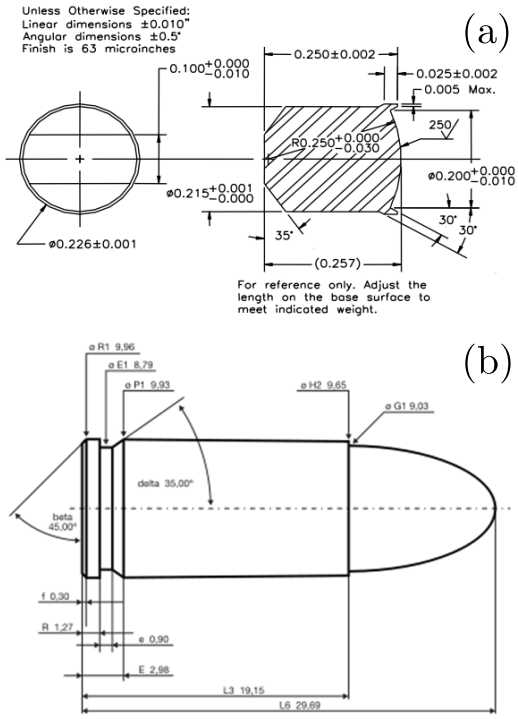

Figure 2.10: Geometrical quotes of fragment FSP caliber 0.22 in [9] and (b) of the Remington 9 mm FMJ [10].

Appendix II: Comparison between the analytical, simulation, and ballistic experimental results

Table 2.2: Summary of characteristics, properties, and test results for the 43 composite targets tested in the ballistic experiments. For each sample are reported the code specification of the textile by the producer, the geometry of the target (in-plane dimension b_1 and b_2, thickness t, and the number of layer N), the plate composition (the densities ρ of the target and of the textile, the weights W of the epoxy and of the textile), the production process parameters used for cleavage and curing (pressure p, temperature T, and time). The fibre volume fraction was determined a posteriori from the geometry of the target and the weight of resin and textile. The epoxy resin, wherever present, is a Bakelite® EPR L 1000 set with density $1135\,\mathrm{kg/m^3}$ and 72.3 MPa of tensile strength. For each target is then reported the initial impact velocity of the Remington 9 mm projectile or of the fragment (when actually tested) and the residual velocity $V_{\mathrm{res,exp}}$ measured in experiments and determined from the analytical model and FEM simulations ($V_{\mathrm{res,an}}$ and $V_{\mathrm{res,sim}}$ respectively). For the fragment, PP identifies a partial perforation with complete stop of the projectile while CP means a complete perforation ($H \equiv t$). Finally, for each plate the critical thickness, that is the minimum thickness required to stop the projectile/fragment, is determined.

		Geometry			Composition				Process parameters			Projectile				Fragment				
ID	Textile	b_1xb_2 [mm^2]	t [mm]	N	ρ [kg/m^3]	W_{epoxy} [g]	$W_{textile}$ [g]	$\rho_{textile}$ [kg/m^3]	p [bar]	T [°C]	time [min]	V_0 [m/s]	$V_{res,exp}$ [m/s]	$V_{res,an}$ [m/s]	$V_{res,sim}$ [m/s]	V_0 [m/s]	$V_{res,exp}$ [m/s]	$V_{res,an}$ [m/s]	$V_{res,sim}$ [m/s]	t_{crit} [mm]
1	DuPont Kevlar XP prepreg	370x370	3	17	1826	n.a.	n.a.	n.a.	80	130	10	360	110	120	117	-	-	-	-	3.5
2	DuPont Kevlar XP prepreg	370x370	2	10	1644	n.a.	n.a.	n.a.	80	130	10	360	221	233	224	-	-	-	-	3.8
3	SAATI Kevlar KQX 240	370x370	6	21	1290	350	710	247	30	80	20	360	55	57	58	-	-	-	-	6.3
4	Glass Angeloni VV - 300P	370x370	3	16	2277	130	690	315	80	80	20	360	110	126	115	-	-	-	-	3.6
5	Carbon Angeloni GG 301 T8	370x370	4	17	2009	180	745	320	80	80	20	360	110	106	103	-	-	-	-	4.7
6	Carbon Angeloni GG 240 T	370x370	4	21	1797	180	690	240	80	80	20	360	166	205	161	-	-	-	-	3.1
7	Carbon Angeloni GG 240 T	370x370	10	21	804	250	690	240	0	0	0	360	193	194	203	-	-	-	-	16.2
8	Angeloni aramid style 170	370x370	5	30	1490	370	698	170	80	80	20	370	0	0	0	-	-	-	-	4.5
9	SAATI Kevlar KQX 240	370x370	4	21	2009	350	710	247	80	80	20	360	138	110	121	-	-	-	-	4.8
10	SINCERT polyethylene tissue	370x370	7	9	1054	250	1010	950	80	80	20	360	0	0	0	-	-	-	-	4.7
11	Angeloni aramid style 170	370x370	5	30	1439	280	698	170	80	75	20	360	27	0	3	-	-	-	-	4.5
12	Angeloni aramid style 170	370x370	10	30	877	360	698	170	80	75	20	360	0	0	0	-	-	-	-	9.7
13	Angeloni aramid style 170	370x370	7	30	1419	410	698	170	80	75	20	360	27	61	34	-	-	-	-	7.5
14	Angeloni aramid style 170	370x370	5	30	1607	230	698	170	80	75	20	360	27	0	0	-	-	-	-	4.3
15	Angeloni aramid style 170	370x370	5	30	1508	370	698	170	80	75	20	360	27	0	0	-	-	-	-	4.3
16	Angeloni aramid style 170	370x370	5	30	1432	210	698	170	80	75	20	360	0	0	0	-	-	-	-	4.5
17	Teinjin prepreg twaron	400x400	4	10	1141	n.a.	n.a.	n.a.	60	170	15	360	0	0	0	-	-	-	-	6.4
18	Teinjin prepreg twaron	400x400	5	12	1088	n.a.	n.a.	n.a.	60	170	15	360	0	0	0	-	-	-	-	7.1
19	Teinjin prepreg twaron	400x400	8	18	1016	n.a.	n.a.	n.a.	60	170	15	360	0	0	0	-	-	-	-	7.6
20	Montefibre Fidion	400x400	8	10	629	0	687	629	100	100	3	360	0	0	0	-	-	-	-	8.0
21	Angeloni aramid style 170	370x370	5	25	1271	220	582	170	80	80	20	360	0	126	103	-	-	-	-	6.0
22	Angeloni aramid style 170	370x370	5	30	1622	435	698	170	80	80	15	360	0	0	0	-	-	-	-	4.3
23	Angeloni aramid style 170	370x370	4	20	1359	220	465	170	80	80	20	360	27	182	150	-	-	-	-	6.0
24	Angeloni aramid style 170	370x370	5	30	1537	270	698	170	60	80	20	360	0	0	0	-	-	-	-	4.3
25	Angeloni aramid style 170	370x370	5	30	1633	330	698	170	40	80	20	360	0	0	0	-	-	-	-	4.3
26	Angeloni aramid style 170	370x370	6	30	1346	325	698	170	20	80	20	360	0	0	0	-	-	-	-	6.0
27	Polyetilene AB26-UD	176x188	3	20	1854	0	175	264	0	0	0	360	0	0	0	-	-	-	-	2.7
28	Dyneema HB80 UD	170x170	6	10	531	0	42	145	0	0	0	360	0	0	0	-	-	-	-	5.4
29	Lenzi Egisto Dynafelt 400	370x370	8	12	968	390	670	408	100	75	20	360	27	57	44	-	-	-	-	8.7
30	Lenzi Egisto Innegra	370x370	7	18	981	200	678	275	80	75	20	360	27	39	42	-	-	-	-	7.4
31	Polyetilene UD fabric	200x400	8	40	883	0	528	165	80	75	20	360	0	0	0	-	-	-	-	3.1
32	UD Kevlar fabric	200x400	7	60	955	0	1056	220	80	75	20	360	0	0	0	-	-	-	-	4.0
33	Dyneema HB80 UD	400x400	6	43	1025	0	998	145	150	100	20	360	0	0	0	710	PP	0	0	5.2/4.3
34	Angeloni aramid style 170 Lenzi Egisto Innegra Carbon Angeloni GG 301 T8	370x370	3 8 1	20 20 4	1029	296	1394	170 275 320	100	80	20	388	0	0	0	-	-	-	-	8.0
35	Dyneema HB80 UD	400x400	6	43	1024	0	1011	147	150	100	20	393	0	0	0	710	PP	0	0	6.0/4.3
36	Dyneema HB80 UD	400x400	7	47	971	0	1105	147	170	110	25	392	0	0	0	804	PP	0	0	6.1/5.4
37	Dyneema HB80 UD	370x370	7	45	1148	0	906	147	100	0	10	390	0	0	0	-	-	-	-	5.8
38	Dyneema HB80 UD	400x400	8	56	1035	0	1317	147	150	100	20	352	0	0	0	850	PP	0	0	5.0/4.9
39	Dyneema HB80 UD	400x400	9	59	966	0	1388	147	170	110	25	358	0	0	0	870	PP	0	0	5.3
40	Polyetilene UD Fabric	370x370	8	50	1004	0	1129	165	100	55	45	-	-.	-	-	720	CP	0	0	4.5
41	Polyetilene UD Fabric	370x370	8	45	940	0	1016	165	155	55	45	390	0	0	0	-	-	-	-	5.5
42	Polyetilene UD Fabric	370x370	8	45	959	0	1016	165	155	55	45	360	0	0	0	-	-	-	-	6.2
43	Polyetilene UD Fabric	370x370	7	45	1052	0	1016	165	100	55	50	-	-	-	-	720	CP	0	0	4.2

Chapter 3

Hybrid 2D materials multilayer armours

In this chapter the ballistic behaviour of 2D materials-based armours upon the hypervelocity impact of fullerene (C_{60}) is investigated by FEM and analytical modelling. FEM model were calibrated and validated by *ab initio* DFTB simulations. The critical penetration energy of monolayer membranes is determined, using graphene and the 2D allotrope of boron nitride as case studies. Multilayer armour configurations, including heterogeneous mixing of layered materials (alternate stacking of graphene and h-BN), are then analysed in order to understand the scaling of energy absorption capabilities with variable number of layers. *ab initio* computer simulations are supported and extended across dimensional scales by FEM and continuum models and compared with the experimental and simulation data available in the literature [12, 13]. DFTB calculations presented in this work were performed by Dr. Simone Taioli (European Centre for Theoretical Studies in Nuclear Physics and Related Areas, Fondazione Bruno Kessler & Trento Institute for Fundamental Physics and Applications, Trento, Italy) who is gratefully acknowledged for providing data and results functional to the validation of FEM models and analytical calculations.

3.1 Introduction

Spacecrafts are commonly exposed during their operation to hypervelocity collisions (velocities $\geq 7-8\,\mathrm{km\,s^{-1}}$) of micrometeoroids or orbital debris [14], leading to surface degradation, on-board instrumentation failures, up to complete perforation and structural damage. Other applications where impact assessment shows great deal of interest are in the field of stretchable and wearable electronics [93], where devices may undergo several and severe accidental shocks during their service life. Protection with a massive shield is straightforward but is often impracticable since lightness, flexibility, and ergonomics are of paramount importance in all these applications. Thus a growing interest towards

the development of unconventional nanocomposites having high specific toughness and low weight has been witnessed. Solutions that embed 2D nanomaterials layers [94, 95] exploiting size-scale effects on mechanical properties are ideal candidates for such applications, increasing the resistance to shock loads while keeping the required flexibility. Furthermore, the possibility to exploit properties of embedded nano-material beyond the typically structural function [96] can lead to further lightening of the system.

Among these materials, graphene, along with extraordinary thermal, optical [97, 98], and electrical properties [99, 100], shows outstanding strength ($\sigma \approx 130\,\mathrm{GPa}$) and Young's modulus ($E \approx 1\,\mathrm{TPa}$) [23] coupled with relatively low density ($\approx 2200\,\mathrm{kg/m^3}$). Recalling the Cuniff's criterion introduced in the previous chapter [64, 65], graphene embedded into a composite material is an ideal candidate for impact protection, reaching for the monolayer unprecedented values of $U = \frac{\sigma\varepsilon}{2\rho}\sqrt{\frac{E}{\rho}} \approx 0.8\,10^{11}\mathrm{m^3/s^3}$ (ε=0.13). Indeed, it has been reported that addition of graphene sheets in the conventional composite materials effectively increases their ballistic resistance [101]. Other 2D materials such as the hexagonal allotrope of boron-nitride (h-BN) [102] or the molybdenum disulfide (MOS_2) [103] also possess excellent tensile properties and are equally promising. However the values of their tensile properties are somewhat lower than graphene and studies on these materials have been discarded also by the overwhelming interest in graphene-based structures.

While computational modelling of defect-free structures can overestimate the mechanical properties of actual 2D-materials, however they usually outperform those of materials traditionally employed as energy absorbers, being able to guarantee the same level of protection against penetrating masses at $\approx 1/100$ of weight. Indeed, remarkable properties have been confirmed by analytical methods based on continuum theories [104, 105] and computational atomistic models [51] also in the presence of defects [25] and in out-of-equilibrium configurations [106]. In particular, layered graphene has been the subject of intensive experimental [12, 107] and computational [13, 53, 108] investigations to evaluate its performance as ballistic material, showing great potential for its use in these applications. However, discrepancies in energy absorption capabilities between the atomistic scale and the micro-scale were reported, suggesting the presence of scaling effects.

3.2 Finite element model

Continuum models based on finite element method were developed and used to complement first-principles simulations. Indeed a major goal of this work was to build and calibrate a computational tool based on continuum mechanics to investigate impact problems on nano-membranes at lower computational cost. For DFTB simulation detail we remind to the reference paper [109]. The graphene and h-BN membranes were modelled with thin shell elements with graphene and h-BN layer having respectively a nominal

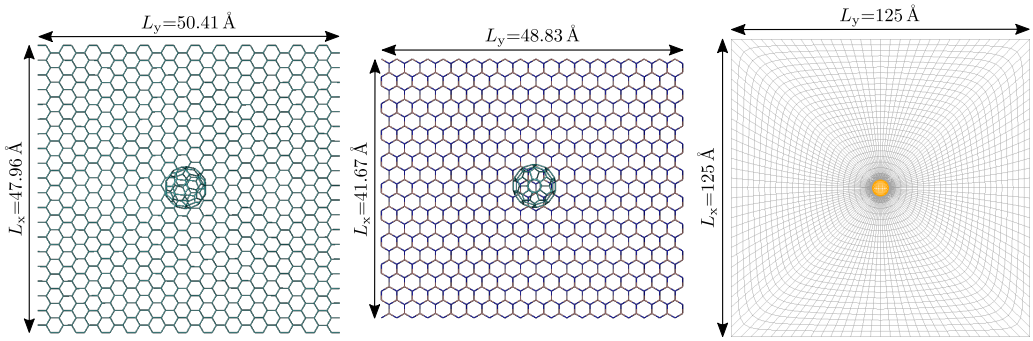

Figure 3.1: Sketch of the single-layer nanomembrane geometries. From left to right: supercell of graphene, h-BN, and the FEM membrane model used for both materials. The impacting fullerene spherical projectile is also depicted.

thickness of 3.415 Å and 3.407 Å, which correspond to their inter-layer equilibrium distance [110]. The fullerene spherical impactor was modelled as a rigid shell body, having an external radius of 5.05 Å. The geometries of the nanoscale membranes are reported in Figure 3.1.

The nanomembranes were modelled with fully integrated shells (2x2 Gauss points) based on the Reissner–Mindlin kinematic assumption. Since the graphene is assumed to experience large strains at impact, the constitutive response of the material is assumed to be elastic and isotropic with a non-linear law of the type $\sigma = E\varepsilon + B\varepsilon^2$ [111] where σ is the symmetric second Piola-Kirchhoff stress, ε is the uniaxial Lagrangian strain, E is the linear elastic modulus, and B is the third-order non-linear elastic modulus. The law parameters for both graphene and boron nitride are determined according to DFT computations available elsewhere [51, 112]. The densities are $\rho_{\mathrm{G}} = 2.2\,\mathrm{g/cm^3}$, and $\rho_{\text{h-BN}} = 2.1\,\mathrm{g/cm^3}$ [23, 112] for graphene and h-BN respectively. Material failure was treated via an erosion algorithm based on the Lagrangian uniaxial strain ε. When the failure condition is reached at one of the element integration point, the element is deleted from the simulation (elastic strain energy properly accounted in the computations) and thus fracture can nucleate and propagate.

The molecular van der Waals (vdW) interactions between the graphene and h-BN layers and with the fullerene projectile were taken into account with a cohesive model on the basis of the work by Jiang et al. [113], under the hypothesis that the layers have an infinite extension in the plane xy. Considering two layers, the homogenized cohesive energy per unit area, function of the distance r between two pair nodes, is the sum of the contributions of the potential energy $\Pi(r)$ of the n atomic pairs a-b (C-C, B-B, N-N, C-B, C-N, B-N):

$$\Phi = \sum_{i=1}^{n} 2\pi\psi_{i,(\mathrm{a})}\psi_{i,(\mathrm{b})}\int_0^{\infty}\Pi_i(r)r\mathrm{d}r \tag{3.1}$$

where, in our case, $\Pi(r)$ is a Lennard-Jones 6-12 functional form. The ψ are the homogenization parameters for the material of the two layers to spread the discrete interaction of $\Pi(r)$ over a continuum equivalent surface. In particular, $\psi = \Gamma/(3\sqrt{3}l_0^2)$ has the meaning of number of atoms per unit area, being l_0 the equilibrium C-C or B-N bond lengths before deformation, $\Gamma = 4$ for C atoms in the graphene lattice and $\Gamma = 2$ for B and N in the h-BN lattice. The cohesive stress-layer separation law is then obtained from derivation of the cohesive energy with respect to the normal and shear interface displacement. The interlayer bonding interaction between graphene and h-BN layer is due to van der Waals interaction [114], which can be represented by the following canonic Lennard-Jones 6–12 potential law:

$$\Pi(r) = 4\varepsilon\left(\frac{s^{12}}{r^{12}} - \frac{s^6}{r^6}\right), \tag{3.2}$$

being r the spatial distance between two pair atoms, $\sqrt[6]{2}s$ is the equilibrium distance between the two atoms, ε the corresponding energy . These parameters for the interaction between carbon, nitrogen and boron atoms [115, 116] are reported in the Table 3.1.

The cohesive energy $\Phi_{\text{G/G}}$ between two graphene layers can be derived by including the expression of $\Pi(r)$ of Equation (3.2) within the energy per unit area of Equation (3.1). At the equilibrium distance $h_{\text{G/G}}$ the cohesive energy for the graphene-graphene interaction is expressed by the following relation:

$$\Phi_{\text{G/G}} = 2\pi\psi_{\text{C}}^2\varepsilon_{\text{C-C}}s_{\text{C-C}}^2\left(\frac{2s_{\text{C-C}}^{10}}{5h_{\text{G/G}}^{10}} - \frac{s_{\text{C-C}}^4}{h_{\text{G/G}}^4}\right). \tag{3.3}$$

Note that any arbitrary potential $\Pi(r)$ could be used in place of the Lennard-Jones. The equilibrium distance between two graphene sheets (that is along the direction perpendicular to the layers surface) can be derived imposing $\frac{\mathrm{d}\Phi_{\text{G/G}}}{\mathrm{d}h} = 0$, obtaining an equilibrium distance $h_{\text{G/G}} \equiv s_{\text{C-C}}$. This is the spacing used in the FEM method models at the beginning of simulations.

For sliding and normal perturbation relative displacement between a pair of nodes of the two layers, u and v respectively, beyond the equilibrium distance the Equation (3.3) is generalized as:

$$\Phi_{\text{G/G}}(u,v) = 2\pi\psi_{\text{C}}^2\varepsilon_{\text{C-C}}s_{\text{C-C}}^2\left(\frac{2s_{\text{C-C}}^{10}}{5(h_{\text{G/G}}+v)^{10}} - \frac{s_{\text{C-C}}^4}{(h_{\text{G/G}}+v)^4}\right), \tag{3.4}$$

where $u = \sqrt{\Delta x^2 + \Delta y^2}$ from the two components of the in-plane displacement Δx and Δy. The normal and shear cohesive stresses can be obtained by derivation of the cohesive energy with respect to the corresponding displacement, thus u and v respectively:

$$\sigma_{\text{cohesive,G/G}} = \frac{\partial\Phi_{\text{G/G}}(u,v)}{\partial v} = 8\pi\psi_{\text{C}}^2\varepsilon_{\text{C-C}}s_{\text{C-C}}\left(\frac{s_{\text{C-C}}^5}{(h_{\text{G/G}}+v)^5} - \frac{s_{\text{C-C}}^{11}}{(h_{\text{G/G}}+v)^{11}}\right), \tag{3.5a}$$

$$\tau_{\text{cohesive,G/G}} = \frac{\partial \Phi_{\text{G/G}}(u,v)}{\partial u} = 0, \tag{3.5b}$$

from which it can be seen that the tangential cohesive stress vanishes. For the coupling of graphene and h-BN layers the energy per unit area $\Phi_{\text{G/h-BN}}$ in a non-equilibrium configuration is given by:

$$\begin{aligned}\Phi_{\text{G/h-BN}}(u,v) &= \Phi_{\text{C-N}}(u,v) + \Phi_{\text{C-B}}(u,v) \\ &= 2\pi\psi_{\text{C}}\psi_{\text{N}}\varepsilon_{\text{C-N}}s_{\text{C-N}}^2\left(\frac{2s_{\text{C-N}}^{10}}{5(h_{\text{G/h-BN}}+v)^{10}} - \frac{s_{\text{C-N}}^4}{(h_{\text{G/h-BN}}+v)^4}\right) \\ &+ 2\pi\psi_{\text{C}}\psi_{\text{B}}\varepsilon_{\text{C-B}}s_{\text{C-B}}^2\left(\frac{2s_{\text{C-B}}^{10}}{(h_{\text{G/h-BN}}+v)^{10}} - \frac{s_{\text{C-B}}^4}{(h_{\text{G/h-BN}}+v)^4}\right),\end{aligned} \tag{3.6}$$

with:

$$h_{\text{G/h-BN}} = \left(\frac{\varepsilon_{\text{C-N}}s_{\text{C-N}}^{12} + \varepsilon_{\text{C-B}}s_{\text{C-B}}^{12}}{\varepsilon_{\text{C-N}}s_{\text{C-N}}^{6} + \varepsilon_{\text{C-B}}s_{\text{C-B}}^{6}}\right)^{1/6}. \tag{3.7}$$

The normal and shear cohesive stresses can be obtained again by derivation of the cohesive energy with respect to the corresponding displacement:

$$\begin{aligned}\sigma_{\text{cohesive, G/h-BN}} &= \frac{\partial \Phi_{\text{G/h-BN}}(u,v)}{\partial v} \\ &= 8\pi\psi_{\text{C}}\psi_{\text{N}}\varepsilon_{\text{C-N}}s_{\text{C-N}}\left(\frac{s_{\text{C-N}}^5}{(h_{\text{G/h-BN}}+v)^5} - \frac{s_{\text{C-N}}^{11}}{(h_{\text{G/h-BN}}+v)^{11}}\right) \\ &+ 8\pi\psi_{\text{C}}\psi_{\text{B}}\varepsilon_{\text{C-B}}s_{\text{C-B}}\left(\frac{s_{\text{C-B}}^5}{(h_{\text{G/h-BN}}+v)^5} - \frac{s_{\text{C-B}}^{11}}{(h_{\text{G/h-BN}}+v)^{11}}\right),\end{aligned} \tag{3.8a}$$

$$\tau_{\text{cohesive,G/h-BN}} = \frac{\partial \Phi_{\text{G/h-BN}}(u,v)}{\partial u} = 0. \tag{3.8b}$$

Finally, for the coupling h-BN layers the cohesive stress can be, derived in an analogous way, an is given by:

$$\begin{aligned}\sigma_{\text{cohesive,h-BN/h-BN}} &= 8\pi\psi_{\text{N}}^2\varepsilon_{\text{N-N}}s_{\text{N-N}}\left(\frac{s_{\text{N-N}}^5}{(h_{\text{h-BN/h-BN}}+v)^5} - \frac{s_{\text{N-N}}^{11}}{(h_{\text{h-BN/h-BN}}+v)^{11}}\right) \\ &+ 16\pi\psi_{\text{N}}\psi_{\text{B}}\varepsilon_{\text{N-B}}s_{\text{N-B}}\left(\frac{s_{\text{N-B}}^5}{(h_{\text{h-BN/h-BN}}+v)^5} - \frac{s_{\text{N-B}}^{11}}{(h_{\text{h-BN/h-BN}}+v)^{11}}\right) \\ &= 8\pi\psi_{\text{B}}^2\varepsilon_{\text{B-B}}s_{\text{B-B}}\left(\frac{s_{\text{B-B}}^5}{(h_{\text{h-BN/h-BN}}+v)^5} - \frac{s_{\text{B-B}}^{11}}{(h_{\text{h-BN/h-BN}}+v)^{11}}\right).\end{aligned} \tag{3.9a}$$

$$\tau_{\text{cohesive,h-BN/h-BN}} = \frac{\partial \Phi_{\text{h-BN/h-BN}}(u,v)}{\partial u} = 0. \tag{3.9b}$$

Figure 3.2 depicts the cohesive laws obtained from Equations (3.5a) (3.8a) (3.9a). The cohesive energy is weighted on each node of the mesh assuming that the area of influence of the node is defined by the centroids of the adjacent finite elements. It can be easily computed that the energy vanishes starting from $r \approx 3h$ (Figure 3.2), which was thus set as cutoff distance for the computation of the cohesive stresses.

Table 3.1: Characteristic parameters for the Lennard-Jones 6-12 potential for the possible interactions in graphene and h-BN hybrid coupling.

vdW bond	ε [eV]	s [nm]	Ref.
C-C	0.002390	0.3455	[115]
N-N	0.006283	0.3365	[116]
B-B	0.004117	0.3453	[116]
C-N	0.004068	0.3367	[116]
C-B	0.003294	0.3411	[116]
N-B	0.005084	0.3409	[116]

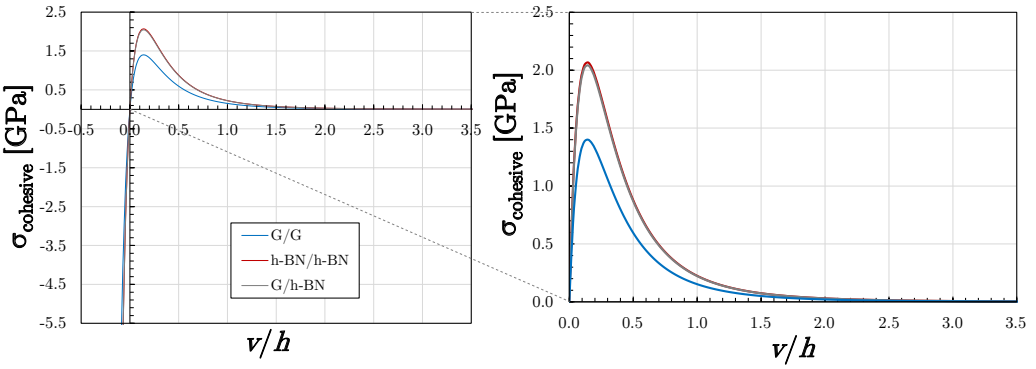

Figure 3.2: Plot of the normal cohesive stress law (σ_{cohesive}) as a function of the normalised interlayer normal separation v/h for G/G, h-BN/h-BN, and G/h-BN interactions. Positive values of v and σ_{cohesive} denotes layer separation and cohesive tractions, respectively.

3.3 Results

3.3.1 Ballistic properties of the single layers

To compare the response of different thin armours upon impact it is a customary in ballistic analysis to plot the projectile residual velocity V_{res} against its initial impact value V_0. This representation, also known in the field as ballistic curve, easily enables to discriminate

Table 3.2: Residual kinetic energy (K_{res}) and velocity (V_{res}) obtained from DFTB and FEM impact simulations on single layer graphene and h-BN.

		Graphene		Boron nitride		Method
K_0 **[eV]**	V_0 **[km/s]**	K_{res} **[eV]**	V_{res} **[km/s]**	K_{res} **[eV]**	V_{res} **[km/s]**	
33.63	3.0	-1.30	-0.59	-0.03	-0.09	DFTB
59.78	4.0	-2.47	-0.81	-0.14	-0.19	DFTB
93.41	5.0	-4.30	-1.07	-2.00	-0.73	DFTB
134.51	6.0	-6.43	-1.31	-4.83	-1.14	DFTB
183.09	7.0	-8.41	-1.50	-5.37	-1.20	DFTB
209.88	7.5	-8.07	-1.47	0.00	0.00	FEM
239.13	8.0	-7.52	-1.42	9.42	1.59	DFTB
302.65	9.0	-4.60	-1.11	51.15	3.70	FEM
336.73	9.5	0.00	0.00	79.06	4.60	FEM
373.64	10.0	11.15	1.73	113.85	5.52	DFTB
451.47	11.0	75.33	4.49	187.82	7.09	FEM
630.56	13.0	253.08	8.23	364.73	9.88	FEM
839.50	15.0	462.86	11.13	575.44	12.41	DFTB

between the projectile bouncing (*ricochet*) and the penetration regimes, thus identifying the critical penetration energy of the target [16, 19, 28]. The initial velocity of the fullerene centre of mass (V_0) is imposed within the range $3 \div 15\,\text{km/s}$ orthogonally to the substrate layers (normal impact condition). The projectile residual centre of mass kinetic energy (K_{res}) and velocity (V_{res}) are intended respectively as the translational kinetic energy and velocity that the fullerene centre of mass (COM) reaches asymptotically after the collision. In DFTB simulations COM kinetic energy is calculated as difference between the total energy of the fullerene and its internal energy, the latter being associated to the molecule shape distortion. A value very close to 0 eV of the COM kinetic energy represents the fullerene molecule embedded in the layer and "almost at rest". The resulting ballistic curves for the graphene and h-BN monolayers are reported in the left panel of Figure 3.3, while the corresponding numerical values of V_{res} and K_{res} can be found in Table 3.2.

In order to rationalize we recall the model based on energy conservation presented in the previous chapter and applied to a single layer. The initial impact kinetic energy K_0, associated to the centre of mass, is dissipated by the membrane after the complete projectile penetration by failure of a volume of material defined by the layer thickness and the damaged area. Referring to the fullerene COM kinetic energies:

$$K_0 - K_{\text{res}} = \frac{1}{2} m {V_0}^2 - \frac{1}{2} m {V_{\text{res}}}^2 = \eta \sigma \pi R^2 t, \tag{3.10}$$

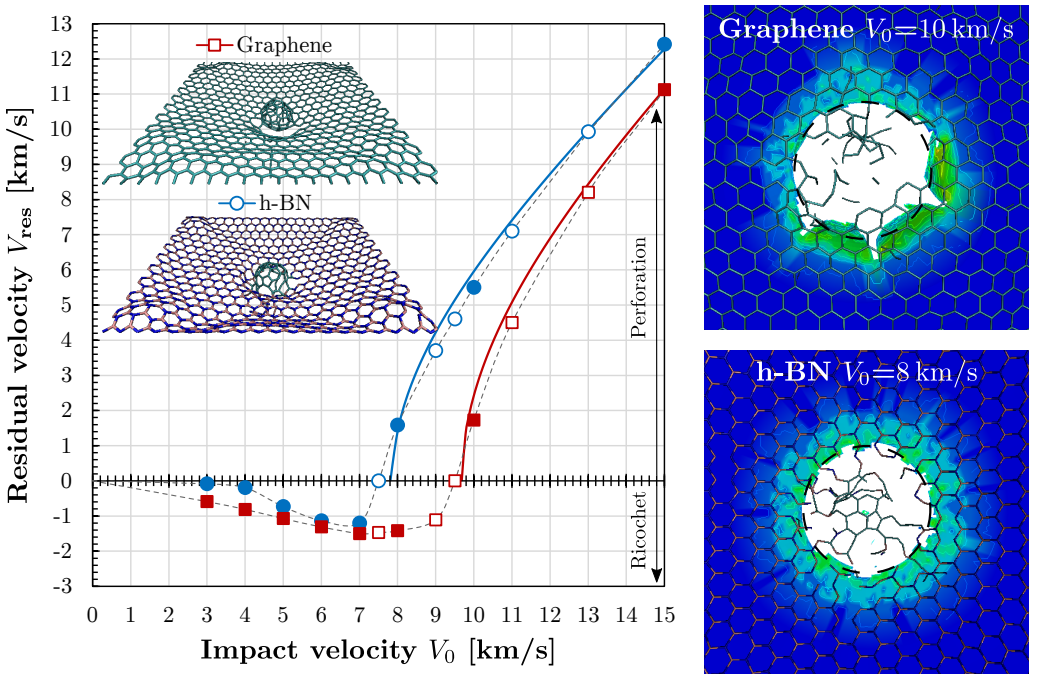

Figure 3.3: Left panel: ballistic curves of single layer graphene and h-BN, from DFTB (filled dots) and FEM (empty dots) simulations. The residual velocity V_{res} is referred to the C_{60} centre of mass. Graphene provides a higher limit penetration velocity (and impact energy) than h-BN monolayer. Consequently, graphene provides lower residual velocity V_{res} at perforation and a higher restitution coefficient in the ricochet regime. The dashed lines represent a guide to the eye while the continuous lines are derived from Equation (3.11) on the data corresponding to penetration regime. Right panel: configurations of graphene and h-BN at the penetration limit velocity with comparison between DFTB and FEM simulations. The contour plot of von Mises stresses from FEM is also depicted. The equivalent damaged areas are highlighted and have a radius of 6.65 Å for graphene and 6.39 Å for boron nitride and are used for determining the material impact strength σ. Atomistic simulation data and images by Dr. Simone Taioli.

where σ is the impact strength of the 2D-membrane, t its thickness, and η is a damage parameter, whose physical meaning is the ratio between the effective damaged area of the perforated membrane versus the fullerene projected area πR^2 ($R = 5.1$ Å is the fullerene outer radius in the undeformed configuration, given by the sum of the half nucleus-to-nucleus fullerene diameter of 7.1 Å and the mean carbon vdW radius of 1.62 Å [117]). In order to include energy dissipation beyond the model considered here, the Equation (3.10) can be generalized as [29]:

$$V_{\text{res}} = \gamma \left(V_0^p - \frac{p(\sigma \eta \pi R^2 t)}{m} \right)^{\frac{1}{p}}, \tag{3.11}$$

where p is theoretically equal to 2 for rigid projectile, and γ is a model-dependent coefficient, which is equal to unity assuming that dissipation is due to target deformation and projectile damage is not taken into account, as in Equation (3.10). From the best-fit of simulation data (Figure 3.5) corresponding to the penetration regime we find $\gamma \approx 0.975$, 0.958 and $p \approx 2.003$, 2.005 for graphene and h-BN respectively. The impact strength can be estimated from the intercept of the linear fit of the $K_{\text{res}} - K_0$ curve (see Figure 3.5). In order to get a precise estimate of η the actual damaged area was computed by measuring the mass of the eroded elements in the FEM simulations: we find $\eta_{\text{G}} = 3.61$ and $\eta_{\text{h-BN}} = 3.33$ for graphene and h-BN respectively corresponding to equivalent radii of the damaged area $R_{\text{G}} = 6.65$ Å and $R_{\text{h-BN}} = 6.39$ Å. Note that the damaged area increases, not monotonically, with the projectile impact energy (see Figure 3.4) and the previous estimation refers to the critical penetration condition, corresponding to the measure of the intercept. In this way, we derive an impact strength $\sigma_{\text{G}} \approx 125$ GPa for graphene and $\sigma_{\text{h-BN}} \approx 91$ GPa. The estimated values are comparable with the tensile strength of the two materials, namely 130 GPa for graphene [23] and 108 GPa for h-BN [118].

These results show that graphene is tougher than h-BN, being higher the minimum (critical) initial energy K_{c} necessary to the fullerene molecule to penetrate the layer ($K_{\text{c,G}}$=352 eV for graphene, corresponding to a critical velocity of about $V_{\text{c,G}}$= 9.7 km/s while $K_{\text{c,h-BN}}$=227 eV and $V_{\text{c,h-BN}}$=7.8 km/s for h-BN). Figure 3.3 shows also the comparison between the two different membranes superimposing the top view of DFTB and FEM simulations at the two minimum velocities leading to complete perforation, that is 10 km/s for graphene and 8 km/s for h-BN. The comparison between the radius of the impact crater shows good agreement between the two approaches. Moreover, FEM simulations show how the stresses (von Mises depicted in the figure) are highly localized around the hole within a distance from the impact point lower than three times the molecule radius R. Referring to the estimated damaged volume, the specific critical energies for the perforation of the monolayers are equal to $\bar{K}_{\text{c,G}} = 51.8$ MJ/kg and $\bar{K}_{\text{c,h-BN}} = 45.0$ MJ/kg respectively.

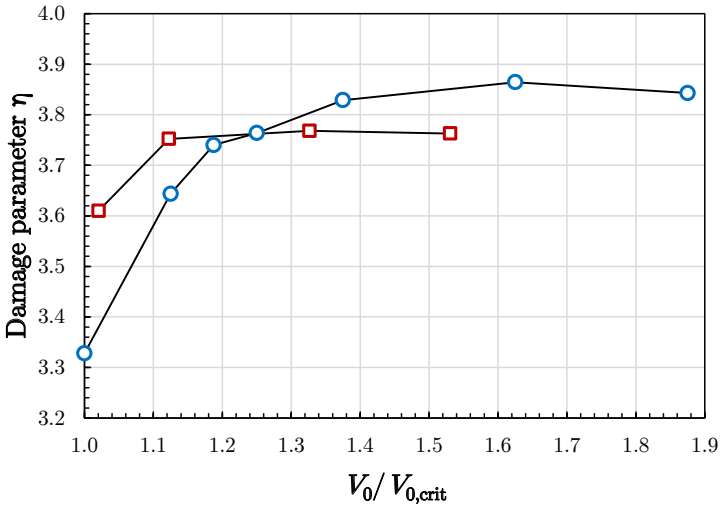

Figure 3.4: Evolution of the damage parameter η for graphene and h-BN monolayers defined as the ratio between the damaged area and the fullerene projected area πR^2 as a function of the fullerene impact velocity V_0 normalized with respect to the corresponding ballistic limit $V_{0,\text{crit}}$, that is the minimum projectile velocity to perforate the membrane.

3.3.2 Ricochet regime

If the impact kinetic energy K_0 is not sufficiently high to perforate the membranes (ricochet regime) the target will dissipate the kinetic energy by undergoing two different deformation mechanisms, that is bending or membrane stretching, in relation to its bending and membrane stiffness, boundary conditions, and the impact kinetic energy of the projectile itself. We consider a configuration at which the instantaneous COM velocity of the projectile is closes to zero, i.e. at the bouncing onset. Part of the energy is converted to vibration (phonons) of the membrane, thus the elastic strain energy of target would be $K_{\text{strain}} = (1-k)K_0$ where k represents the amount of the projectile kinetic energy dissipated by mechanical waves in the membrane plus the one converted into kinetic energy of the target.

To analyse the sub-critical regime, the target is assumed to be made of linear elastic and isotropic material, defined by the Young's modulus E and Poisson's ratio ν. Although the material properties are non-linear at high strain –as used in the FEM models- this simplification is acceptable far from the perforation and failure conditions. We model the system as a circular membrane of radius $L \gg R$ (as for the simulations) and thickness t. The impact is accounted as a normal concentrated force F acting on the target, assuming that all the projectile kinetic energy K_0 is converted into strain energy of the target (i.e., $k = 0$). Considering a finite kinematic mechanism in a membrane regime, the vertical

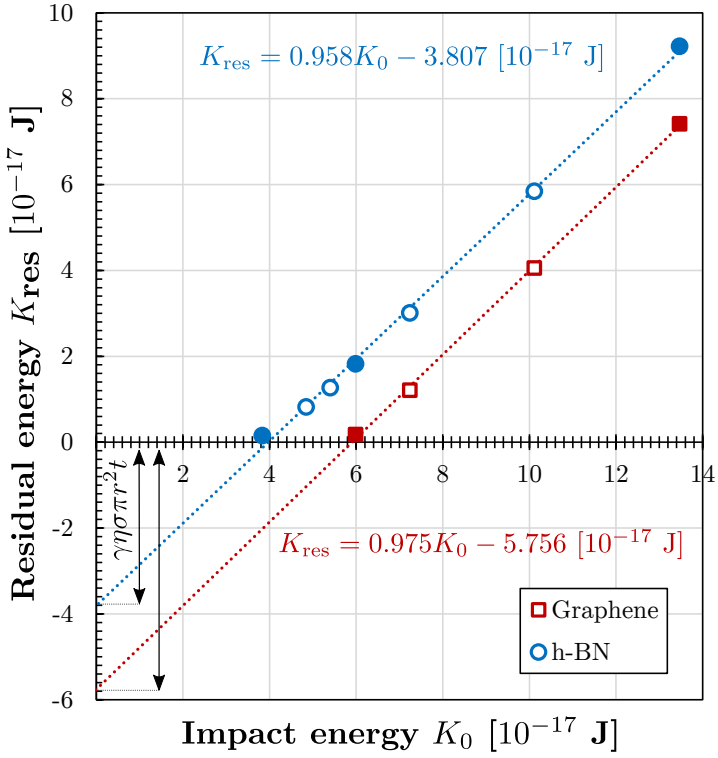

Figure 3.5: Plot of the fullerene residual COM energy K_{res} vs. the initial impact energy K_0 at penetration regime (filled dots correspond to *ab initio* simulations, empty dots to FEM). Assuming an energy dissipation within a material volume defined by the layer thickness $t = 3.35$ Å and the projectile effective imprint area corresponding to the fullerene radius, the membrane impact strength is derived from the intercept of the linear fit (Equation (3.11), $p = 2$). The damage parameter η is the the ratio between the actual damaged area and the projected fullerene area. Atomistic simulation data by Dr. Simone Taioli.

displacement w at the impact point is a function of the force F and it satisfies [119]:

$$\left(\frac{w}{t}\right)^3 = \left[1-\left(\frac{1-3\nu}{4}\right)^{1/3}\right]^3 \frac{4L^2}{(1+\nu)\,\pi E t^4} F; \tag{3.12}$$

It follows that the non-linear relation between the membrane strain energy and the midspan vertical displacement w, under pure stretching regime, for the instant at which the projectile residual velocity is zero, thus all projectile kinetic energy K_0 has been transferred to the target, is:

$$\begin{aligned} K_{\text{stretch}} &= \int_0^w F(w)\mathrm{d}w \\ &= \left[1-\left(\frac{1-3\nu}{4}\right)^{1/3}\right]^{-3} \frac{(1+\nu)\,\pi E t}{16L^2} w^4; \end{aligned} \tag{3.13}$$

thus, under membrane stretching one finds $K \propto w^4$. Note that this result is analogous to the case of a cable subjected to a transversal concentrated force. On the other hand, if bending mechanism prevails the elastic strain energy for a clamped circular plate loaded at the centre is $K_{\text{bend}} = 1/2kw^2$, with $k = 16\pi D/L^2$, $D = Et^3/[12(1-\nu^2)]$. It follows that, under bending, $K \propto w^2$

$$K_{\text{bend}} = \frac{2}{3}\pi \frac{Et^3}{(1-\nu^2)} \left(\frac{w}{L}\right)^2. \tag{3.14}$$

The transition between the two deformation mechanisms takes place around a normalized displacement w^*/L that can be determined by equating the two previous expressions for the absorbed kinetic energy (Equations (3.13),(3.14)):

$$\frac{w^*}{L} = \frac{1}{\lambda}\sqrt{\left[1-\left(\frac{1-3\nu}{4}\right)^{1/3}\right]^3 \frac{32}{3\,(1+\nu)^2\,(1-\nu)}}, \tag{3.15}$$

where $\lambda = L/t$ is the plate slenderness. The impact kinetic energy K^* corresponding to the transition can be finally determined introducing Equation (3.15) either into Equation (3.13) or (3.14):

$$K^* = \left[1-\left(\frac{1-3\nu}{4}\right)^{1/3}\right]^3 \frac{64\pi E t^3}{9\,(1+\nu)\,(1-\nu^2)^2} \frac{1}{\lambda^2}. \tag{3.16}$$

In summary, for $K_0 < K^*$, or $w < w^*$, bending prevails and thus mainly $K \propto w^2$, while for for $K_0 > K^*$ (or $w > w^*$) the plate undergoes prevailing stretching with $K \propto w^4$. The estimated transition displacement for both monolayers is $w^* \approx 0.41\,\text{nm}$ and it is independent of the material elastic modulus. Table 3.3 reports the recorded midspan deflection w at different impact energies for the plates in the ricochet regime. The

Table 3.3: Maximum deflection w at membrane midspan for single layer graphene and h-BN at different initial impact energies K_0 in the ricochet regime. At $K_0 = 239.1\,\text{eV}$ h-BN starts to show damage an thus it is not included in the computations.

Impact energy [eV]	$w_{\mathbf{G}}$ **[nm]**	$w_{\mathbf{h\text{-}BN}}$ **[nm]**
33.6	0.370	0.456
59.8	0.437	0.543
93.4	0.493	0.619
134.5	0.560	0.716
183.1	0.628	0.781
239.1	0.695	perforated

bi-logarithmic plot of Figure 3.6 shows the deflection w as a function of the impact kinetic energy K_0. The estimated scaling exponents of the law $w = K^q$ are $s \approx 0.320$ for graphene and $s \approx 0.322$ for h-BN, and are intermediate between the predictions for stretching ($q = 0.25$) and bending ($q = 0.5$). From the best-fit of the simulation points (Table 3.3) with Equation (3.13) $q = 0.25$ we derive the elastic moduli of the materials, which are $\bar{E}_{\text{G}} \approx 1.93\,\text{TPa}$ and $\bar{E}_{\text{h-BN}} \approx 0.947\,\text{TPa}$. According to the ratio between this theoretical prediction (computed assuming $k = 0$) and the actual values of the mechanical properties [23, 102] we estimate $k_{\text{G}} = 0.48$ and $k_{\text{h-BN}} = 0.69$ for graphene and h-BN membranes respectively. This represents an estimate of the amount of projectile kinetic energy dissipated by mechanical waves. The corresponding transition kinetic energies, which are dependent on the respective elastic moduli, are $K^*_{\text{G}} \approx 27.4\,\text{eV}$ and $K^*_{\text{h-BN}} \approx 13.5\,\text{eV}$, confirming that for the whole analysed cases the plates mainly undergo stretching under impact. From the cases corresponding to the higher impact energy at penetration it is possible to calculate the maximum specific energy stored in the membrane before breaking. Assuming uniform tension, as $K_0/\rho\pi L^2 t$, we obtain $2.11\,\text{MJ/kg}$ and $2.21\,\text{MJ/kg}$ for graphene and h-BN respectively.

3.3.3 Energy scaling in multilayer armours

Recalling the Equation (2.23), which expresses the scaling of energy absorption with the number of layers N, we studied this scaling also for these nanoarmors. DFTB simulations have been performed on 1, 2, 4, and 6 layer homogeneous and hybrid membranes with alternate stacking of graphene and h-BN. The used COM initial impact velocities were equal to 10, 15, 25, and 35 km/s respectively, being slightly higher the ballistic limit of the multilayers. The analysed graphene-based, h-BN and hybrid nano-armours show all high positive values of α (Figure 3.7). However, this synergistic interaction between layers was not observed at the micro- and macro-scale for graphene armours, e.g. in the recent

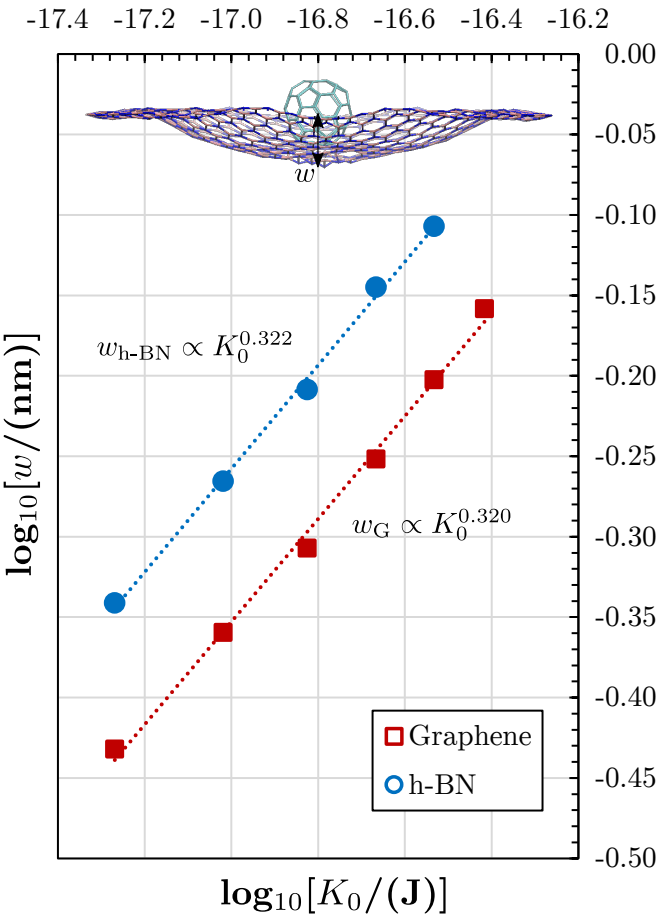

Figure 3.6: Plot of the maximum deflection w at midspan vs. the impact kinetic energy K_0 of the incident particle for graphene and h-BN membranes in the ricochet regime. The obtained scaling $w \propto K^{0.32}$ is in the proximity of the condition derived for the stretching regime $w \propto K^{0.25}$ and intermediate with that of bending $w \propto K^{0.5}$. Atomistic simulation data and images by Dr. Simone Taioli.

experimental work by Lee et al. [12] on micrometric projectile impacts on graphite, in which a sub-optimal scaling law ($\alpha < 0$) was found.

To explain this apparent mismatch we analysed the evolution of the damaged volume, which can be directly correlated to the amount of the absorbed energy. During the perforation of the target the radius of the damaged area is not constant but increases through the the thickness, creating a tapered damaged volume of truncated conical shape (Figure 3.8). The variable size of the radius at the i-th layer can be expressed by the following relation:

$$R_i = \sqrt{\eta}R + \sum_{i=1}^{N} t_i \tan\theta, \tag{3.17}$$

where θ is the inclination angle of the cone apothem and t_i is the thickness of each layer, that is, in our case, 3.415 Å and 3.407 Å for graphene and h-BN, respectively. For a shear-dominated mechanism $\theta \to 45°$ [19]. Assuming all the layers of the same material ($t_i = t$), Equation (3.17) yields to an evolution of the specific damaged volume as follows:

$$\frac{V_{\text{dam}}}{N} = \frac{\pi t^3}{3}\left[3\eta\left(\frac{R}{t}\right)^2 + 3\sqrt{\eta}N\left(\frac{R}{t}\right)\tan\theta + N^2\tan^2\theta\right]. \tag{3.18}$$

For the graphene membrane we determined from DFTB simulations $\theta \approx 13.5°$ (Figure 3.8). The shape of the truncated cone depends on the dimensional ratio R/t between the radius of the impacting mass and the target thickness. However, the damaged area does not indefinitely increase as stated by Equation (3.18) but tends to saturate leading into a cylindrical volume, hence $\frac{V_{\text{dam}}}{N} \propto N^0$ for $N \to \infty$. In order to take into account this, Equation (3.18) is considered valid up to $N < N^* = \text{int}[6R/t]$, where $6R$ is acknowledged in ballistic literature to be a reasonable value of the maximum radius of the damaged cone (see also Methods for the determination of the models supercells). Thus, for $N > N^*$ we assume $R_{\max} = R(N^*) =$const.. Furthermore, accounting for a Linear Elastic Fracture Mechanics (LEFM) scaling law [120] for material strength, one can assess the strength from the following relation:

$$\sigma = \sigma_0^*\left[(N+1)\cdot\left(\frac{R}{t}\right)\right]^{-b}, \tag{3.19}$$

where b is the strength scaling law exponent, here assumed 0.5 according to LEFM, and $\sigma_0^* = \sigma_0\left(\frac{R}{t} = 1\right)$. In particular, according to a Griffith-like scaling law, the dimension of the characteristic defect of the material is assumed proportional both to N, i.e. the plate thickness, and to the area affected by the impact, which is directly proportional to R. The combination of volume and strength size-scalings, which both depend on N and R/t, may yield in some cases -according to the competition between the two- to an optimal configuration as reported in Figure 3.9a. N_{opt} is the number of layer that characterizes the transition between positive and negative scaling, and that maximizes the specific energy absorption of the plate, which can be obtained as follows from Equations (3.18),(3.19):

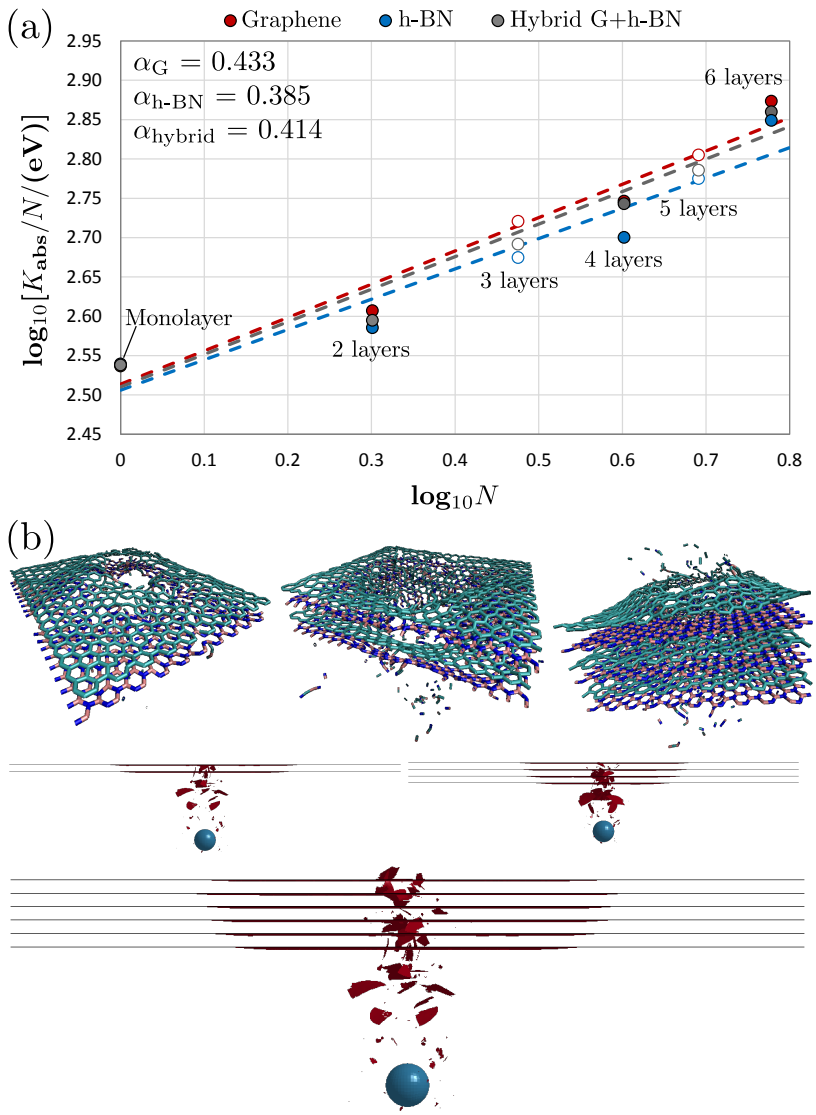

Figure 3.7: (a) Determination of the specific energy absorption scaling exponent α for graphene (red line), h-BN (blue line) and hybrid graphene/h-BN (grey line) alternate armours. Values of α are greater than 0, showing a synergistic interaction as the number of layers increases. The fit for the determination of the scaling exponent is performed by using the DFTB simulations (filled dots) while FEM simulation points (empty) are included for results comparison. This result is far from being trivial since values of $\alpha < 0$ have been found in macroscopic composite armours [11] and graphene upon microscale impact [12]. Impact simulations of the hybrid armour system (2, 4 and 6 layers) from DFTB and FEM simulations are depicted. Atomistic simulation data and images by Dr. Simone Taioli.

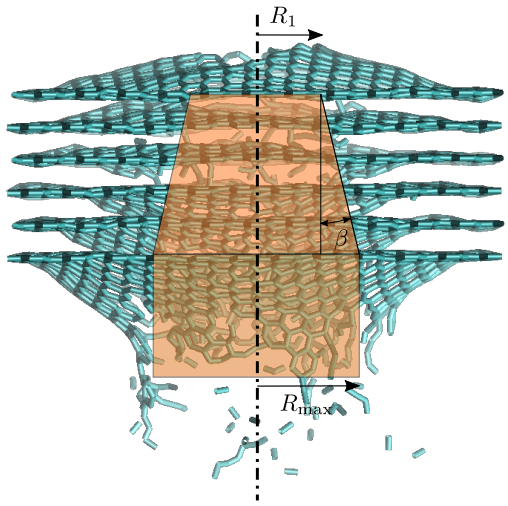

Figure 3.8: Conical shape of the damaged volume observed in DFTB simulations with a measured diffusion angle $\beta \approx 13.5°$. For the 6 graphene armour shown in the figure the top and bottom radius of the damaged cone are respectively $R_1 = 6.65\,\text{Å}$ and $R_{\max} = 7.05\,\text{Å}$.

$$\frac{K_{\text{abs}}(N)}{N} = \sigma_0^* \frac{V_{\text{dam}}(N)}{N} \left[(N+1) \cdot \left(\frac{R}{t} \right) \right]^{-0.5}. \tag{3.20}$$

We notice that the dependence of the damaged volume on material strength is not considered. Figure 3.9b depicts the specific energy absorption versus the number of layers N for different values of R/t. It can be clearly seen that N_{opt} emerges for nanoscale configurations ($R/t < 2$), such as the ones investigated in this work with the fullerene impact ($R/t \approx 1.48$). Our DFTB-FEM simulation results are in good quantitative agreement with the analytical prediction. The optimal number of layer N_{opt} is predicted to be 5 for $R/t = 1$ and 10 for $R/t = 2$, and from the coupled DFTB-FEM data we obtain $N_{\text{opt}} = 7$. Furthermore, values of the absorbed energy at the nanoscale are in good agreement also with molecular dynamics simulations of Haque et al. [13]. For higher scales ($R/t > 2$) the optimum value vanishes and the scaling is negative for any N. For $R/t < 10$ the contribution to positive scaling of the damaged volume is still relatively significant and a change in the slope α of the curves in the bi-logaritmic plane still appears. By increasing the projectile dimension of the projectile, the specific damaged volume tends to be constant and the scaling of the strength is predominant (Figure 3.9b), determining a nearly constant negative α independent of N. Thus, predictions from the same equation are in good agreement also with the trend experimentally observed by Lee et al. [12] in microscopic impact configurations.

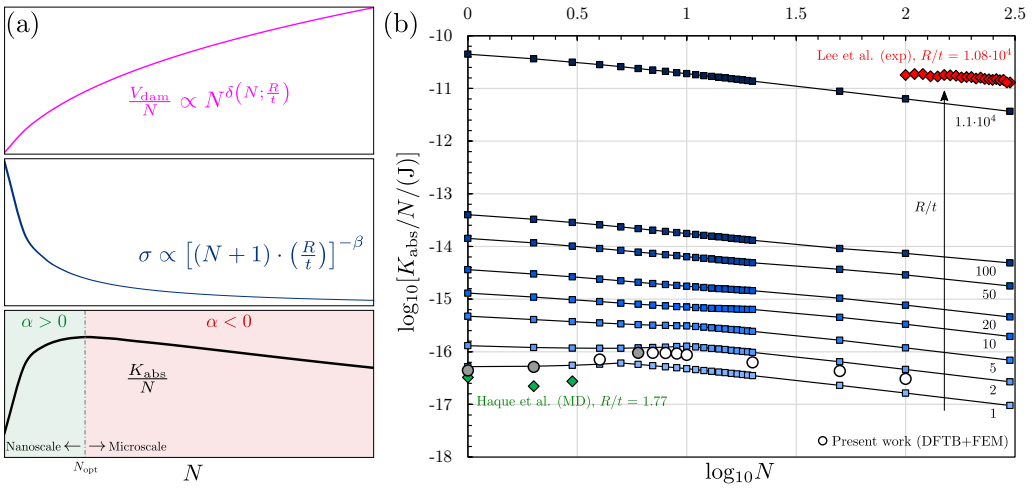

Figure 3.9: Scaling of the specific energy absorption in the multilayer nanoarmours with the dimensional scale. (a) Conceptual representation of the role of the damaged volume scaling (Equation (3.18)) and of the material strength scaling (Equation (3.19)) according to LEFM in determining an optimal number of layer N_{opt}, to which correspond both the maximum specific energy absorption and the inversion in the sign of the scaling exponent α. (b) Results obtained from analytical calculations (Equation (3.20)) for different R/t configurations (curves with square dots, the lines are just a guide to the eye being the function of integers values of N) compared with the results from DFTB and FEM simulations (circular dots), MD results from Haute et al. [13] at the nanoscale, and experimental results from Lee et al. [12] at the microscale.

3.4 Conclusions

In this work we studied the mechanical behaviour of single and multilayer graphene and h-BN armours undergoing hypervelocity impacts of a C_{60} fullerene molecule. Coupling atomistic DFTB and continuum FEM approaches, the ballistic critical penetration energy of single sheets of graphene and h-BN was determined along with the impact strength of these two 2D materials. The membrane behaviour in the subcritical impact (no perforation) was also rationalized via a kinematic model on an elastic equivalent continuum membrane.

Multilayer homogeneous and hybrid structures have been investigated to study the energy absorption scaling laws for different number of layers. We have demonstrated that generally at the microscale the scaling of these nanoarmours is not optimal, confirming that graphite is a weaker configuration also for impact loads. However moving to nanoscale -that is projectile dimension comparable with the thickness of the monolayer, $R/t \to 1$, and few layer armours, $N < 10$- a strong synergistic coupling emerges. This dimensional scaling is rationalized for graphene by taking into account both the damaged volume as well as the material strength scalings, according to the LEFM model. Although more accurate predictions could be obtained by refining the constitutive model, the LEFM approach is able to quantitatively predict the transition between positive and negative scaling at different dimensional scales, finding a good agreement between our simulations and the simulations/experimental data available in the literature [12, 13]. At this scale an optimal number of layers, between 5 and 10, emerges that maximizes also the specific dissipation of energy under impact. These results suggests that multilayer 2D material based armours should be structured and optimized at the nanolevel, not relying on the mere high specific mechanical properties of the constituent materials. These armours, for example, would be particularly effective in providing protection from high energy nanoscopic fragments or even suitable as coating for protection from cavitation erosion.

We believe that these results provide significant guidelines for the design and optimization of graphene and other 2D-materials armours.

Chapter 4

Mechanics of aerographite tetrapods and related networks

In this chapter it is shown an example of possible 3D structuring of graphene and other 1D and 2D materials in the form of hollow tetrapodal networks for obtaining structures with extreme lightness which exhibit a large reversible deformation mechanism governed by local buckling instability. The buckling of the central joint was seen to be the governing mechanism of the overall deformation of the single tetrapod. We then propose a nonlinear mechanical model for describing the formation of the "buckling-hinge" at the tetrapod central joint or along the arms. Through FEM simulations the behaviour of single tetrapods under bending, tension or compression is investigated, elucidated, and compared with *in situ* scanning electron microscopy experiments. The analysis of tetrapods of different size-scales and tube cross-section aspect ratio allowed to generalize behaviour of such kind of structures. The mechanical model of single tetrapods is then used as input for the modelling of aerographite networks under compression. The findings permit to better understand the mechanical response of the networks with different densities and known tetrapod characteristics, allowing their optimization as well. Furthermore, the models can be extended to the design of similar aerogels and scaffolds based on graphene and other 2D materials.

4.1 Introduction

Three dimensional (3D) cellular materials built from carbon nanostructures are currently under increased investigation in terms of fabrication and physical properties because of their significant technological potential for diverse advanced applications, such as biological scaffolds, electrochemical biosensing, supercapacitors, lightweight flexible batteries, and highly efficient oil absorbers [121–126]. Since the introduction of graphene, a large variety of synthesis methods, involving direct growth, wet chemistry, and templates,

have been introduced for the growth of 3D carbon-based nanomaterials [126–131] and the field is still under development. Nanoscale carbon structures can be built, for example, from carbon nanotubes (CNTs) or graphene flakes [132] exhibiting very high surface to volume ratios from which interesting physical and chemical features originate. But to efficiently access their unique nanoscopic features, these materials should be preferentially available in a macroscopic 3D form with a sufficient mechanical robustness and stability so that they can be manufactured into any desired structured shape [133]. Thus, 3D carbon-based networks comprising both sufficient mechanical strength and very high porosity are desirable, but this is a challenging task in 3D cellular networks. For instance, it is well known, that 3D networks based on CNTs being randomly interconnected and held in place only by vdW forces are prone to failure when compressed and several attempts have been made to overcome this drawback [134, 135]. In this context, the morphology and interconnections of the nanoscale carbon-based network building units play a fundamental role.

As basic building block of porous 3D networks, the tetrapod geometry is an interesting shape, since when accumulated together their spatially extended arms can prohibit close packing very efficiently. Recently, a new concept for producing tetrapod-based 3D networks has been introduced by the flame transport synthesis of zinc oxide [136–138]. During the re-heating at high temperatures the nano- and micro-scale tetrapod arms build interconnections, forming a bridging 3D network which provides necessary mechanical strength and simultaneously very high porosity (up to 98% just by controlling the initial tetrapod template amount in the scaffold) [136, 139]. In the context of carbon-based networks, the ZnO also can be exploited as sacrificial template for the growth of ultra-lightweight and highly porous (porosity > 99.99%) 3D multilayer aerographite (AG) networks (also known in the literature as aerographene). In a single step chemical vapor deposition (CVD) process it is possible to form hollow nano- and micro-tubular multilayer graphene structures, which adopt basic features of the shape of the ZnO templates. The high temperature, together with the presence of a carbon source and of hydrogen (carbon by precursor and hydrogen by gas) allow the deposition of nm-thick graphene flakes on ZnO [140]. Then ZnO is chemically reduced to metallic Zn, whereas Zn evaporates and is removed by the carrier gas (Ar). By modifying the CVD parameters several variants can be synthesized, which differ in walls morphology (closed or open) and/or inner graphitic fillings [140]. Some further AG variants do not have closed graphene-based shells, but just consist of narrow carbon filaments on the former tetrapod surfaces and thus possess an extreme high level (>99.99%) of porosity [140]. This kind of hierarchical networks containing carbon filaments is even more attractive in terms of porosity and was used to realize flexible and semiconducting composites which could be exploited as next generation materials for electronic, photonic, and sensors applications [133, 141].

Apart from being highly porous and extremely lightweight, aerographite exhibits very interesting specific mechanical properties such as remarkable specific tensile strength

(σ/ρ) and Young's moduli (E/ρ) [140], being in principle ideal candidates for impact protection and shock absorption. Some variants show also self-stiffening in cyclic mechanical loading [140]. In order to use AG for different applications, and thus predict the overall mechanical properties of its 3D networks, a detailed understanding of the mechanical behaviour of its individual building blocks is necessary. So far, even nanoscale hollow carbon tetrapods synthesized using ZnO tetrapods templates have been studied with respect to their different properties but their constitutive response has not been discussed yet.

The morphology of the studied aerographite is shown in Figure 4.1a [142] the conversion principle of tetrapodal ZnO (t-ZnO) into hollow and tubular tetrapodal aerographite (t-AG) during the CVD process is schematically illustrated. Furthermore, the panel displays representative SEM images of a typical ZnO tetrapod (Figure 4.1b) and an AG tetrapod (Figure 4.1c), respectively before and after the CVD conversion within the network. The ZnO tetrapod template used in this study, and thus the resulting graphene counterpart, has four arms which are interconnected together with a mutual dihedral angle of $\approx 106^\circ$ via a central joint, resulting in a 3D spatial shape [140]. Thus, their geometry can be defined, in a good approximation, from the vertexes and the centroid of a regular tetrahedron. In the variant used here, the ZnO tetrapods exhibit uniform hexagonal cylindrical arms narrowing towards their tips (see SEM image in Figure 4.1a). The arms typically have a diameter of about $1 \div 5\,\mu m$ at their joint and tip respectively. Arm length is in the range of $15 \div 30\,\mu m$. The morphology of the t-AG arms is strongly influenced by the growth parameters during the CVD process and, if required, t-AG variants with hollow tubular arms, a closed shell, and low aspect ratios can be grown [140]. The arms of the aerographite tetrapods used for the *in situ* atomic force microscopy (AFM) bending experiments exhibit a hollow tubular morphology with diameters being equally in the range of $1 \div 5\,\mu m$ and wall overall thicknesses of the graphene flakes of about 15 nm [142]. The aerographite variant which was used here, possesses tubular and smooth walls (see t-AG SEM images in 4.1c-e). Other crumpled variants may arise from a thickness-dependent growth processes which could be influenced by several parameters, such as surface energies, defects and internal mechanical stresses during the conversion process in the CVD chamber [142].

4.2 Finite element models

FEM models of the tetrapods (results reported in Figures 4.2-4.6 were built associating the arms extremities and the central joint of the tetrapods to the vertexes and centroid of a regular tetrahedron, respectively. The tube walls were modelled with thin shell elements with selective-reduced integration [61], while the spurious modes effects were properly controlled. For the bending experimental setup three arms were fully clamped at the end accounting for the adhesion to the substrate, while both fixed and sliding boundary

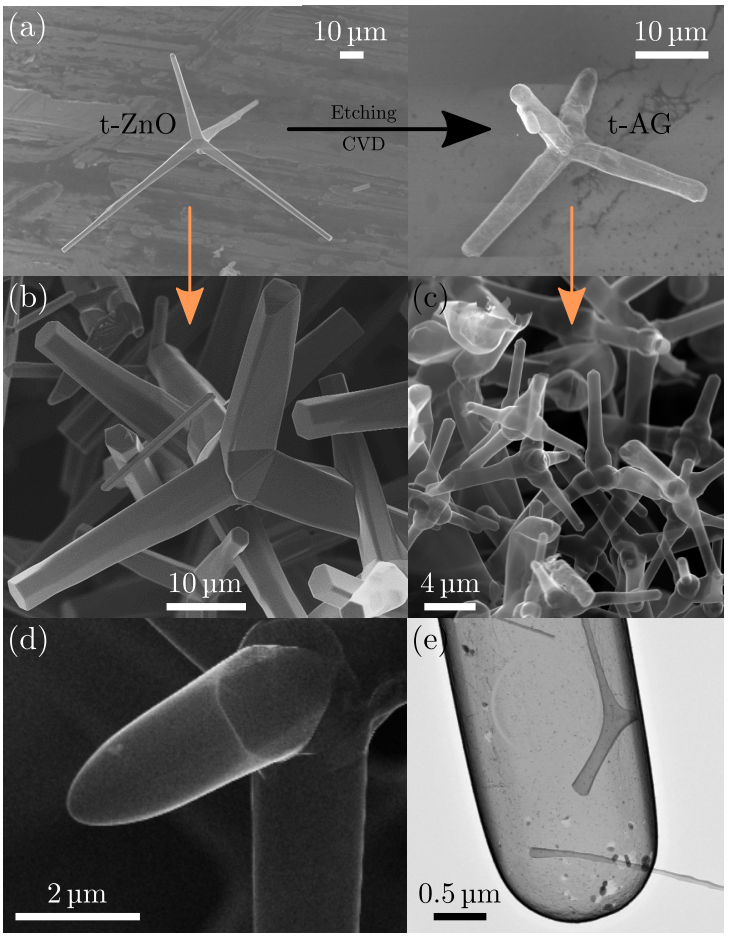

Figure 4.1: Production of AG tetrapods. (a) Schematic illustration of the formation of t-AG from sacrificial tetrapodal ZnO (t-ZnO) in the CVD process. (b,c) Typical high-resolution SEM images corresponding to t-ZnO (left) and converted t-AG networks (right), respectively. (d) Further high resolution SEM image from the tip and middle of a t-AG arm. (e) TEM bright field image of an AG tube with closed walls. Sample fabrication and images courtesy of Institute of Chemical Physics - University of Latvia, Functional Nanomaterials - Institute for Materials Science - Kiel University, and Institute for Polymers and Composites - Hamburg University of Technology.

conditions were considered for both compression and tensile tests. The constraint is applied to a set of nodes rather than a single point, in order to avoid undesired stress localization and large concentrated deformation and to properly account for moments at the clamped restrains. The arm deflection simulating the AFM load is obtained imposing the displacement at the end of the arm, in order also to maximize and quantify the contribution of the arm bending stiffness with respect to the one of the rotational stiffness of the tetrapod central joint. In compression and tension tests the displacement is imposed at the ideal intersection node of the arms axes (tetrahedron centroid). The total applied force, and the bending moment at the joint are computed from resultant at the restrained node with the substrate. Self-contact is implemented in order to avoid walls interpenetration at the buckling/folding sites due to large displacements and properly evaluate the post-buckling contribution. The self-contact is in the form of the vdW interaction presented in the previous chapter. The model for the single arm buckling (second type of *in situ* experiment) follows the same procedure, with the arm modelled as a clamped cantilever at one of the ends and subjected to a transversal imposed displacement at the tip simulating the action of the gold manipulator. The critical buckling point (M_{bh}, α_{bh}) is determined for each case looking at the evolution of the tetrapod deformation energy U, in particular it corresponds to the drop in the local derivative of the $U-\alpha$ curve [143].

4.3 Results

4.3.1 Tetrapod bending experiments

During the first type of *in situ* experiment a tetrapod arm was bent inside a SEM with a soft AFM cantilever while the other three arms were attached to a substrate, following a well-established procedure [144–146]. It was repeatedly observed via instant video recording [142], that the free standing aerographite tetrapod arms tend to preferentially rotate around the central joints and to experience there localized elastic instability, while the arm itself behaves very rigidly. Thus the tetrapod joint appears to be the most compliant location of the arm, as demonstrated later. In general, when a tube starts to buckle its stiffness is significantly lowered [147]. To examine and quantify this stiffness reducing effect of the buckling hinge, the free-standing aerographite tetrapod arm depicted in Figure 4.2a,b was deflected to an angle $\alpha = 0.6$ rad with the help of the aforementioned AFM-cantilever tip from the right towards left side of the image, parallel to the surface. The angle increment $\Delta\alpha$ at the buckling joint is a function of the resulting moment and of the joint rotational stiffness D, thus $\Delta\alpha = \frac{1}{D}|\vec{r}\times\vec{F}| = \frac{M}{D}$ where F is the external applied force on one of the arms and r its lever arm with respect to the computing point (inset in e 4.2c). Being in the elastic regime, we assume D as constant until the applied moment $M = |\vec{r}||\vec{F}|\sin\theta$ is lower than the buckling threshold which is a function of the joint/cross-section geometry and material elastic properties. The resulting nonlinear moment-rotation curve experimentally measured is shown in Figure 4.2c. As expected, it

reveals progressively decreasing rotational arm stiffness for higher deflection angles.

We propose a nonlinear equation for describing the formation of a buckling hinge in the tetrapod central joint or along the arm length analogously to the moment-rotation curve observed during the formation of a plastic hinge in bent beams. In both cases (buckling and yielding) the involved sections at large load possess very low rotational stiffness: a large local deformation arises with small increment of load and the local curvature χ goes to infinite (the radius of curvature $1/\chi \to 0$). Considering a homogeneous linear elastic perfectly plastic isotropic material, an initial linear regime occurs. Then, if the section is sufficiently thick and the material ductile, localized plastic deformation starts with the formation of the so called plastic hinge [148]. On the contrary, if the section is very thin, as in the case of tubular sections, the local elastic buckling may forego yielding or fracture. When $M > M_{\text{bh}}$ the following nonlinear buckling-hinge equation enters into play, which in the most general expression can be expressed substituting plastic characteristic thresholds with the buckling counterparts:

$$M = M_{\text{u}} - M_{\text{bh}}\gamma\left(\frac{\alpha_{\text{bh}}}{\alpha}\right)^{\delta}, \tag{4.1}$$

where α_{bh} is the joint (hinge) rotation at the buckling onset, M_{u} is the ultimate asymptotic moment that the hinge is able to carry, $\delta > 0$ and $\gamma = \frac{M_{\text{u}} - M_{\text{u}}}{M_{\text{bh}}}$ for the continuity of the function at the buckling onset, that is $M(\alpha = \alpha_{\text{bh}}) \equiv M_{\text{bh}}$. We can then compute the evolution of the joint stiffness in the nonlinear regime as derivative of the $M - \alpha$ relationship. It follows:

$$D(\alpha) = \frac{dM}{d\alpha} = \delta\gamma M_{\text{bh}}\alpha_{\text{bh}}^{\delta}\alpha^{-(\delta+1)}. \tag{4.2}$$

Note that $\lim_{\alpha\to\infty} D(\alpha) \equiv 0$ and that to guarantee the continuity of the curve slope $D(\alpha)$ at the buckling onset ($\alpha = \alpha_{\text{bh}}$) it must hold $\delta\gamma = 1$. We come then to the following final formulation of the nonlinear buckling-hinge law:.

$$\frac{M}{M_{\text{bh}}} = (1+\gamma) - \gamma\left(\frac{\alpha_{\text{bh}}}{\alpha}\right)^{\frac{1}{\gamma}}. \tag{4.3}$$

When $\gamma = 1/2$ this equation describes the plastic behaviour of a filled rectangular cross-section. The analogy holds just in the monotonic loading regime: in fact the buckling hinge can be completely reversible. Eventually, different values of γ could be estimated for different cross-section and different causes of joint rotation.

We then simulated the *in situ* experiment presented in Figure 4.2a in which the geometry of the tetrapod was highly regular and clearly visible from the SEM, being its bending not covered by the AFM cantilever. The length of each arm was derived from the *in situ* SEM videos and found to be $\approx 27\,\mu\text{m}$ [142] (Figure 4.2b). This value was set as the distance from the base of the tetrapod arm (thus not the central joint) and the top face of the circular tapered cone defining the arm end (Figure 4.2). The diameters of the cone at the

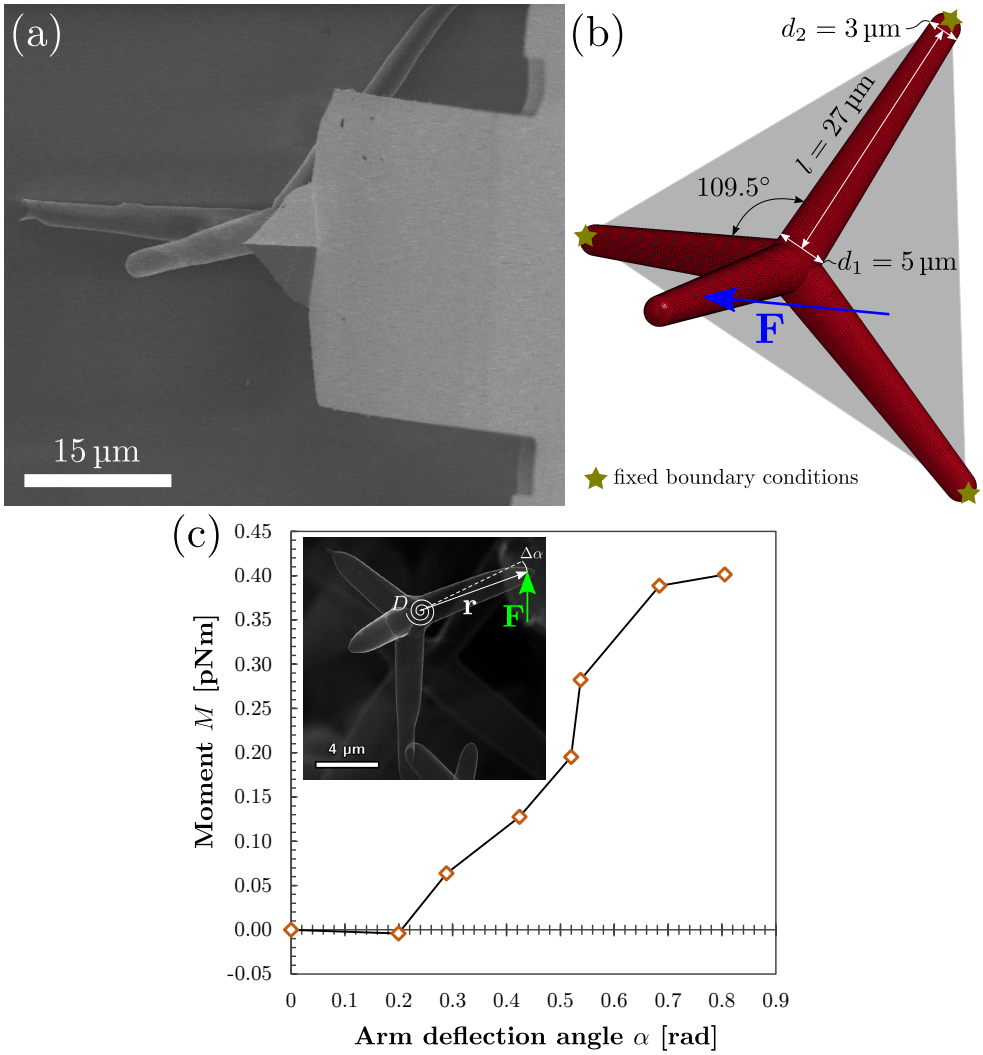

Figure 4.2: Bending experiment on individual tetrapod attached to silica substrate. (a) SEM image of the tested tetrapod under bending action of an AFM cantilever. As the cantilever is moved from right to left parallel to the substrate, both the arm of the tetrapod and the cantilever are bent. (b) FEM model with detail of the geometry of the tetrapod reported in (a); the tetrapod is assumed with extreme points corresponding to the vertexes of a regular tetrahedron. (c) From the AFM acquired raw data (applied force and cantilever deflection as schematically depicted in the inset picture) the current applied moment M and corresponding arm rotation angle α are determined. Sample fabrication, AFM experiments, and images courtesy of Institute of Chemical Physics - University of Latvia, Functional Nanomaterials - Institute for Materials Science - Kiel University, and Institute for Polymers and Composites - Hamburg University of Technology.

tetrapod central joint and at the arm end are respectively $d_1 = 5\,\mu m$ and $d_2 = 3\,\mu m$ and each tetrapod arm is capped at the end with a hemispherical shell of diameter d_2 (Figure 4.2b). We assumed a wall thickness $t = 15.3\,\mu m$, namely corresponding to 45 graphene layers, as suggested from an energy filtered TEM image taken from a representative tetrapod arm [142]. Figure 4.3 shows the normalized moment-rotation-curves of the analysed tetrapod, comparing the experimental results with the curves defined by the nonlinear buckling-hinge model and FEM simulation. The analytical curve is obtained from the best-fit of the experimental data (corresponding to the ones reported in Figure 4.2), while the FEM simulations are calibrated assuming fixed DOFs, the buckling point (M_{bh},α_{bh}) and the ultimate hinge moment M_u. From the buckling-hinge model we estimated $\gamma = 0.44$, and $D = 0.85\,pNm/rad$ in the elastic regime ($\alpha \leq \alpha_{bh}$), while from FEM simulation we determined as best-fit of the AFM experiment a Young's modulus for single the graphene layer of $E = 270\,GPa$ [149, 150] which was not known a priori. Notice that for a thin circular elastic-plastic section undergoing yielding would be $\gamma \approx 0.27$. FEM images of the tetrapod deformation at three different stages are depicted as inset in Figure 4.3 displaying stress distribution within the tetrapods. These FEM pictures confirm that, prior to buckling, the response is governed by a transverse deformation of the adjacent arms nearby the joint and that in the end it merges in the central joint buckling (see FEM third stage image of Figure 4.3b) and that bending deformation of the loaded arm has a negligible contribution. This can also be theoretically claimed approximating the arm as a bent cantilever of length l under a concentrated force at the free end: indeed, assuming by absurd that the arm tip displacement $u = l \cdot \tan\alpha \approx l \cdot \alpha$ is due to the elastic bending of the arm, the materials Young's modulus can be derived as $E = lD/(3J)$, where J is the average cross section moment of inertia of the tapered arm. The corresponding calculated value would be for our case $E = 20\,MPa$, which is very low referring to nominal properties of multi-layer graphene [151]. Consequently, for our thin-walled tube tetrapods, the pure elastic arm bending is negligible when compared to the most compliant buckling-hinge section, either is represented by the central joint or by an intermediate arm section.

4.3.2 Buckling of single arm under bending

In a second type of *in situ* experiment the AG arm was isolated from the tetrapodal structure and thus from the central joint and was instead placed in between two gold tips. In this way, without the AFM cantilever tip masking the buckling location, a better visual evaluation of the hinge formation was realized by constructing a deformation situation in which it was more probable to observe buckling at the most compliant position along the arm length. Figure 4.4 shows a series of SEM micrographs from the buckling of a single tube of aerographite bent in between the two gold tips, from the undeformed state (Figure 4.4a) to a state in which the tube has started to buckle (position indicated by the circle in Figure 4.5b), to a heavily buckled state in which the stiffness of the tube is dramatically decreased due to buckling (Figure 4.4c). This confirms that buckling can

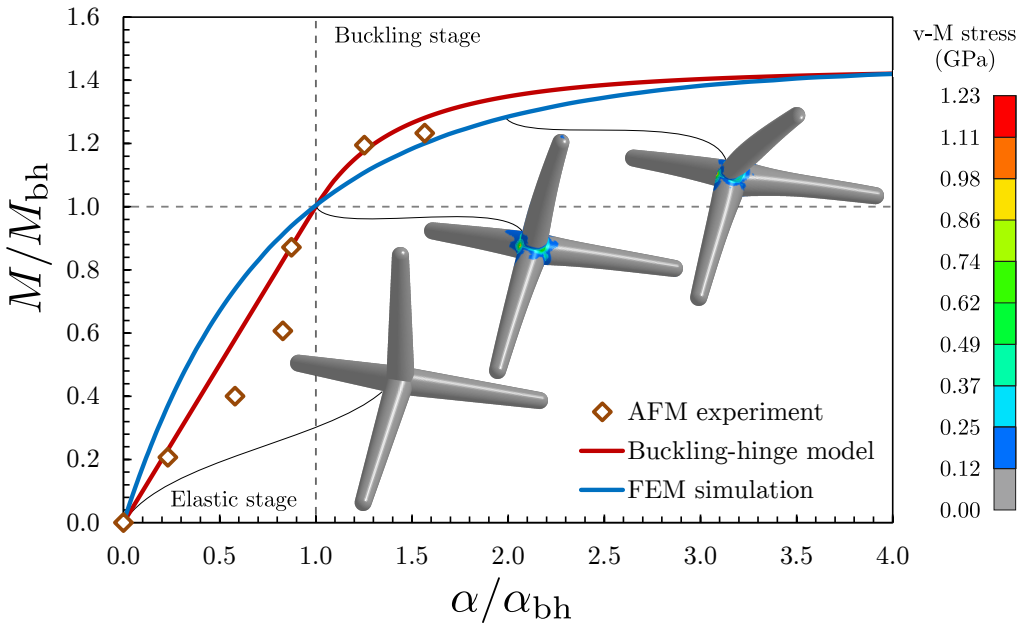

Figure 4.3: Normalized moment-rotation curve for bending of the tested single tetrapod. Experimental results (dots), buckling-hinge model fitted on experimental data (red line) and FEM simulation (blue line) are reported. Contour plots of the von-Mises stress in the tetrapod outer layer of the wall is plotted (scale bar in GPa) showing the stress concentration at the central joint.

occur even on the arm provided that the joint rotational stiffness is sufficiently high (here the joint is not present and the left-hand side extremity can be assumed fully clamped, thus analogous to a rigid joint). Interestingly, the tube recovered elastically to its original shape without any visible damage after flexure folding (Figure 4.4d). This property has already been reported by Falvo et al. [152] for multiwalled carbon nanotubes (MWCNT), but in contrast to these carbon nanotubes the diameter of the examined aerographite tubes is about three orders of magnitude bigger. However, these results indicate similarities between the elastic buckling of aerographite tubes and MWCNTs. The buckling-hinge model is likewise applicable to this case. We assumed that the buckled section takes an elliptic shape, this can be computed by imposing two conditions: (1) the perimeter of the tube section must keep constant under ovalization and (2) the cross-section moment of inertia is related step by step to the current value of the joint rotational stiffness $D(\alpha)$. These conditions are expressed by the following relations, that must hold for each arm bending angle:

$$\begin{cases} \pi d = \pi\sqrt{2(a^2+b^2)} \\ D(\alpha) \approx \frac{EJ}{b} \end{cases} \tag{4.4}$$

where d is the diameter of the tube before buckling in the section where the hinge forms. The system of the two previous equations can be solved numerically state by state providing the evolution of the cross sectional shape after buckling (Figure 4.4e). The result at buckling onset is analogous to the one that can be derived by different method presented elsewhere [147]. Figure 4.4e shows the curve obtained from FEM simulation and the fit obtained with the buckling-hinge model ($E = 270\,\text{GPa}$, $d_1 = 0.5\,\mu\text{m}$, $d_2 = 0.75\,\mu\text{m}$, $t = 15.3\,\text{nm}$, $l = 2.6\,\mu\text{m}$). The buckling-hinge model validity is also confirmed by the good agreement between the simulation observed cross-section shape at the buckling hinge and its analytically derived counterpart (Figure 4.4e).

4.3.3 Scaling laws

The obtained results can be generalized to tetrapods of different size-scale and shape, namely aspect ratio t/d. Indeed, it is acknowledged that for thin-walled tubes, such as ours, the critical compressive local strain ε_{bh}, corresponding to the buckling condition under bending, is given by the following relation [143, 153]:

$$\varepsilon_{\text{bh}} = \eta \frac{2}{\sqrt{3\,(1-\nu^2)}} \frac{t}{d} = \eta\,\kappa \frac{t}{d}, \tag{4.5}$$

where, in our case, $\kappa \approx 1.178$ assuming a Poisson's ratio $\nu = 0.2$ for the graphite tube walls and η is an adimensional factor theoretically equal to 1. Figure 4.5a shows the simulations results in terms of critical buckling stress σ_{bh} for tetrapods of different scales $\zeta = d/d_0 = l/l_0$ both for constant and variable aspect ratios t/d. These are compared

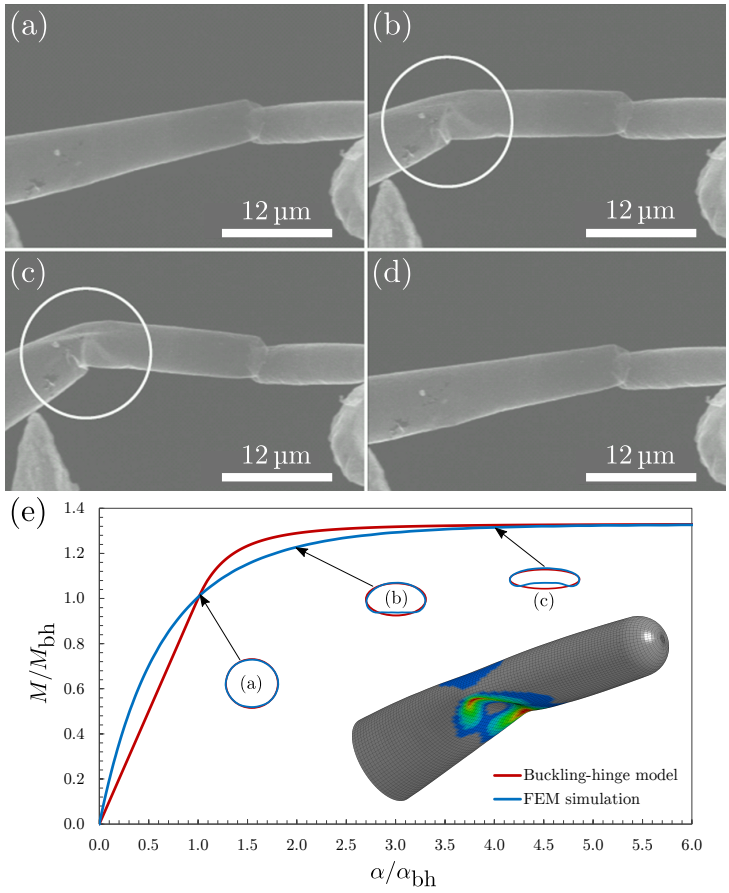

Figure 4.4: Reversible buckling of a bent AG tubular arm. (a) Tube in the undeformed state; (b) the tube has started to buckle (position indicated by the circle); (c) tube heavily buckled with its stiffness dramatically decreased; (d) the tube recovered elastically its original shape. (e) FEM simulation derived curve (blue) and the analytical one (red) determined from the buckling-hinge model are reported. The shape of the buckling hinge cross section at different stages from simulation and its prediction from analytical calculations are depicted. The estimated buckling-hinge parameter is $\gamma = 0.33$, note that the corresponding value determined for buckling at the tetrapod central joint was $\gamma = 0.44$. Sample fabrication, AFM experiments, and images courtesy of Institute of Chemical Physics - University of Latvia, Functional Nanomaterials - Institute for Materials Science - Kiel University and Institute for Polymers and Composites - Hamburg University of Technology.

to the analytical predictions of Equation (4.5), according to $\sigma_{\mathrm{bh}} = E\varepsilon_{\mathrm{bh}}$, from where a very good agreement is observed, considering $\eta \approx 0.787$ as derived from the best fit of numerical simulations. Buckling stresses of the order of the gigapascal emerge. The small difference of this factor from the theoretical unit value, which corresponds to the case of simple tubular section [143, 153] can be imputed to the higher complexity of the buckling deformation mechanism at the central joint, which involves also multiple layers constituting the tube wall. Figure 4.5b shows the dimensionless moment vs. rotation curves for all the analysed cases compared with the analytical prediction obtained inserting $M_{\mathrm{bh}} = \frac{2\sigma_{\mathrm{bh}}J}{d}$ into Equation (4.3), with $\gamma = 0.44$. The collapse of all the curves into a single master curve confirms the validity of this last scaling-shape law. It could also be used to include statistical variation in the tetrapods geometry for the modelling of realistic networks.

4.3.4 Compressive and tensile bahaviour of tetrapods

With FEM simulations we performed further mechanical characterizations on the same tetrapod geometry under pure compression or tension, with fixed or sliding boundary conditions in order to simulate the limit cases of perfect bonding and weak interaction between adjacent tetrapods. We subjected the central joint of the tetrapod to an imposed displacement orthogonal to the substrate. The results are reported in Figure 4.6. Figure 4.6a depicts the compression behaviour: the buckling-hinge local instability leads to a global snap-through instability. For sliding boundary conditions the buckling-hinge appears at the central joint while for fixed boundary conditions early buckling-hinges appear on each arm near the clamps (deformation level ②), being there also a bending moment. At larger joint displacement the central buckling-hinge occurs (level ②) while the arm hinges disappear. After the snap-through the three base arms are under tension and a further increase in the force is observed (level ③). Regarding the tensile behaviour depicted in Figure 4.6b, the fixed boundary conditions are able to prevent buckling and the tetrapod behaviour is governed by the the elastic bending of the arms attached to the substrate, thus resulting in much higher overall stiffness and bearing capacity with respect to the sliding boundary conditions. In the latter, the formation of the buckling hinge at the central joint is observed, representing an example of buckling in tension [154]; at very large displacements the tetrapod starts to stiffen, being governed by the arms axial rather than bending stiffness. The slope of the force-displacement curve is nearly the same in both tension and compression as expected, and depicted in the Figure 4.7. The four in-silico tests , which could be considered as limiting cases of real scenarios where mixed boundary conditions are expected (compliant clamps), are all in agreement with the buckling-hinge model prediction, as demonstrated in the Figure 4.8, confirming the generality of the proposed approach.

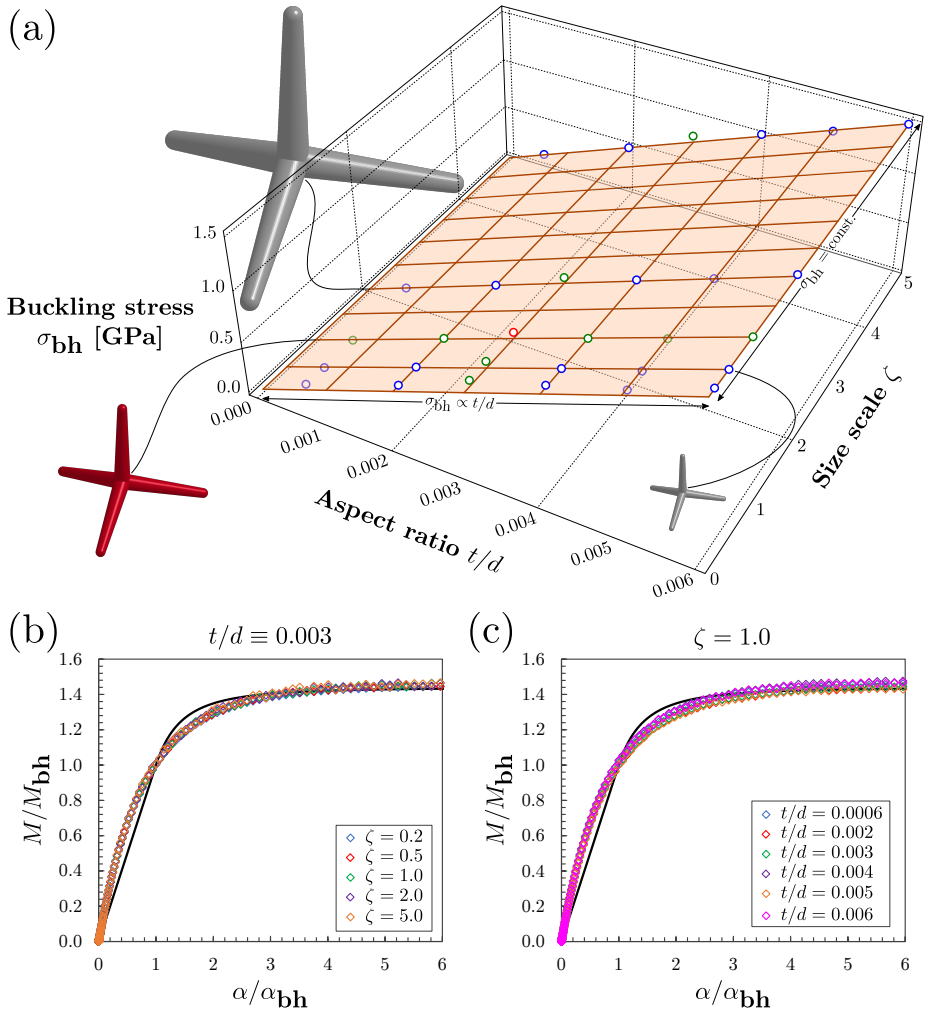

Figure 4.5: Scaling of the joint mechanical properties for different tetrapod size scales ($d/d_0 = l/l_0$) and tube aspect ratios (t/d). (a) Maximum buckling stress $\sigma_{bh} = E\varepsilon_{bh}$ at the joint section from numerical simulations (dots) compared with the best-fit surface of Equation (4.5). It emerges nearly independence of the buckling stress/strain from the size scale (t/d = const.) and linear dependence with respect to the aspect ratio t/d. The red dot represents the nominal tested tetrapod of Figure 4.3 (ζ=1, t/d=0.003) while the green dots correspond to its size scaling with t/d=const.=0.003, or to the aspect ratio scaling only (ζ=1). Tetrapod at three different size scales (ζ=0.2, 1.0, 2.0) are depicted. (b) Dimensionless moment-rotation curves of the 5 performed simulations with t/d=const.=0.003 compared to the analytical prediction of the buckling-hinge model (continuous line). (c) Dimensionless moment-rotation curves of the 6 performed simulations with ζ=1 compared to the analytical prediction of the buckling-hinge model (continuous line).

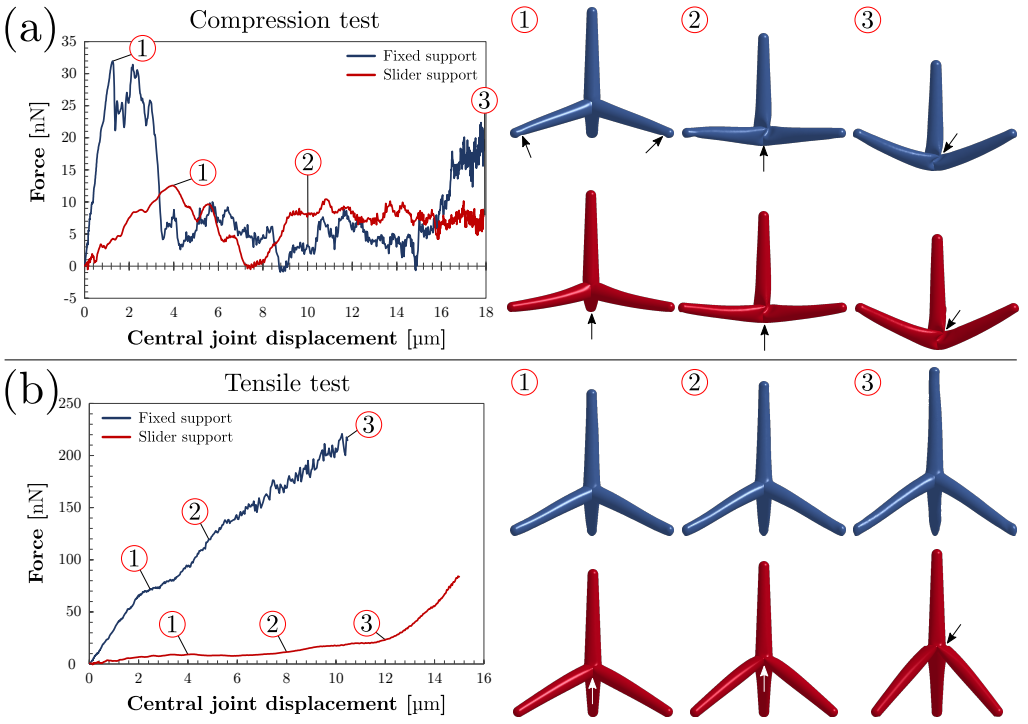

Figure 4.6: Force–displacement curves of a single tetrapod under compression or tension and fixed or sliding boundary conditions as computed by FEM simulations. The boundary configuration in the FEM images is identified by the tetrapod colour according to the graph legend. The locations of the buckling hinge formations are highlighted with the arrows. (a) Compression tests showing a typical snap-through-like global instability under displacement control. The reactive moments at the clamps yield there to the formation of buckling-hinges ① which disappear for large displacement leading to the formation of a central hinge ②. The sliding boundary conditions led the formation of the hinge only at the central joint where the maximum moment takes place. (b) Tension test showing how the fixed boundary conditions do not allow the formation of a buckling hinge thus, the tetrapod behaviour is governed by arm bending. In the sliding boundary conditions case, stiffening after displacement level ③ is due to the base arms alignment along the loading direction after the formation of the central hinge.

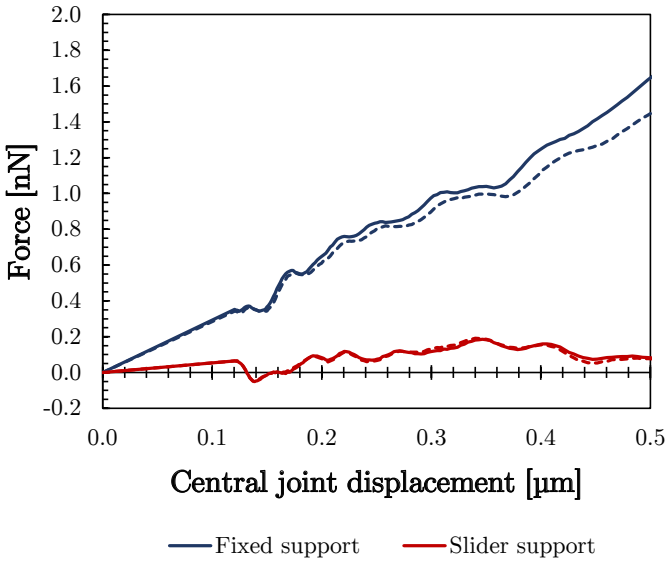

Figure 4.7: Magnifications at small displacements of the force-displacement curves reported in Figure 4.6 of tetrapods under compression or tension and fixed or sliding boundary conditions ($\varepsilon = \Delta h/h_0 \leq 1.3\%$ where $h_0 = 37.5\,\mu m$ is the initial total height of the tested tetrapod). Compression and tensile behaviour (dashed and continuous lines respectively) are compared for the two different boundary conditions, confirming that prior to the nonlinear regime (buckling) the tetrapod stiffness is the same in tension and compression.

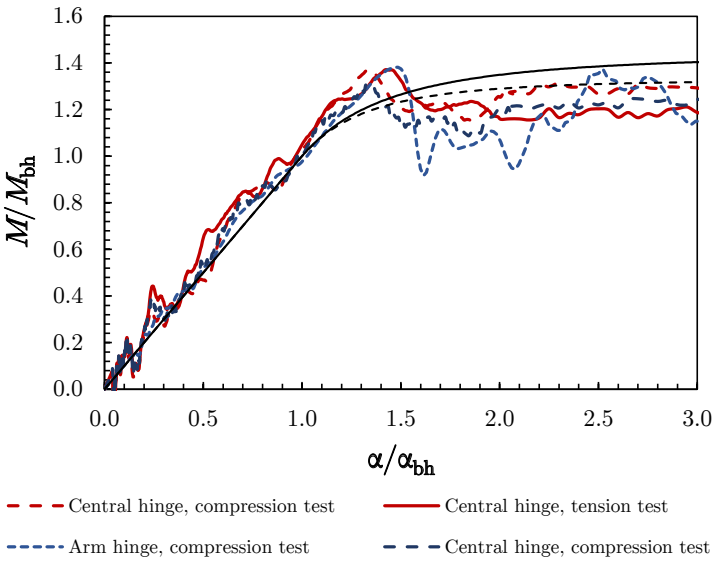

Figure 4.8: Dimensionless moment-rotation curves for the buckling hinges formation in the tetrapod. Buckling hinges appear in the central joint and/or close to the arms near the clamps. Compression or tension tests and sliding or fixed boundary conditions are considered. Red curves correspond to tension or compression tests with sliding boundary conditions; the blue lines refer to the two hinges appearing in the compression test with fixed boundary conditions (Figure 4.6a). No hinge formation is observed for tensile test with fixed boundary conditions (Figure 4.6b). The constitutive behaviour of all the buckling hinges is well described by the model prediction. The black lines represent the fit of the buckling hinge model (Equation (4.3)) to the AFM tetrapod bending experiments (continuous line is related to the experiments reported in Figure 4.3, $\gamma = 0.44$, whereas dashed line is related to the experiments reported in Figure 4.4, $\gamma = 0.33$). Thus, these results -related to different loading and boundary conditions- confirm the generality of the proposed model without invoking any best fitting parameters.

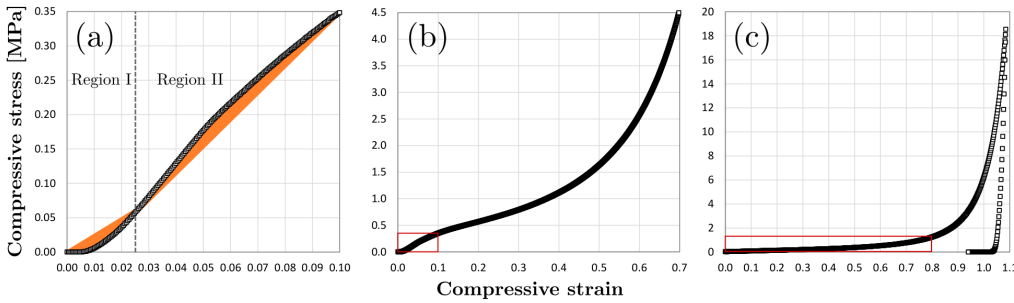

Figure 4.9: (a) and (b): An aerographite network with a density of 3.84 mg/cm^3 density was compressed by 70%, down to 30% of its original height. In (a) a magnified view the values up to 10% compression are shown and the first two of the three deformation regions I and II can be distinguished. The complete curve for the sample is depicted in (b) and illustrates the onset of the densification region (III) at about 30 %. (c) Ultimate compression test of an aerographite sample with a density of 2.86 mg/cm^3 showing a rapid increase of the compression stress in the densification region III starting at about 60 % deformation. Experiments courtesy of Institute of Chemical Physics - University of Latvia, Functional Nanomaterials - Institute for Materials Science - Kiel University and Institute for Polymers and Composites - Hamburg University of Technology.

4.3.5 Tetrapodal aerographite networks

Figure 4.9 shows a compression test of an aerographite sample with a density of 3.84 mg/cm^3 up to 70 % deformation. The stress response of the sample can be divided into 3 different regions which are separated by two points of inflection (delimited by the dashed lines). This means the curvature of the stress curve changes twice during the compression. This behaviour is typical for elastomeric open cell foams. In the first region up to $\approx$ 3 % deformation (see Figure 4.9a) the linear-elastic rotation of individual tetrapod arms around their junction. Here, however, no linear behaviour is observed in this region. Instead the stress increases progressively. This can be explained in terms of the surface roughness of the sample and by nonlinear behaviour at the contact points between tetrapods. At first, higher stresses act at exposed tetrapod structures until they collapse and then neighbouring tetrapods approach the mechanical contact. Thus the number of contact points between the surface of the sample and the mechanical contact area of the setup and the stress on the bulk increases progressively.

In region two, between 3% and 30% deformation (Figure 4.9a), the slope gets smaller indicating the onset of different mechanisms in the network. There are two major contributions: first, reversible buckling of the tetrapod arms occurs involving decreased decreased post-buckling. Secondly, agglomeration can occur, since it was also investigated in earlier *in situ* experiments that individual tetrapods adhere easily to each other by vdW forces.

With further compression, starting from 30% deformation in (Figure 4.9b), the curvature changes again and the stress increases progressively in the third region to a maximum value of 4.8 kPa for 70% compression. The integral over the stress strain curve from 0 to 70% compression gives a specific energy of $0.94\,\mathrm{kJ/m^3}$. In consideration of the sample volume of $0.7\,\mathrm{cm^3}$, this results in an absolute deformation energy of 0.66 mJ and with respect to the sample mass of $2.69\,\mathrm{cm^3}$ in $0.245\,\mathrm{J/g}$ deformation energy per unit mass. From the theory of bending-dominated lattices and open cell foams, this region is known as the so called densification region in which the opposing sides of the network cells impinge on each other so that finally the cell walls, in this case the hollow graphite tubes of the aerographite network, are compressed themselves. Figure 4.9c shows an ultimate compression at 97 % deformation of a sample with a density of $2.87\,\mathrm{mg/cm^3}$. Here a maximum compressive stress of 18 kPa was observed.

In order to describe the mechanical behaviour of aerographite networks under compression we developed a mathematical model. It is based on a simplified geometry (Figure 4.10a) consisting in a stack of parallel layers formed by aligned individual tetrapods having constant arm length r with the same orientation with respect to the external force. (Figure 4.10b) shows in detail the schematization of a single tetrapod with total initial height H depending on its geometry, namely arm length and dihedral angles, here derived assuming that the tetrapod arm tips are the vertexes of a regular tetrahedron. It is assumed in the model that the external applied load is equally distributed to all tetrapods of each single layer that, thus is constituted by an ensemble of springs connected in parallel. The external force, according to the scheme, is assumed to be equally distributed over the three lower arms ($\Delta F_{\mathrm{ext}}/3$ for $\psi = 0$). The sample compressive strain ε is defined as the ratio between the current variation in sample height Δh with respect to its initial value H:

$$\varepsilon = \frac{\Delta h(\alpha)}{H} = \frac{h_0 - r\cos(\alpha_0 + \Delta\alpha)}{r + r\cos\alpha_0} = \frac{\cos\alpha_0 - \cos(\alpha_0 + \Delta\alpha)}{1 + \cos\alpha_0}. \tag{4.6}$$

Recalling that $\Delta\alpha = \frac{1}{D}|\vec{r}\times\vec{F}| = \frac{M}{D}$ and inserting this expression into Equation (4.6) we get the deformation as a function of the external applied load:

$$\varepsilon = \frac{\cos\alpha_0 - \cos\left(\alpha_0 + \frac{1}{D(\alpha)} r \frac{F_{\mathrm{ext}}}{3}\sin\alpha\right)}{1 + \cos\alpha_0}. \tag{4.7}$$

Now it is possible to compute the the equivalent compressive stress in the network explicating the normal force F_{ext} and normalizing it with respect to the tetrapod projected area $a = \frac{3\sqrt{3}}{4}(r\sin\alpha_0)^2$ (regular tetrahedron geometry assumed):

$$\sigma = \frac{4}{3}\sqrt{3} n D(\alpha) \frac{[\arccos[\varepsilon(1+\cos\alpha_0) - \cos\alpha_0]]}{r^3 \sin^2\alpha_0 \sin\alpha} \tag{4.8}$$

The expression of Equation (4.8) makes the approximation that the buckling is experienced by all tetrapod at the same load level while some statistical distribution of tetrapod geome-

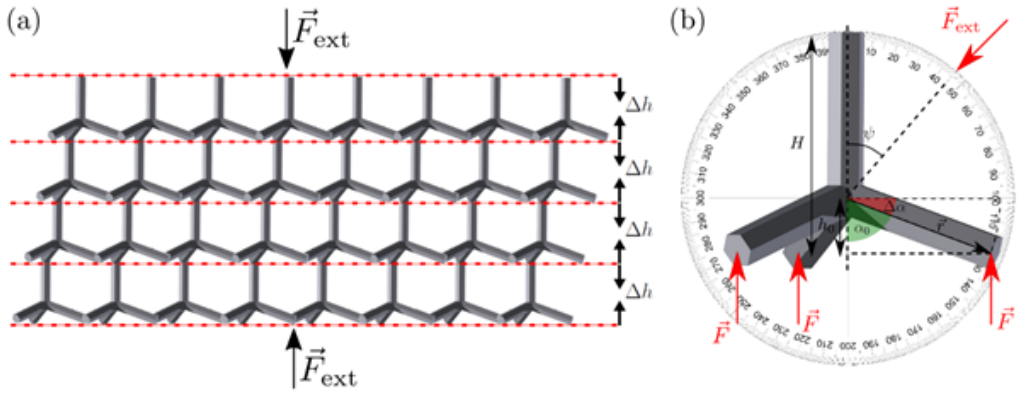

Figure 4.10: Schematic drawing of the undeformed aerographite network used as basis for the mathematical model. (a) The simplified geometry consists of a stack of parallel layers in which all individual tetrapods touch the plane with 3 arms and are oriented in the same direction with respect to the external force. (b) Scheme of single tetrapod with network model parameters.

try and orientation could be inserted. To consider material densification at large strain a stress multiplicative factor n is introduced, which correlates the level of densification to the material compaction quantified by the compressive strain ε:

$$n(\varepsilon) = \frac{\rho_0/\rho_{\min}}{1-\varepsilon} \tag{4.9}$$

where ρ_0 is the density of the network in the undeformed state ($\varepsilon = 0$) while $\rho_{\min}$ is the minimum density allowed for an interconnected network, thus the one corresponding to the model scheme of Figure 4.10. This coherently yields to infinite stress for $\varepsilon \to 1$ that is at null volume, describing the behaviour of foamy networks at large compressive strain.

Figures 4.11- 4.12 show the superposition of the analytical model and FEM simulations result for two for two networks with different densities. Tetrapod geometry was assumed to be the same as the one investigated in the previous section. Stage I corresponds to the elastic deformation of tetrapod and the slope of the stress strain curve is also influenced by mutual sliding, since the high void volume. Then buckling occurs with progressively decrease of the tetrapod stiffness D (central joint) and the curvature of the stress-strain law changes consequently (Stege II), showing a softening behaviour. As the compaction increases there is no room for more tetrapod rotation and transversal crushing of the tube sections starts causing a further reversion of the curvature (stage III) which is followed by material compaction and a high increase in the strain.

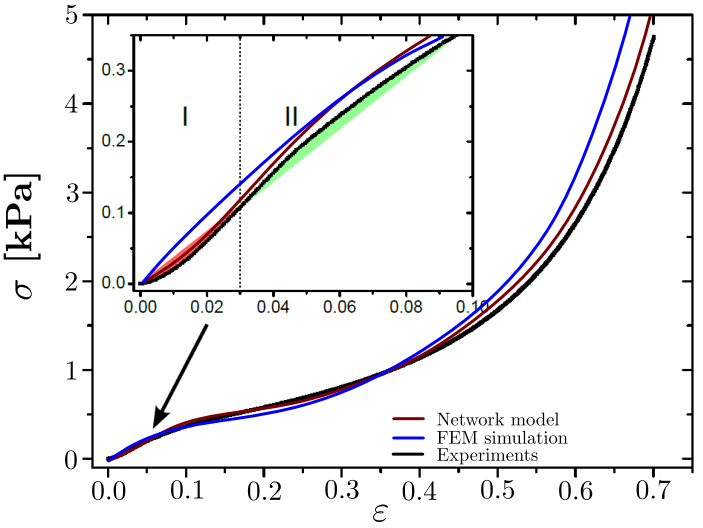

Figure 4.11: Compression test of an aerographite network with a density of 3.84 mg/cm^3.

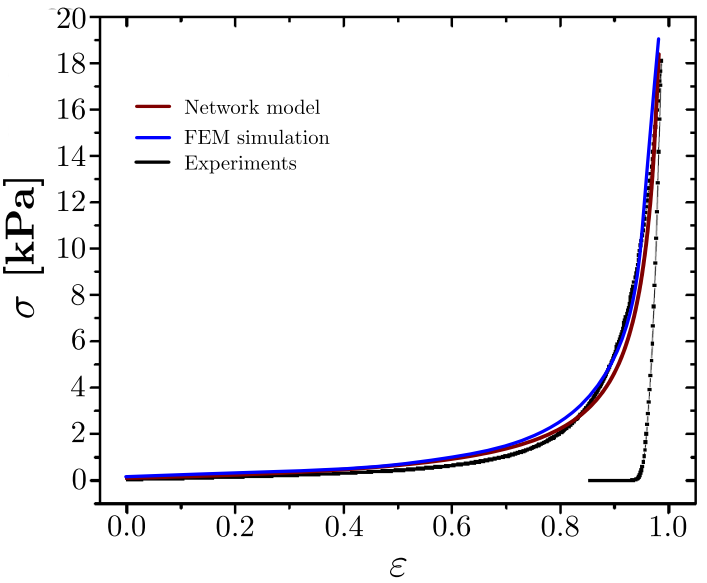

Figure 4.12: Compression test of an aerographite network with a density of 2.86 mg/cm^3.

4.4 Conclusions

Complex shaped hollow nano- and micro-structures, for instance the here considered tetrapods, enable the tunable fabrication of advanced 3D highly porous materials with unique mechanical specific properties. The nonlinear constitutive law of these modular networks is mainly dictated by the mechanical behaviour of the individual network building blocks, which themselves strongly depend upon their morphology. In particular, the mechanics of single hollow AG tetrapods with hollow arms is governed by the buckling-hinge formation at the central joint or along its arms, rather than by the elastic deformation of the arms, as dictated by its thin walls. This mechanism, which clearly emerges from experiments and simulations, is reversible and allows high overall deformation without damage under extreme and cyclic loads, as confirmed and visible by experiments. The developed analytical model, which describes the mechanical behaviour of the tetrapod buckling hinges with three parameters (the arm rotation at buckling onset α_{bh}, the hinge elastic rotational stiffness D and the buckling-hinge parameter γ), represents the essential basis for understanding the mechanical behaviour of AG networks as a whole. We believe that our findings on the dominant deformation mechanisms of individual AG tetrapods can lead to a more profound understanding of the mechanical behaviour of the 3D interconnected t-AG. Moreover, due to the proved generality of the buckling-hinge model, not restricted to the specific geometry, loading and boundary conditions, size scale, and shape of the tetrapod, our work is expected to be useful in the design and optimization of aerogels and foams [155] in different fields, from materials science to scaffold medical engineering.

The nonlinear softening of tetrapods suggests that the relative network under compression may experience an analogous behaviour before its stiffening due to material densification. Indeed, this is in agreement with the experimentally observed behaviour for networks, which shows a change in the sign of the stress–strain curve second derivative (nonlinear softening followed by stiffening) [140]. The good agreement between the modelled and the experimental curves indicates that the network behaviour mainly depends on the mechanical properties of the single tetrapods and their increasing agglomeration during deformation rather than on their random orientation and interconnections. The developed model allows forecasting the mechanical behaviour of aerographite foams with different densities and consisting of differently dimensioned tetrapods (different arm length, tube wall thickness and diameter). This would enables the foresighted tuning of the network fabrication process according to the needs of its envisaged application. Future following works will cover the modelling of the unloading stages and the cyclic loading of these structures.

Chapter 5

Hollow-cylindrical-joint honeycombs for enhanced energy absorption

In this chapter a simulation study on modified honeycomb structures made of a metallic alloy subjected compressive crushing and experiencing yielding, elastic-plastic instability, and fracture is presented. The structures are realized by substituting the joint between the walls of the traditional honeycomb with hollow cylinders of variable radius, which have to be optimized in order to maximize the specific energy absorption of the cellular structure. These structures could be in principle be realized also with other materials, namely traditional composite materials, graphene-based composite, silk-like artificial materials. The sample preparation and experiments were performed by the group of Prof. Qiang Chen, School of Biological Science and Medical Engineering, Southeast University, Nanjing (Popular Republic of China) which is acknowledged for the sharing of the data.

5.1 Introduction

Hollow-cylindrical-joint honeycombs represent a modification of traditional honeycombs where the joint formed by the intersection of converging walls are placed by hollow cylinders (Figure 5.1c). This kind of structure belongs to the family of centre-symmetrical hexagonal honeycombs [156] and has been recently proposed [157, 158] as possible and effective modification of conventional honeycomb structures (Figure 5.1a-b) to further increase their specific elastic mechanical properties, i.e. the yield strength (σ/ρ), and stiffness (E/ρ). It has analytically been proved that these characteristic quantities can be maximized, on an equal mass basis, in relation to specific geometric sizing of the radius r of the cylinders and of the length l of the walls (Figure 5.1). In particular, an optimal (maximum) value of the mechanical properties was analytically predicted for

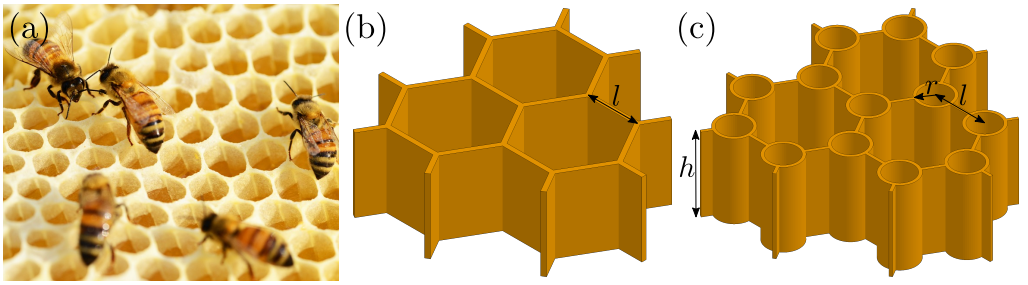

Figure 5.1: From traditional to modified honeycombs. (a) Natural honeycomb structure of a beehive. (b) Reference model of a conventional regular hexagonal honeycomb structure. (c) Model a hollow-cylindrical-joint honeycomb structure. Geometrical characteristics of the honeycombs are identified in the figure, namely the specimen height h, the wall length l and the cylindrical joint radius r.

aspect ratios $r/l \approx 0.3$ [157] (Figure 5.1c).

The proposed analytical models [157] to describe the mechanics of these modified honeycombs are based on geometrical consideration and on the elastic theory of plates and shells and, thus, are limited to the description of the elastic regime up to yielding onset. The high complexity of phenomena within the material, which experiences yielding, elastic-plastic instabilities, and fracture under large strain, in addition to the geometrical non-linearity introduced by the complex 3D geometry, require the use of non-linear simulation in order to thoroughly describe mechanical behaviour of such honeycombs up to crushing. Further advantages are associated with the virtual modelling. The closed cell structure of the honeycombs does not allow to directly visualize the formation and the evolution of plastic folds and fractures during the experiments. Moreover simulations can go beyond the mere measurement of the force displacement curves being able to measure other important quantities such as local stresses and strain (and thus highlight with precision the yielded and damaged regions), to visualize the formation of shear bands, and to precisely control and evaluate the role of different frictional properties (static and dynamic coefficient of friction) at the contact interfaces on the overall behaviour. Scope of the study was the development of a simulation model able to predict the energy absorption capability of such structures and to be use for future studies on further geometries or constituent materials.

5.2 Materials

A series of five specimen with different ratio r/l, from 0 to 0.5, and same mass was experimentally tested, both in the out-of-plane (parallel to the cylinder axes) and in the in-plane directions. The geometrical characteristics of the specimens are reported in Table 5.1.

The sample utilized for this study [158] were made using 6061-T4 aluminum alloy for the bulk constituent material. Defining ρ_h/ρ_{bulk} as the ratio between the honeycomb density and the density of the constituent bulk material this value was selected to be 0.1, being the density of the alloy $\rho_{bulk} = 2.7\,kg/m^3$. The height of the specimens h is 20 mm for the in-plane loaded samples and 30 mm for the out-of plane loaded samples. The distance l between the joints was fixed to be 20 mm for all specimens. Consequently, the theoretical thickness of each samples to keep the specimen mass constant can be calculated as a function of r/l according to the relation $\rho_h/\rho_{bulk} = -1.155\,(t/l)^2 + [2.528\,(t/l) + 1.155]\,(t/l)$ [157].

Table 5.1: Geometric parameters, theoretical (m) and real (m_{re}) masses of the eleven tested samples. The double values for m_{re} of the in-plane loaded samples refer to different samples compressed in the two orthogonal directions (y direction within brackets).

In-plane loaded samples						Out-of-plane loaded samples					
n.	l [mm]	r [mm]	t [mm]	m [g]	m_{re} [g]	n.	l [mm]	r [mm]	t [mm]	m [g]	m_{re} [g]
-	-	-	-	-	-	1	20	0	1.78	41.7	39.6
1	20	4	1.26	59.0	55.8 (53.1)	2	20	4	1.26	41.7	38.9
2	20	6	1.08	59.0	55.0 (52.3)	3	20	6	1.08	41.7	39.8
3	20	8	0.95	59.0	56.7 (53.2)	4	20	8	0.95	41.7	36.5
-	-	-	-	-	-	5	20	10	0.84	41.7	34.6

The monoaxial compression experiments [158] were made with a 1000HDX Instron Universal Testing Machine (ITW, USA) with loading capacity of 1000 kN. The loading rates before and after the initial yield of the samples are of 1 mm/min. We define conventional quantities for describing the constitutive response of the honeycomb. The compressive stress is $\sigma_h = F/A$ where F is the force recorded in the load cell of the testing machine, and A is the projected convex hull area of the honeycomb samples on the plane perpendicular to the loading direction; the corresponding compressive strain is $\varepsilon_h = \Delta h/h$, where Δh is the variation of height of the specimen recorded by the machine. The material properties and stress-strain relationship of the aluminum alloy used in the experiment were characterized by tensioning a round dog-bone specimen with circular cross-section of diameter d = 10 mm up to failure. The determined mechanical properties extracted from the stress-strain curve were: the Young's modulus E = 68 GPa, the yield stress σ_y=287 MPa, the ultimate (peak) stress σ_u=318 MPa, and the failure strain ε_f=0.121. The corresponding constitutive curve is reported in Figure 5.2.

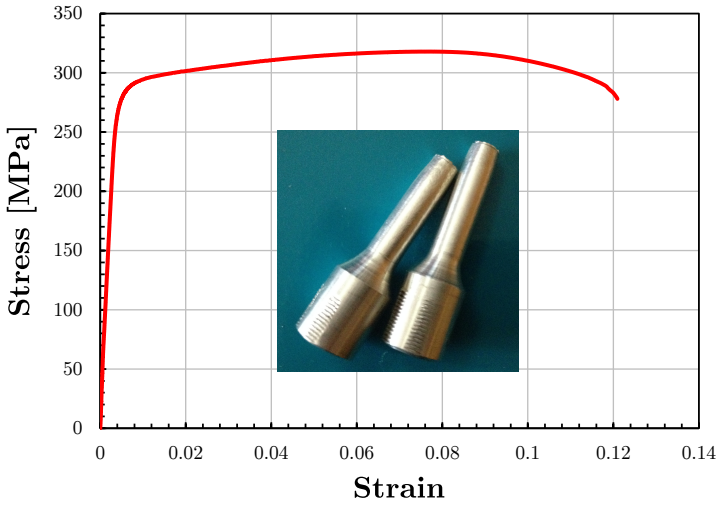

Figure 5.2: Nominal stress-strain curve from tensile test of a dogbone specimen ($d =$ 10 mm) of 6061-T4 aluminum alloy used for the fabrication of the tested honeycombs.

5.3 FEM models

Although the material constitutive law could be approximated with a piecewise linear elastic-plastic relationship, the experimentally derived plastic branch of the curve was directly used as input in the material model. Prior to yielding the material is assumed linear elastic with $\varepsilon_y = \sigma_y/E$. It must be mentioned that in the FEM model, due to the size-scale effect, the plastic strain in the input curve $\varepsilon_{pl} = \varepsilon - \frac{\sigma_y}{E}$ were scaled with respect to the nominal one measured from the dog-bone test by a factor $\frac{\varepsilon_{pl,FEM}}{\varepsilon_{pl}} = \frac{d}{t}$, since is $t \ll d$ for the fabricated specimens. Thus also the ultimate strain $\varepsilon_{f,\,FEM}$ is scaled accordingly. This operation was necessary, otherwise without considering this effect, simulations provide an unnatural brittle behaviour very far from the experiments.

Regarding the choice of elements for this kind of problems, hexaedron 1-point integration solid elements (constant stress) represent an effective solution. This solution is efficient and accurate and works very well for severe deformations. For plasticity problem at least 3 integration points should be present through the minimum dimension of the structure, thus 3 elements of this type should be used through the thickness t. Besides the saving in computational time with respect to the 8-point fully integrated element, this choice may avoid element locking. Hourglass must also be monitored with attention and mitigated, if necessary, for these elements. The use of more element through the thickness may help in this sense. von Mises criterion was employed for yielding. Material fracture is treated via an erosion algorithm with the element that are deleted from simulation when either one between the principal or deviatoric strain reaches the corresponding limit $\varepsilon_{f,FEM}$.

Contact interactions were implemented between the steel plates and the honeycomb. Self-contact within the honeycomb parts was also introduced in order to properly account for material densification during the crushing process. Static and dynamic coefficients of friction were respectively set to be 0.61-0.47 for the honeycomb-rigid steel plate contact and 1.35-1.05 for the self-contact, which are common value for aluminum-steel and aluminum-aluminum surfaces. For the out-of-plane loaded samples the solid element were placed with thin shell element with 5 integration point to the thickness. This solution, much less computationally demanding, is sufficiently accurate to describe the crushing behaviour of the samples loaded in this direction, being the behaviour governed mainly by the bending of the walls [157]. Since the performed simulations are under displacement control and a force is not directly applied, the load F to compute the stress σ_{h} is here extrapolated from the normal component of the contact force at the contact surface between the honeycomb and the steel plate, which by equilibrium is equal to the external applied load.

5.4 Results

5.4.1 In-plane mechanical behaviour

The in-plane mechanical behaviour of the 3 honeycombs compressed in both x and y directions is reported in Figure 5.3. The quantities, namely the stress σ_{h} and the strain ε_{h} from FEM simulations are computed as previously described for experiments. It can be seen that the stress–strain curves generally take on a serrated feature, due to the fracture in cylindrical shells and plates, and the linear-elastic stage (E1) of all samples is very short. The FEM results (dashed line) and experimental results (solid line) are in good agreement, both in terms of curve shape and of honeycomb bearing capacity. The samples 1 and 3 ($r/l = 0.2$, red line and $r/l = 0.4$, blue lines) have only one plateau stage, whereas, the sample 2 ($r/l = 0.3$, green line) has two linear-elastic or plateau stages (Figure 5.3a and b), and the second linear-elastic (E2) and plateau (P2) stages are longer and much shorter than their first counterparts (i.e., E1 and P1), respectively. The sample 2 reaches densification earlier than the samples 1 and 3.

Yield strengths of the three samples in the x direction are 1.11 MPa ($r/l = 0.2$), 1.20 MPa ($r/l = 0.3$), 1.02 MPa ($r/l = 0.4$) for experiments vs. 1.19 MPa, 1.29 MPa, 1.10 MPa for FEM; in the y direction, and they are 1.19 MPa ($r/l = 0.2$), 1.34 MPa ($r/l = 0.3$), 0.96 MPa ($r/l = 0.4$) for experiments vs. 1.28 MPa, 1.42 MPa, 1.10 MPa for FEM. From these data, we see that the yield strengths are optimized when $r/l = 0.3$, which is consistent with the precedent analytical work [157]. Finite element results are slightly greater than the experimental counterparts. Moreover, the yield strength in the x direction is less than that in the y direction, and this is caused by the different structures of the two directions, with the compressed samples in the x direction including the extra axial deformation or instability of the vertical plates. Considering the effect of the mass variations among samples, we here also compare the yield strength to mass ratio $\sigma_{\mathrm{h,y}}/m$,

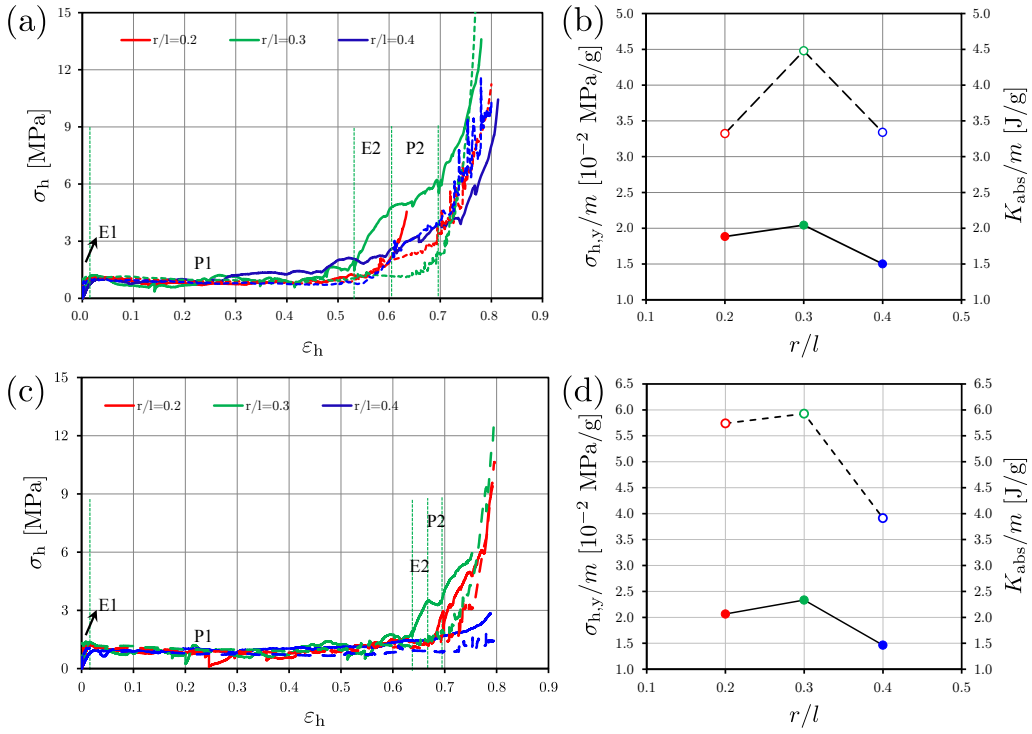

Figure 5.3: Stress-strain curves with different r/l ratios from simulations (dashed lines) and comparison with experimental results (solid lines) of the three samples loaded in (a) x direction and (c) y direction. Yield strength to mass ratio (filled dots) and specific absorbed energy (empty dots) as a function of r/l computed from FEM simulations for samples loaded in (b) x direction and (d) y direction. Results show how the lattice are optimized for $r/l \approx 0.3$ providing the higher yield strength and energy absorption. Experimental data courtesy of Prof. Qiang Chen, Southeast University, Nanjing (Popular Republic of China).

and again the optimal case for both directions corresponds to $r/l = 0.3$ (Figure 5.3c and d). The coherent optimization for both $\sigma_{\mathrm{h,y}}$ and $\sigma_{\mathrm{h,y}}/m$ is due to the little mass difference for each intra-group (x and y directions).

In addition, the large deformations and failure mechanisms (Figure 5.4 and 5.5) in both directions are observed. For the x direction, the samples 1 and 2 (i.e., $r/l = 0.2, 0.3$) have an approximate anti-symmetric configuration (Figure 5.4a and c), thanks to the instability of vertical plates, which have a relative large slenderness ratio, while the sample 3 is nearly symmetric (Figure 5.4e). When the samples fail, the plastic hinges and fracture points locate at the plate-shell connecting points on the plates (points A and B, Figure 5.4g) or on the cylindrical shell (points C, Figure 5.4h), depending on the r/l ratio. This behaviour has already been verified by the theoretical analysis [157]. For the y direction, the three samples share a symmetric configuration (Figure 5.5a,c, and e), but their failures differ as well, since in the samples 1 and 2 (i.e., $r/l = 0.2, 0.3$, respectively) plastic hinges and fractures occur in the two plates (points A in Figure 5.5g), while on the cylindrical shell in the the sample 3 ($r/l = 0.4$, points C in Figure 5.5h). The same occurs in the samples loaded in the x direction. The contours of von Mises stresses from the finite element simulations confirm the results, see Figure 5.4i and Figure 5.5i.

When $r/l \to 0$, the cylindrical shells disappear and the structure shrinks into the conventional regular hexagonal honeycomb, which has been widely studied in literature. Otherwise, when $r/l \to 0.5$, the plates disappear. For the structures in-between, smaller r/l ratio (e.g., sample 1) results in a more rigid cylindrical shells -also due to the higher thickness-, and the in-plane samples fail in the weaker plates due to bending and buckling according to the loading directions. On the contrary, greater r/l (e.g., sample 3) results in a more compliant cylindrical shell, and the samples fail in the weaker cylindrical shell due to their folding. These two cases result in single pair of linear elastic and plastic stages as shown in Figure 5.3a and b. In the intermediate situation, the two parts fail one after the other. This causes the double pairs of linear elastic and plastic stages, E1-P1 and E2-P2 in Figure 5.3a and b: the first one is contributed by the bending and yielding of the plate, and the second by the bending and collapse of the cylindrical shell. In view of this, it can be concluded that it is the featured structure that provides the sample 2 with the optimized failure mechanism and further best energy-absorption ability even though the six experimental samples had approximate mass. In this regard, this hierarchical failure mechanism of different components in the structure is similar to the behaviour of spider silk [159], which enables its great extensibility, toughness and strength.

5.4.2 Out-of-plane mechanical behaviour

Like the in-plane case, the FEM and experimental stress–strain curves the yield strength to mass ratio and the specific absorbed energy of the five out-of-plane samples are plotted in Figure 5.6. When r/l is small (samples 1–3), there is only one couple of peak and valley; while r/l is large (samples 4, 5), there are multi-couples of peak and valley (①-④), and

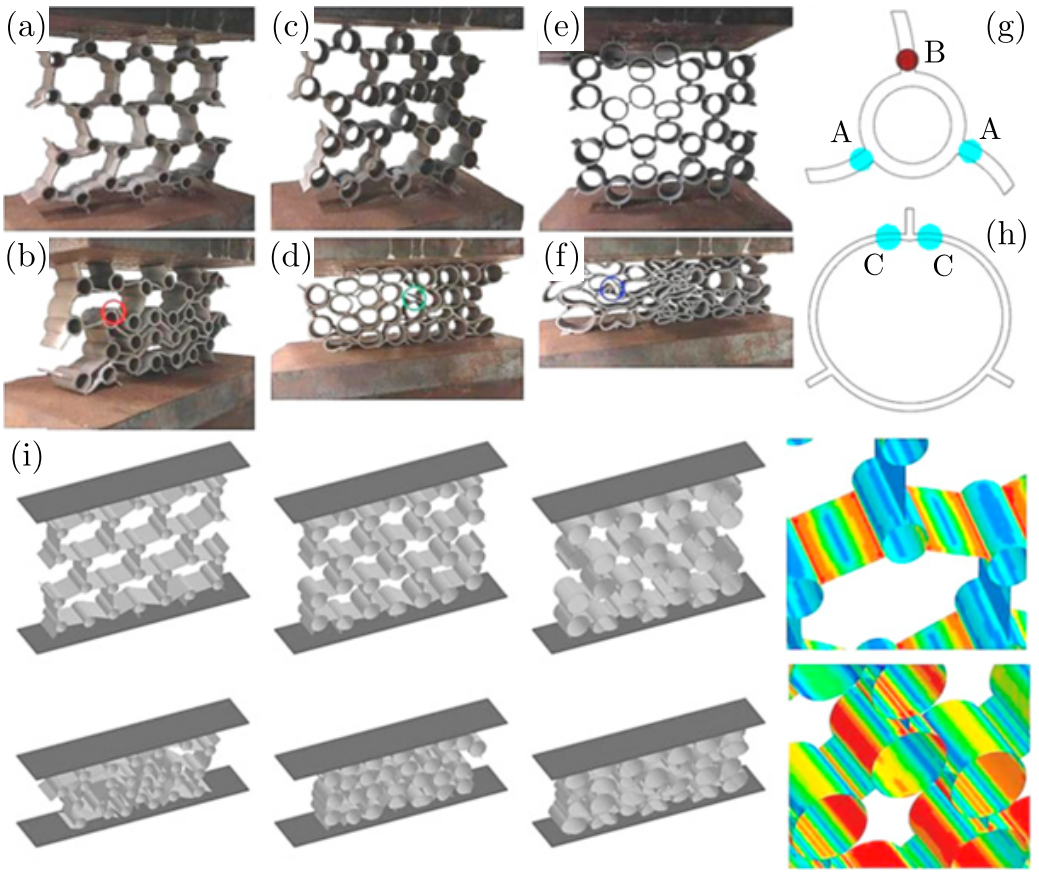

Figure 5.4: Snapshots of the experimental in-plane loaded samples in the x direction with $r/l = 0.2$ (a and b), $r/l = 0.3$ (c and d), $r/l = 0.4$ (e and f) at two different strain levels. (i) Corresponding snapshots from finite element simulations and details of the cylindrical shell-plate joints for different r/l with contour of von Mises stress (red regions are the most stressed). The solid coloured circles in (g and h) indicate the positions of the plastic hinges or fracture locations. Experimental images courtesy of Prof. Qiang Chen, Southeast University, Nanjing (Popular Republic of China).

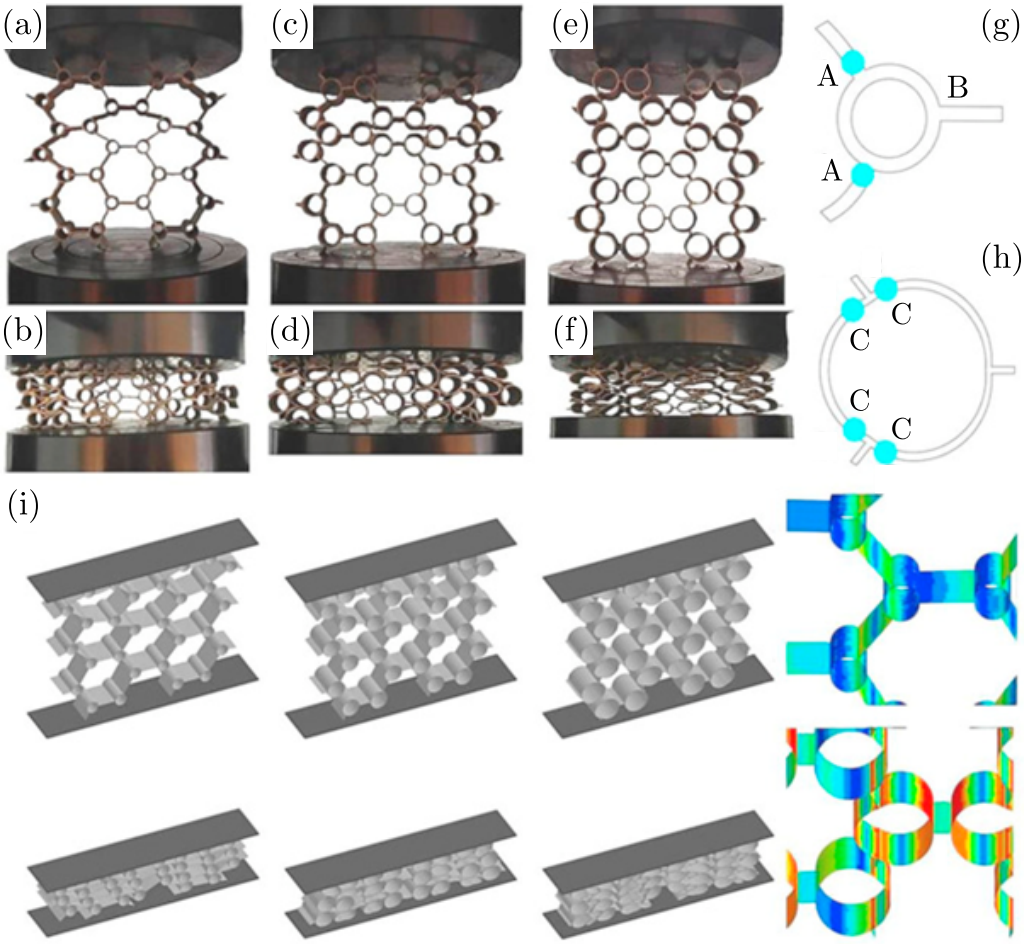

Figure 5.5: Snapshots of the experimental in-plane loaded samples in the y direction with $r/l = 0.2$ (a and b) $r/l = 0.3$ (c and d) $r/l = 0.4$ (e and f) at two different strain levels. (i) Corresponding snapshots from finite element simulations and details of the cylindrical shell-plate joints for different r/l with contour of von Mises stress (red regions are the most stressed). The solid coloured circles in (g and h) indicate the positions of the plastic hinges or fracture locations. Experimental images courtesy of Prof. Qiang Chen, Southeast University, Nanjing (Popular Republic of China).

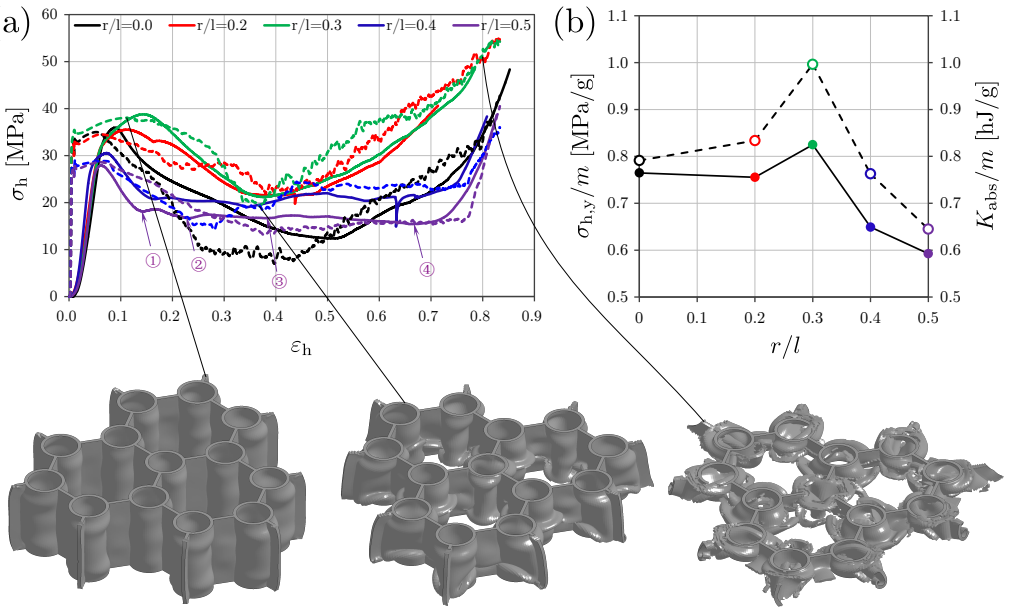

Figure 5.6: (a) Stress-strain curves of the five simulated samples with different r/l ratios (dashed lines) and comparison with experimental results (solid lines). For $r/l = 0.5$ four states are highlighted corresponding to the images of Figure 5.8b. Three simulation states for the optimal honeycomb $r/l = 0.3$ are depicted corresponding to yielding, minimum of bearing capacity and complete fracture. (b) Specific yield strength (filled dots) and absorbed energy (empty dots) as a function of r/l computed from FEM simulations. Results show how the lattice is again optimized for $r/l \approx 0.3$ providing the higher yielding strength and energy absorption. Experimental data courtesy of Prof. Qiang Chen, Southeast University, Nanjing (Popular Republic of China).

the plateau stage is much longer than those of the samples with small r/l, but sample 3 ($r/l = 0.3$) still possesses the greatest energy-absorption capacity (computed as the work done by the external load). Besides, the images of FEM compression test for $r/l = 0.3$ are shown in Figure 5.6. The lattices Young's modulus, computed as $\sigma_{h,y}/\varepsilon_{h,y}$ is nearly constant, in accordance to the fact that the ratio E_h/ρ_h is a material constant [160]. The yield strengths of the five samples are 35.95 MPa ($r/l = 0.0$), 35.46 MPa ($r/l = 0.2$), 38.78 MPa ($r/l = 0.3$), 30.60 MPa ($r/l = 0.4$), 27.81 MPa ($r/l = 0.5$) for experiments vs. 34.99 MPa, 34.51 MPa, 38.06 MPa, 29.09 MPa, 26.80 MPa for finite element simulations. The yield strength of the out-of-plane samples is 20÷30 times those of the in-plane samples. The optimized yield strength is obtained again for $r/l = 0.3$, and the same for the yield strength to mass ratio (Figure 5.6b) due to the weak mass variation of the intra-group (out-of-plane) of real samples.

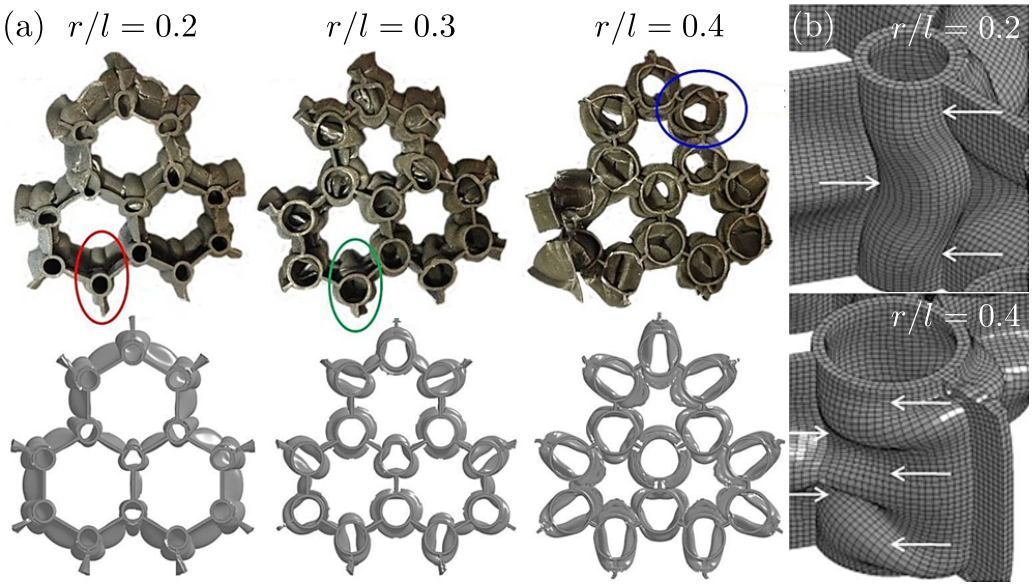

Figure 5.7: (a) Experimental and simulated collapse modes of the out-of-plane loaded honeycomb with r/l=0.2, 0.3, 0.4. (b) Snapshots of FEM simulations (at $\varepsilon_h = 20\%$) showing the collapse mechanisms of the cylindrical shell-plate joint with detail of variable number of foldings for different r/l due to the different level of restrain between cylinders and plates and the different thickness of the honeycombs to provide the same mass. Experimental images courtesy of Prof. Qiang Chen, Southeast University, Nanjing (Popular Republic of China).

The failure mechanisms obtained for the shell-plate assembled honeycombs Figure 5.7 represent a transition between the two limit behaviours of Sample 1 ($r/l = 0$, classical hexagonal honeycomb) and of Sample 5 ($r/l = 0.5$, degenerated plates) shown in Figure 5.8. The classical honeycomb, after the elastic-plastic instability of the plates, which can be approximated with the simple case of the Euler's column with both clamped edges, reaches the failure due to the formation of a sub-horizontal fracture approximately at $h/2$. For the Sample 5, the collapse of the structure is caused by the multiple folding of cylindrical shell and does not experience fracture. For single cylindrical tube, many works explain its collapse mechanisms, according to thickness, diameter and length [161]. From Figure 5.8a it can be seen how simulations are capable to capture the transition between the two limit structures, with increasing number of folds and decreasing fold wavelength as r/l increases. This behaviour can be imputed to the fact that for maintaining the same mass along all specimens the wall thickness t decreases with increasing r/l, yielding towards a more ductile behaviour. Figure 5.8b gives a measure of the capability of simulation to catch large displacement deformation with the simulation deformed shape that can be nearly perfectly superposed to experimental pictures, matching the number of folds. As

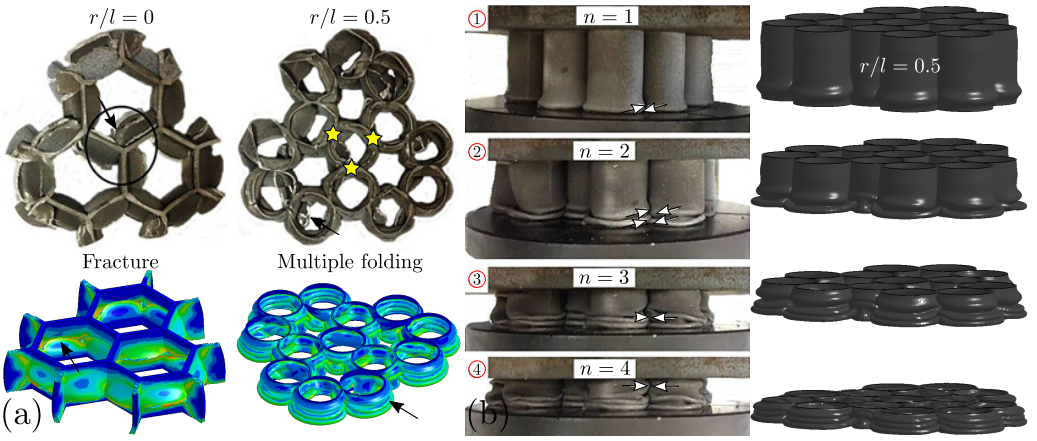

Figure 5.8: (a) Collapse mode transition from Sample 1 ($r/l = 0$, unmodified honeycomb) to Sample 5 ($r/l = 0.5$, full cylindrical joint honeycomb, restrain point between the cylinders highlighted). Contour plot of plastic strain is superposed to simulated honeycombs images. (b) Visual comparison between crushing experiment (left) and simulation (right) on Sample 5 at four deformation levels (encircled labels in Figure 5.6a) showing very good agreement in the formation of folds (highlighted by the arrows) due to elastic-plastic instabilities. For each state the number of formed fold n is indicated. Experimental data courtesy of Prof. Qiang Chen, Southeast University, Nanjing (Popular Republic of China).

an interesting example, four states of the sample 5 assembled only by cylindrical shells without plates are reported, and the sequence of events is shown in Figure 5.8. Initially, the entire sample deforms elastically to the first peak point, i.e., yield stress. Due to the existence of the bottom steel plate, the further expansion of the sample's deformation is restrained by friction, and the first axisymmetric outward fold (n=1) starts to form. As the load increases, the fold of each cylindrical shell grows and it thrusts into its adjacent shells to form an overlap (highlighted by the arrows), while the other parts of the sample still deforms elastically. Simultaneously, the constituent material at the fold begins to yield, and the entire sample shows a softening behaviour. Then, the deformation of the portion close to the fold accumulates. After the contact of the two sides in the fold, the drop of the compressive load arrests. Meanwhile, a new fold (n=2) starts to form, and the second peak stress gradually emerges, followed by the second valley. In state ② the overlaps can be clearly seen. Then, the third and fourth diamond folds (states ③ and ④) are formed by the squeezed cylindrical shells; the stress does not apparently increase until it reaches the densification in state ④, after which, the stress increases sharply.

5.5 Conclusions

The results indicates that the combination of hollow cylindrical shells and plates forms a new periodic assembly with better (maximized) elastic mechanical properties and energy absorption capability with respect to conventional hexagonal honeycombs. As shown, the developed numerical model was able to well describe the experiments, both in predicting the constitutive curves of the honeycomb under in-plane and out-of-plane compression and the energy absorbing capability. Thus, the models could be used in predicting the performance of honeycombs of different geometries, further optimizing natural solutions. This concept is not limited to the present material but may be used to generate new crashworthy lattices at different scales, ranging form macroscopic sandwich panels to material structuring at the nanoscale, also employing biological materials for gaining further toughness [162, 163].

Chapter 6

Conclusions and outlook

In this work finite element method-based numerical models were exploited to investigate the mechanical behaviour of structures subjected to the high-velocity penetration of an impacting mass or to compressive crushing and to study materials of interest for possible application in the sector of impact protection and energy absorption, ranging from nano to macro-scale systems. Scope of this work was to develop computational models to complement and integrate, also in synergy with theory, experiments and physical prototyping in order to propose new and better-optimized solutions for such applications. In this way, it was possible to explore the whole design domain and to overcome the difficulties of experiments in measuring and controlling the physical quantities of interest for a large number of samples and with the required precision, especially when moving towards the smallest dimensional scales. The main results of the present research can be summarized as follows:

- Through finite element simulations and analytical modelling we have studied the ballistic properties of multilayer composite armours, focusing the role of the mechanical properties of the adhesive between the plies on the scaling of the specific absorbed energy with different number of layers. It was demonstrated how the addition of materials, namely increasing the number of layers, it is not always beneficial leading even to sub-optimal configurations. We have shown how the adhesive properties can tune, and also optimize, this scaling allowing a synergistic behaviour between the layers. These results underline the importance of controlling these characteristics in the production process of such multilayer armours. We find that a graded distribution of layers with different material strength in the thickness provide higher protection when the projectile first encounter plies with the higher failure strength, explaining also common structural arrangements of biological armours. Results of the developed numerical and analytical models, in terms of energy absorption and projectile residual velocity, are in good agreement with ballistic experiments and these tools can be effectively used to reliably predict the impact

behaviour of such structures.

- We have extended the investigation of energy scaling to armours at lower dimensional levels by studying the ballistic properties of single and multilayer 2D materials membranes, taking graphene and the hexagonal allotrope of boron nitride (and their mixing) as case studies. A strong synergistic coupling emerges at the nanoscale, which was shown to vanish and invert at the micro- and macro-scale, in accordance with experiments available in literature. This leads to an optimal number of layers, identified between 5 and 10. These results suggest that multilayer 2D materials armours should be structured and optimized at the nano scale, not relying only on the high specific mechanical properties of the constituent materials. These armours, for example, would be particularly effective in providing protection from high energy nanoscopic fragments or even suitable as coating for protection from cavitation erosion. An important outcome of the research is the realization of a finite element continuum model to study the behaviour of these materials at different dimensional scales overcoming the difficulties of *ab initio* methods in modelling large scale systems.

- As 3D structuring of 2D materials for possible energy absorption application, we studied the mechanics of hollow aerographite tetrapods which are the basic building blocks of the related ultralight networks. Finite element simulation were fundamental to interpret and integrate nanoscopic experiments. The virtual study of different tetrapodal geometries allowed the generalization of the constitutive law describing the tetrapod mechanical behaviour, which is governed by the elastic and reversible buckling of the central joint. The single tetrapod model was then extended to investigate the behaviour of aerographite networks. Due to the proved generality of the developed buckling-hinge model, not restricted to the specific geometry, loading and boundary conditions, size scale, and shape of the tetrapod, the results are expected to be useful in the design and optimization of aerogels and foams in different fields, from materials science to scaffold medical engineering.

- As final case study, the investigation of the crushing behaviour under compressive loads of modified honeycombs made of a metallic alloy lead to the proposal of new optimized geometries for maximizing the energy absorption of these structures. Results indicate that the combination of hollow cylindrical shells and plates forms a new periodic assembly with higher specific yield strength and energy absorption capability with respect to conventional hexagonal honeycombs. The developed numerical model was able to match the experiments, predicting the constitutive curves of the honeycomb behaviour under compression and the optimum. These models could be used in predicting the performance of honeycombs of different geometries and materials, further optimizing natural solutions.

Given the promising results, many possibilities are open for future application of these models. Further numerical and physical experiments on these systems be performed, employing different material constitutive laws and structures based on 2D or 3D architectures, also bio-inspired, in order to gain an advance and propose a new generation of protective structures. Although numerical codes become more and more sophisticated, many problems related the accurate prediction of real material behaviour at impact remain to be solved. The introduction of these new materials and concepts arise further concerns regarding the ability of current computational methods to effectively model and predict -at a reasonable computational cost- the impact mechanics of such protective structures, compensating the limit of experimental prototyping. Future modelling and simulation tools will have to be able to treat concurrently and in a unified manner the many failure mechanisms present at impact and penetration, such as dynamic cracking and fragmentation, generation of dislocations and shear bands. Anyhow, it must be mentioned that another crucial limit in the capability of computational analysis for the class of problems discussed here -but also for many others (e.g., fluid dynamics, astrophysics) is the current advance in computational hardware architectures. Indeed, a further and significant push in the capabilities computational analysis, in terms of degrees of freedom of the models, will necessarily require a breakthrough in the hardware conceptions [164]. Anyway, in this work we showed how with the current resources it is possible to obtain significant results in the field if different methods and theory are coupled in a synergistic way, overcoming the current limits in performing truly single-framework multiscale simulations.

Bibliography

[1] L.S. Dimas and M.J. Buehler. Modeling and additive manufacturing of bio-inspired composites with tunable fracture mechanical properties. *Soft Matter*, 10(25):4436–4442, 2014. doi: 10.1039/C3SM52890A.

[2] B. Achrai, B. Bar-On, and H.D. Wagner. Bending mechanics of the red-eared slider turtle carapace. *Journal of the Mechanical Behavior of Biomedical Materials*, 30: 223–233, 2014. doi: http://dx.doi.org/10.1016/j.jmbbm.2013.09.009.

[3] E. Lin, Y. Li, J.C. Weaver, C. Ortiz, and M.C. Boyce. Tunability and enhancement of mechanical behavior with additively manufactured bio-inspired hierarchical suture interfaces. *Journal of Materials Research*, 29(17):1867–1875, 2014. doi: http://dx.doi.org/10.1557/jmr.2014.175.

[4] M. Thielen, C.N.Z. Schmitt, S. Eckert, T. Speck, and R. Seidel. Structure–function relationship of the foam-like pomelo peel (Citrus maxima) - an inspiration for the development of biomimetic damping materials with high energy dissipation. *Bioinspiration & Biomimetics*, 8(2):025001, 2013. doi: http://dx.doi.org/10.1088/1748-3182/8/2/025001.

[5] M. Thielen S.F. Fischer, P. Weiß, R. Seidel, T. Speck, A. Bührig-Polaczek, and M. Bünck. Production and properties of a precision-cast bio-inspired composite. *Journal of Materials Science*, 49(1):43–51, 2014. doi: http://dx.doi.org/10.1007/s10853-013-7878-4.

[6] L. Brely, F. Bosia, and N.M. Pugno. A Hierarchical Lattice Spring Model to Simulate the Mechanics of 2-D Materials-Based Composites. *Frontiers in Materials*, 2(51):64–73, 2015. doi: 10.3389/fmats.2015.00051.

[7] E. Lepore, F. Bonaccorso, M. Bruna, F. Bosia, S. Taioli, G. Garberoglio, A.C. Ferrari, and N.M. Pugno. Silk reinforced with graphene or carbon nanotubes spun by spiders. *ArXiv*, (1504.06751 [cond-mat.mtrl-sci]), 2016. URL `https://arxiv.org/abs/1504.06751`.

[8] N.M. Pugno, F. Bosia, and T. Abdalrahman. Hierarchical fiber bundle model to investigate the complex architectures of biological materials. *Physical Review E*, 85(1):011903, 2012. doi: http://dx.doi.org/10.1103/PhysRevE.85.011903.

[9] MIL-DTL-46593B. DETAIL SPECIFICATION PROJECTILE, CALIBERS .22, .30, .50, AND 20MM FRAGMENT-SIMULATING. Standard, U.S. Army Research Laboratory, Aberdeen Proving Ground, MD 21005-5069, July 2006.

[10] MAS/132-MMS/4090. STANAG 4090 LAND (Edition 2) SMALL ARMS AMMUNITION (9 mm PARABELLUM). Standard, NATO Military Agency for Standardization, 1110 Brussels, Belgium, April 1982.

[11] S. Signetti and N.M. Pugno. Evidence of optimal interfaces in bio-inspired ceramic-composite panels for superior ballistic protection. *Journal of the European Ceramic Society*, 34(11):2823–2831, 2014. doi: http://dx.doi.org/10.1016/j.jeurceramsoc.2013.12.039.

[12] J.H. Lee, P.E. Loya, J. Loeu, and E.L. Thomas. Dynamic mechanical behavior of multilayer graphene via supersonic projectile penetration. *Science*, 346(6213):1092–1096, 2014. doi: http://dx.doi.org/10.1126/science.1258544.

[13] B.Z.G. Haque, C.S.C. Chowdhury, and J.W. Gillespie. Molecular simulations of stress wave propagation and perforation of graphene sheets under transverse impact. *Carbon*, 102:126–140, 2016. doi: http://dx.doi.org/10.1016/j.carbon.2016.02.033.

[14] NASA. International Space Station Risk of Impact from Orbital Debris, 2015. URL `http://www.nasa.gov/externalflash/iss_impact_risk/`.

[15] P.J. Hoog. Composites in Armor. *Science*, 314(5802):1100–1101, 2006. doi: http://dx.doi.org/10.1126/science.1131118.

[16] S. Abrate. Ballistic impact on composites. In *Proceedings of the 16th International Conference on Composite Materials*, volume 26, pages 1–10, Kyoto, Japan, 2007. Japan Society for Composite Materials. doi: http://dx.doi.org/10.13140/2.1.2202.3044.

[17] B.G. Kumar, R.P. Singh, and T. Nakamura. Degradation of Carbon Fiber-Reinforced Epoxy Composites by Ultraviolet Radiation and Condensation. *Journal of Composite Materials*, 36(24):2713–2733, 2002. doi: http://dx.doi.org/10.1177/002199802761675511.

[18] G.S. Springer. *Environmental effects on composite materials*, volume 3. Technomic Publishing Co., 1988.

[19] S. Abrate. *Impact on Composite Structures*. Cambridge University Press, 1th edition, 2001.

[20] P.J. Hazell. *Armour: Materials, Theory and Design*. CRC Press, 2015.

[21] Advances in Ceramic Armor X, 2014. URL `http://eu.wiley.com/WileyCDA/WileyTitle/productCd-1119040604.html`.

[22] W. Liu, Z. Chen, Z. Chen, X. Cheng, Y. Wang, X. Chen, J. Liu, B. Li, and S. Wang. Influence of different back laminate layers on ballistic performance of ceramic composite armor. *Materials & Design*, 87:31–27, 2015. doi: http://dx.doi.org/10.1016/j.matdes.2015.08.024.

[23] C. Lee, X. Wei, J.W. Kysar, and J. Hone. Measurement of the Elastic Properties and Intrinsic Strength of Monolayer Graphene. *Science*, 321(5887):385–388, 2008. doi: http://dx.doi.org/10.1126/science.1157996.

[24] T. Zhang, X. Li, S. Kadkhodaei, and H. Gao. Flaw Insensitive Fracture in Nanocrystalline Graphene. *Nano Letters*, 12(9):4605–4610, 2012. doi: http://dx.doi.org/10.1021/nl301908b.

[25] S.W. Cranford. When is 6 less than 5? Penta- to hexa-graphene transition. *Carbon*, 96:421–428, 2016. doi: http://dx.doi.org/10.1016/j.ijsolstr.2012.05.019.

[26] J-H. Lee, D. Veysse, J.P. Singer, M. Retsch, G. Saini, T. Pezeril, K.A. Nelson, and E.L. Thomas. High strain rate deformation of layered nanocomposites. *Nature Communications*, 3:1164, 2012. doi: http://dx.doi.org/10.1038/ncomms2166.

[27] W. Yang, I.H. Chen, B. Gludovatz, E.A. Zimmermann, R.O. Ritchie, and M.A. Meyers. Natural Flexible Dermal Armour. *Advanced Materials*, 25(1):31–48, 2013. doi: http://dx.doi.org/10.1002/adma.201202713.

[28] W.J. Goldsmith. *Impact - The theory and physics of colliding solids*. Dover Publications, 2nd edition, 2001.

[29] R.F. Recht and T.W. Ipson. Ballistic Perforation Dynamics. *Journal of Applied Mechanics*, 30(3):384–390, 1963. doi: http://dx.doi.org/10.1115/1.3636566.

[30] W. Goldsmith. Non-ideal projectile impact on targets. *International Journal of Impact Engineering*, 22(2–3):95–395, 1999. doi: http://dx.doi.org/10.1016/S0734-743X(98)00031-1.

[31] P.K. Porwal and S.L. Phoenix. Modeling system effects in ballistic impact into multi-layered fibrous materials for soft body armor. *International Journal of Fracture*, 135(1–4):217–249, 2005. doi: http://dx.doi.org/10.1016/S1359-8368(02)00137-3.

[32] C.T. Lim, V.P.W. Shim, and Y.H. Ng. Finite-element modeling of the ballistic impact of fabric armor. *International Journal of Impact Engineering*, 28(1):13–31, 2003. doi: http://dx.doi.org/10.1016/S0734-743X(02)00031-3.

[33] S. Signetti, F. Bosia, and N.M. Pugno. Computational modelling of the mechanics of hierarchical materials. *MRS Bulletin*, 41(9):694–699, 2016. doi: http://dx.doi.org/10.1557/mrs.2016.185.

[34] B. Wang, W. Yang, R. Vincent, R. Sherman, and M.A. Meyers. Pangolin armor: Overlapping, structure, and mechanical properties of the keratinous scales. *Acta Biomaterialia*, 41:60–74, 2016. doi: http://dx.doi.org/10.1016/j.actbio.2016.05.028.

[35] B.J.F. Bruet, J. Song, M.C. Boyce, and C. Ortiz. Materials design principles of ancient fish armour. *Nature Materials*, 7(9):748–756, 2008. doi: http://dx.doi.org/10.1038/nmat2231.

[36] W. Yang, V.R. Sherman, B. Gludovatz, M. Mackey, E.A. Zimmermann, E.H. Chang, E. Schaible, Z. Qin, M.J. Buehler, R.O. Ritchie, and M.A. Meyers. Protective role of Arapaima gigas fish scales: Structure and mechanical behavior. *Acta Biomaterialia*, 5(8):3599–3614, 2014. doi: http://dx.doi.org/10.1016/j.actbio.2014.04.009.

[37] S. Rudykh, M.C. C. Ortiz, and Boyce. Flexibility and protection by design: imbricated hybrid microstructures of bio-inspired armor. *Soft Matter*, 11(13):2547–2554, 2015. doi: http://dx.doi.org/10.1039/c4sm02907k.

[38] E.A. Zimmermann, B. Gludovatz, E. Schaible, N.K.N. Dave, W. Yang, M.A. Meyers, and R.O. Ritchie. Mechanical adaptability of the bouligand-type structure in natural dermal armour. *Nature Communications*, 4:2634, 2013. doi: http://dx.doi.org/10.1038/ncomms3634.

[39] L. Li and C. Ortiz. A natural 3D Interconnected Laminated Composite with Enhanced Damage Resistance. *Advanced Functional Materials*, 25(23):3463–3471, 2015. doi: http://dx.doi.org/10.1002/adfm.201500380.

[40] K.W. Garrett and J.E. Bailey. Multiple transverse fracture in 90° cross-ply laminates of a glass fibre-reinforced polyester. *Journal of Materials Science*, 12(1):157–168, 1977. doi: http://dx.doi.org/10.1007/BF00738481.

[41] J.D. Currey. Mechanical properties and adaptations of some less familiar bony tnumbers. *Journal of the Mechanical Behavior of Biomedical Materials*, 3(5): 357–372, 2010. doi: http://dx.doi.org/10.1016/j.jmbbm.2010.03.002.

[42] F. Barthelat, H. Tang, P.D. Zavattieri, C.-M. Li, and H.D. Espinosa. On the mechanics of mother-of-pearl: A key feature in the material hierarchical structure.

Journal of the Mechanics and Physics of Solids, 55(2):306–337, 2007. doi: http://dx.doi.org/10.1016/j.jmps.2006.07.007.

[43] D. Sen and M.J. Buehler. Structural hierarchies define toughness and defect-tolerance despite simple and mechanically inferior brittle building blocks. *Scientific Reports*, 1:35, 2011. doi: http://dx.doi.org/10.1038/srep00035.

[44] F. Bosia and N.M. Pugno T. Abdalrahman. Investigating the role of hierarchy on the strength of composite materials: evidence of a crucial synergy between hierarchy and material mixing. *Nanoscale*, 4(4):1200–1207, 2012. doi: http://dx.doi.org/10.1039/c2nr11664b.

[45] M.K. Vickaryous and B.K. Hall. Osteoderm morphology and development in the nine-banded armadillo, Dasypus novemcinctus (Mammalia, Xenarthra, Cingulata). *Journal of Morphology*, 267(11):1273–1283, 2006. doi: http://dx.doi.org/10.1002/jmor.10475.

[46] H. Rhee, M.F. Horstemeyer, Y. Hwang, H. Lim, H. El Kadiri, and W. Trim. A study on the structure and mechanical behavior of the terrapene carolina carapace: A pathway to design bio-inspired synthetic composites. *Materials Science and Engineering: C*, 29(8):2333–2339, 2009. doi: http://dx.doi.org/10.1016/j.msec.2009.06.002.

[47] F.J. Vernerey and F. Barthelat. On the mechanics of fishscale structures. *International Journal of Solids and Structures*, 47(17):2268–2275, 2010. doi: http://dx.doi.org/10.1016/j.ijsolstr.2010.04.018.

[48] D. Frenkel and B. Smit. *Understanding Molecular Simulation - From Algorithms to Applications*. Academic Press, 2nd edition, 2002.

[49] T. Frauenheim, G. Seifert, M. Elstner, T. Niehaus, C. Köhler, M. Amkreutz, M. Sternberg, Z. Hajnal, A. Di Carlo, and S. Suhai. Atomistic simulations of complex materials: ground-state and excited-state properties. *Journal of Physics: Condensed Matter*, 14(11):3015–3047, 2002. URL `http://stacks.iop.org/0953-8984/14/i=11/a=313`.

[50] G. Garberoglio and S. Taioli. Modeling flexibility in metal–organic frameworks: Comparison between Density-Functional Tight-Binding and Universal Force Field approaches for bonded interactions. *Microporous and Mesoporous Materials*, 163:215–220, 2012. doi: http://dx.doi.org/10.1016/j.micromeso.2012.07.026.

[51] M. Xu, J.T. Paci, J. Oswald, and T. Belytschko. A constitutive equation for graphene based on density functional theory. *International Journal of Solids and Structures*, 49(18):2582–2589, 2012. doi: http://dx.doi.org/10.1016/j.ijsolstr.2012.05.019.

[52] R. Tatti, L. Aversa, R. Verrucchi, E. Cavaliere, G. Garberoglio, N.M. Pugno, G. Speranza, and S. Taioli. Synthesis of single layer graphene on Cu(111) by C_60 supersonic molecular beam epitaxy. *RSC Advances*, 6(44):37982–37993, 2016. doi: http://dx.doi.org/10.1039/C6RA02274J.

[53] K. Yoon, A. Ostadhossein, and A.D.T. van Duin. Atomistic-scale simulations of the chemomechanical behavior of graphene under nanoprojectile impact. *Carbon*, 99:58–64, 2016. doi: http://dx.doi.org/10.1016/j.carbon.2015.11.052.

[54] S. Pradhan and B.K. Chakrabarti A. Hansen. Failure processes in elastic fiber bundles. *Review of Modern Physics*, 82(1):499–555, 2010. doi: http://dx.doi.org/10.1103/RevModPhys.82.499.

[55] S. Zapperi and H.E. Stanley A. Vespignani. Plasticity and avalanche behaviour in microfracturing phenomena. *Nature*, 388(6643):658–660, 1997.

[56] N.M. Pugno and R.S. Ruoff. Quantized fracture mechanics. *Philosophical Magazine*, 84(27):2829–2845, 2004. doi: http://dx.doi.org/10.1080/14786430412331280382.

[57] Z. Zhang, Y-W. Zhang, and H. Gao. On optimal hierarchy of load-bearing biological materials. *Proceedings of the Royal Society B*, 278(1705):519–525, 2011. doi: http://dx.doi.org/10.1098/rspb.2010.1093.

[58] S. Panzavolta, B. Bracci, C. Gualandi, M.L. Focarete, E. Treossi, K. Kouroupis-Agalou, K. Rubini, F. Bosia, L. Brély, N.M. Pugno, V. Palermo, and A. Bigi. Structural reinforcement and failure analysis in composite nanofibers of graphene oxide and gelatin. *Carbon*, 78:566–577, 2014. doi: http://dx.doi.org/10.1016/j.carbon.2014.07.040.

[59] L.S. Dimas, G.H. Bratzel, I. Eylon, and M.J. Buehler. Tough Composites Inspired by Mineralized Natural Materials: Computation, 3D Printing, and Testing. *Advanced Functional Materials*, 23(36):4629–4638, 2013. doi: http://dx.doi.org/10.1002/adfm.201300215.

[60] F. Bosia and N.M. Pugno T. Abdalrahman. Self-healing of hierarchical materials. *Langmuir*, 30(4):1123–1133, 2014. doi: http://dx.doi.org/10.1021/la403497z.

[61] T. Belytschko, W.K. Liu, B. Moran, and K. Elkhodary. *Nonlinear Finite Elements for Continua and Structures*. John Wiley & Sons, 2nd edition, 2013.

[62] P. Wriggers. *Computational Contact Mechanics*. Springer-Verlag Berlin Heidelberg, 2nd edition, 2006.

[63] J.O. Hallquist, G.L. Goudreau, and D.J. Benson. Sliding interfaces with contact-impact in large-scale Lagrangian computations. *Computer Methods in Applied Mechanics and Engineering*, 51(1):107–137, 1985. doi: http://dx.doi.org/10.1016/0045-7825(85)90030-1.

[64] P.M. Cuniff. Dimensionless parameters for optimization of textile-based body armor systems. In *Proceedings of the 18th International Symposium of Ballistics (San Antonio, TX, USA)*, pages 1303–1310, 1999.

[65] P.M. Cuniff. Analysis of the system effects in woven fabrics under ballistic impact. *Textile Research Journal*, 62(9):495–509, 1992. doi: http://dx.doi.org/10.1177/004051759206200902.

[66] T. Belytschko, J.S.-J. Ong, W.K. Liu, and J.M. Kennedy. Hourglass control in linear and nonlinear problems. *Computer Methods in Applied Mechanics and Engineering*, 43(3):251–276, 1984. doi: http://dx.doi.org/10.1016/0045-7825(84)90067-7.

[67] S.A. Silling. Reformulation of elasticity theory for discontinuities and long-range forces. *Journal of the Mechanics and Physics of Solids*, 48(1):175–209, 2000. doi: http://dx.doi.org/10.1016/S0022-5096(99)00029-0.

[68] S.A. Silling and E. Askari. A meshfree method based on the peridynamic model of solid mechanics. *Computers & Structures*, 83(17–18):1526–1535, 2005. doi: http://dx.doi.org/10.1016/j.compstruc.2004.11.026.

[69] Sandia National Laboratories. LAMMPS Molecular Dynamics Simulator, 2015. URL `http://lammps.sandia.gov/`.

[70] M.L. Parks, R.B. Lehoucq, S.J. Plimpton, and S.A. Silling. Implementing peridynamics within a molecular dynamics code. *Computer Physics Communications*, 179(11):777–783, 2008. doi: http://dx.doi.org/10.1016/j.cpc.2008.06.011.

[71] S.A. Silling and F. Bobaru. Peridynamic modeling of membranes and fibers. *International Journal of Non-Linear Mechanics*, 40(2–3):395–409, 2005. doi: http://dx.doi.org/10.1016/j.ijnonlinmec.2004.08.004.

[72] J. Lee, W. Liu, and J-W. Hong. Impact fracture analysis enhanced by contact of peridynamic and finite element formulations. *International Journal of Impact Engineering*, 87:108–119, 2016. doi: http://dx.doi.org/10.1016/j.ijimpeng.2015.06.012.

[73] J.L. Zinszner, P. Forquin, and G. Rossiquet. Experimental and numerical analysis of the dynamic fragmentation in a SiC ceramic under impact. *International Journal of Impact Engineering*, 76:9–19, 2015. doi: http://dx.doi.org/10.1016/j.ijimpeng.2014.07.007.

[74] L. Li and C. Ortiz. Pervasive nanoscale deformation twinning as a catalyst for efficient energy dissipation in a bioceramic armour. *Nature Materials*, 10(1): 501–507, 2014. doi: http://dx.doi.org/10.1038/nmat3920.

[75] M.E. Backman and W. Goldsmith. The mechanics of penetration of projectile into targets. *International Journal of Engineering Science*, 16(1):1–99, 1978. doi: http://dx.doi.org/10.1016/0020-7225(78)90002-2.

[76] Z. Guoqi, W. Goldsmith, and C.K.H. Dharan. Penetration of laminated Kevlar by projectiles-II. Analytical model. *International Journal of Solids and Structures*, 29 (4):421–436, 1992. doi: http://dx.doi.org/10.1016/0020-7683(92)90208-B.

[77] B. Parga-Landa and F. Hernández-Olivares. An analytical model to predict impact behaviour of soft armours. *International Journal of Impact Engineering*, 16(3): 455–466, 1995. doi: http://dx.doi.org/10.1016/0734-743X(94)00054-Z.

[78] S.L. Phoenix and P.K. Porwal. A new membrane model for the ballistic impact response and V_50 performance of multi-ply fibrous systems. *International Journal of Solids and Structures*, 40(24):6723–6765, 2003. doi: http://dx.doi.org/10.1016/S0020-7683(03)00329-9.

[79] B. Gu. Analytical modeling for the ballistic perforation of planar plain-woven fabric target by projectile. *Composites Part B: Engineering*, 34(4):361–371, 2003. doi: http://dx.doi.org/10.1016/S1359-8368(02)00137-3.

[80] J. López-Puente, R. Zaera, and C. Navarro. An analytical model for high velocity impacts on thin {CFRPs} woven laminated plates. *International Journal of Solids and Structures*, 44(9):2837–2851, 2007. doi: http://dx.doi.org/10.1016/j.ijsolstr.2006.08.022.

[81] M. Mamivand and G.H. Liaghat. A model for ballistic impact on multi-layer fabric targets. *International Journal of Impact Engineering*, 37(7):806–812, 2010. doi: http://dx.doi.org/10.1016/j.ijimpeng.2010.01.003.

[82] P. Hubert and A. Pousartip. Aspects of the Compaction of Composite Angle Laminates: An Experimental Investigation. *Journal of Composite Materials*, 35(2): 1–26, 2001. doi: http://dx.doi.org/10.1177/002199801772661849.

[83] N.V. Banichuk, S.Y. Ivanova, and E.V. Makeev. On the penetration of nonaxisymmetric bodies into a deformable solid medium and their shape optimization. *Mechanics of Solids*, 43(4):671–677, 2008. doi: 10.3103/S0025654408040158.

[84] M.J. Forrestal and D.Y. Tzou. A spherical cavity-expansion penetration model for concrete targets. *International Journal of Solids and Structures*, 34(31–32): 4127–4146, 1997. doi: http://dx.doi.org/10.1016/S0020-7683(97)00017-6.

[85] G. Ben-Dor, A. Dubinsky, and T. Elperin. High-speed Penetration Modeling and Shape Optimization of the Projectile Penetrating into Concrete Shields. *Mechanics Based Design of Structures and Machines*, 37(4):538–549, 2009. doi: http://dx.doi.org/10.1080/15397730903272830.

[86] M.J. Forrestal, B.S. Altman, J.D. Cargile, and S.J. Hanchak. An empirical equation for penetration depth of ogive-nose projectiles into concrete targets. *International Journal of Impact Engineering*, 15(4):395–405, 1994. doi: http://dx.doi.org/10.1016/0734-743X(94)80024-4.

[87] A.A. Griffith. The Phenomena of Rupture and Flow in Solids. *Philosophical Transaction of the Royal Society of London*, 221:163–198, 1921. doi: http://dx.doi.org/10.1098/rsta.1921.0006.

[88] MATWEB - Material Property Data, 2014-08-24. URL `http://www.matweb.com/Search/MaterialGroupSearch.aspx?GroupID=84`.

[89] A. Carpinteri and N.M. Pugno. Are scaling laws on strength of solids related to mechanics or to geometry? *Nature materials*, 43(6):421–423, 2005. doi: http://dx.doi.org/10.1038/nmat1408.

[90] A. Matzenmiller, J. Lubliner, and R.L. Taylor. A constitutive model for anisotropic damage in fiber-composites. *Mechanics of Materials*, 20(2):125–152, 1995. doi: http://dx.doi.org/10.1016/0167-6636(94)00053-0.

[91] M.A. Iqbal, A. Diwakar, A. Rajput, and N.K. Gupta. Influence of projectile shape and incidence angle on the ballistic limit and failure mechanism of thick steel plates. *Theoretical and Applied Fracture Mechanics*, 62:40–53, 2012. doi: http://dx.doi.org/10.1016/j.tafmec.2013.01.005.

[92] M.J.N. Jacobs and J.L.J. Van Dingenen. Ballistic protection mechanisms in personal armour. *Journal of Materials Science*, 36(13):3137–3142, 2001. doi: http://dx.doi.org/10.1023/A:1017922000090.

[93] G. Anagnostopoulos, P-N. Pappas, Z. Li, I.A. Kinloch, R.J. Young, K.S. Novoselov, C.Y. Lu, N.M. Pugno, J. Parthenios, C. Galiotis, and K. Papagelis. Mechanical Stability of Flexible Graphene-Based Displays. *ACS Applied Materials & Interfaces*, 8(34):22605–22614, 2016. doi: http://dx.doi.org/10.1021/acsami.6b05227.

[94] J-H. Lee, D. Veysse, J.P. Singer, M. Retsch, G. Saini, T. Pezeril, K.A. Nelson, and E.L. Thomas. High strain rate deformation of layered nanocomposites. *Nature Communications*, 3(1164):1–7, 2012. doi: http://dx.doi.org/10.1038/ncomms2166.

[95] C. Androulidakis, E.N. Koukara, O. Frank, G. Tsoukleri, D. Sfyris, J. Parthenios, N.M. Pugno, K. Papagelis, K.S. Novoselov, and C. Galiotis. Failure Processes in Embedded Monolayer Graphene under Axial Compression. *Scientific Reports*, 4: 5271, 2014. doi: http://dx.doi.org/10.1038/srep05271.

[96] T. Ramanathan, A.A. Abdala, S. Stankovich, D.A. Dikin, M. Herrera-Alonso, R.D. Piner, D.H. Adamson, H.C. Schniepp, X. Chen, R.S. Ruoff, S.T. Nguyen, I.A. Aksay, R.K. Prud'Homme, and L.C. Brinson. Functionalized graphene sheets for polymer nanocomposites. *Nature Nanotechnology*, 3(6):327–331, 2008. doi: http://dx.doi.org/10.1038/nnano.2008.96.

[97] P. Umari, O. Petrenko, S. Taioli, and M.M. De Souza. Electronic band gaps of semiconducting zig-zag carbon nanotubes from many-body perturbation theory calculations. *The Journal of Chemical Physics*, 136(18):181101, 2012. doi: http://dx.doi.org/10.1063/1.4716178.

[98] S. Taioli, P. Umari, and M.M. De Souza. Electronic properties of extended graphene nanomaterials from GW calculations. *Physica Status Solidi B*, 246(11-12):2572–2576, 2009. doi: http://dx.doi.org/10.1038/srep05271.

[99] I.N. Kholmanov, C.W. Magnuson, R. Piner, J.Y. Kim, A.E. Aliev, C. Tan, T.Y. Kim, A.A. Zakhidov, G. Sberveglieri, R.H. Baughman, and R.S. Ruoff. Optical, Electrical, and Electromechanical Properties of Hybrid Graphene-Carbon Nanotube Films. *Advanced Materials*, 27(19):3053–3059, 2015. doi: http://dx.doi.org/10.1002/adma.201500785.

[100] C. Chen, J.Z. Wu, K.T. Lam, G. Hong, M. Gong, B. Zhang, Y. Lu, A.L. Antaris, S. Diao, J. Guo, and H. Dai. Graphene Nanoribbons Under Mechanical Strain. *Advanced Materials*, 27(2):303–309, 2015. doi: http://dx.doi.org/10.1002/adma.201403750.

[101] A.F. Ávila, A.S. Neto, and H. Nascimento. Hybrid nanocomposites for mid-range ballistic protection. *International Journal of Impact Engineering*, 38(8–9):669–676, 2011. doi: http://dx.doi.org/10.1016/j.ijimpeng.2011.03.002.

[102] Q. Peng, W. Ji, and S. De. Mechanical properties of the hexagonal boron nitride monolayer: Ab initio study. *Computational Materials Science*, 56:11–17, 2012. ISSN 0927–0256. doi: http://dx.doi.org/10.1016/j.commatsci.2011.12.029.

[103] R.C. Cooper, C. Lee, C.A. Marianetti, X. Wei, J. Hone, and J.W. Kysar. Nonlinear elastic behavior of two-dimensional molybdenum disulfide. *Physical Review B*, 87 (3):035423, 2013. doi: http://dx.doi.org/10.1103/PhysRevB.87.035423.

[104] N.M. Pugno. A general shape/size-effect law for nanoindentation. *Acta Materialia*, 55(0):1947–1953, 2007. doi: http://dx.doi.org/10.1016/j.actamat.2006.10.053.

[105] N.M. Pugno. Dynamic Quantized Fracture Mechanics. *International Journal of Fracture*, 140(0):159–168, 2006. doi: http://dx.doi.org/10.1007/s10704-006-0098-z.

[106] G. Garberoglio, N.M. Pugno, and S. Taioli. Gas Adsorption and Separation in Realistic and Idealized Frameworks of Organic Pillared Graphene: A Comparative Study. *The Journal of Physical Chemistry C*, 119(4):1970–1978, 2016. doi: http://dx.doi.org/10.1021/jp511953p.

[107] C.K. Liang M.J. Eller, S. Della-Negra, A.B. Clubb, H. Kim, A.E. Young, and E.A. Schweikert. Hypervelocity nanoparticle impacts on free-standing graphene: A sui generis mode of sputtering. *The Journal of Chemical Physics*, 142(4):044308, 2015. doi: http://dx.doi.org/10.1063/1.4906343.

[108] E.D. Wetzel, R. Balu, and T.D. Beaudet. A theoretical consideration of the ballistic response of continuous graphene membranes. *Journal of the Mechanics and Physics of Solids*, 99(82):23–31, 2015. doi: http://dx.doi.org/10.1016/j.jmps.2015.05.008.

[109] S. Signetti, S. Taioli, and N.M. Pugno. Hybrid 2D materials multilayer armours. *Submitted*.

[110] O. Hod. Graphite and Hexagonal Boron-Nitride have the Same Interlayer Distance. Why? *Journal of Chemical Theory and Computation*, 8(4):1360–1369, 2012. doi: http://dx.doi.org/10.1021/ct200880m.

[111] N. Pugno, F. Marino, and A. Carpinteri. Towards a periodic table for the nanomechanical properties of the elements. *International Journal of Solids and Structures*, 43(18):5647–5657, 2006. doi: http://dx.doi.org/10.1016/j.ijsolstr.2005.12.003.

[112] L. Boldrin, F. Scarpa, R. Chowdhury, and S. Adhikari. Effective mechanical properties of hexagonal boron nitride nanosheets. *Nanotechnology*, 22(50):505702, 2011. URL `http://stacks.iop.org/0957-4484/22/i=50/a=505702`.

[113] L.Y. Jiang, Y. Huang, H. Jiang, G. Ravichandran, H. Gao, K.C. Hwang, and B. Liu. A cohesive law for carbon nanotube/polymer interfaces based on the van der waals force. *Journal of the Mechanics and Physics of Solids*, 54(11):2436–2452, 2006. doi: http://dx.doi.org/10.1016/j.jmps.2006.04.009.

[114] B. Sachs, T.O. Wehling, M.I. Katsnelson, and M.I. Lichtenstein. Adhesion and electronic structure of graphene on hexagonal boron nitride substrates. *Physical Review B*, 84(19):195414, 2011. doi: http://dx.doi.org/10.1103/PhysRevB.84.195414.

[115] L.A Girifalco and R.S. Lee M. Hodak. Carbon nanotubes, buckyballs, ropes, and a universal graphitic potential. *Physical Review B*, 62(19):13104–13110, 2000. doi: http://dx.doi.org/10.1103/PhysRevB.62.13104.

[116] N. Thamwattana and J.M. Hill. Nanotube bundle oscillators: Carbon and boron nitride nanostructures. *Physica B: Condensed Matter*, 404(21):3906–3910, 2009. doi: http://dx.doi.org/10.1016/j.physb.2009.07.140.

[117] G.B. Adams, M. O'Keeffe, and R.S. Ruoff. Van der waals surface areas and volumes of fullerenes. *The Journal of Physical Chemistry*, 98(38):9465–9469, 1994. doi: http://dx.doi.org/10.1021/j100089a018.

[118] J. Wu, B. Wang, Y. Wei, R. Yang, and M. Dresselhaus. Mechanics and Mechanically Tunable Band Gap in Single-Layer Hexagonal Boron-Nitride. *Materials Research Letters*, 1(4):200–206, 2013. doi: http://dx.doi.org/10.1080/21663831.2013.824516.

[119] S.-L. Chen and Z.-L. Zheng. Large deformation of circular membrane under the concentrated force. *Applied Mathematics and Mechanics*, 24(1):28–31, 2003. doi: http://dx.doi.org/10.1007/BF02439374.

[120] N.M. Pugno. The role of defects in the design of space elevator cable: From nanotube to megatube. *Acta Materialia*, 55(15):5269–5279, 2007. ISSN 1359-6454. doi: http://dx.doi.org/10.1016/j.actamat.2007.05.052.

[121] H. Wang, K. Sun, F. Tao, D.J. Stacchiola, and Y.H. Hu. 3d Honeycomb-Like Structured Graphene and Its High Efficiency as a Counter-Electrode Catalyst for Dye-Sensitized Solar Cells. *Angewandte Chemie International Edition*, 52(35):9210–9214, 2013. doi: http://dx.doi.org/10.1002/anie.201303497.

[122] B.G. Choi, M.-H. Yang, W.H. Hong, J.W. Choi, and Y.S. Huh. 3d macroporous Graphene Frameworks for Supercapacitors with High Energy and Power Densities. *ACS Nano*, 6(5):4020–4028, 2012. doi: http://dx.doi.org/10.1021/nn3003345.

[123] O. Parlak, A.P.F. Turner, and A. Tiwari. On/Off-Switchable Zipper-Like Bioelectronics on a Graphene Interface. *Advanced Materials*, 26(3):482–486, 2014. doi: http://dx.doi.org/10.1002/adma.201303075.

[124] M.A. Correa-Duarte, N. Wagner, J. Rojas-Chapana, C. Morsczeck, M. Thie, and M. Giersig. Fabrication and Biocompatibility of Carbon Nanotube-Based 3D Networks as scaffolds for cell seeding and growth. *Nano Letters*, 4(11):2233–2236, 2004. doi: http://dx.doi.org/10.1021/nl048574f.

[125] J. Xu, Z. Tan, W. Zeng, G. Chen, S. Wu, Y. Zhao, K. Ni, Z. Tao, M. Ikram, H. Ji, and Y. Zhu. A hierarchical carbon derived from sponge-templated activation of graphene oxide for high-performance supercapacitor electrodes. *Advanced Materials*, 28(26): 5222–5228, 2016. doi: http://dx.doi.org/10.1002/adma.201600586.

[126] H. Sun, Z. Xu, and C. Gao. Multifunctional, ultra-flyweight, synergistically assembled carbon aerogels. *Advanced Materials*, 25(18):2554–2560, 2013. doi: http://dx.doi.org/10.1002/adma.201204576.

[127] A.K. Geim and K.S. Novoselov. The rise of graphene. *Nature Materials*, 6(3): 183–191, 2013. doi: http://dx.doi.org/10.1038/nmat1849.

[128] M.A. Worsley, S.O. Kucheyev, H.E. Mason, M.D. Merrill, B.P. Mayer, J. Lewicki, C.A. Valdez, M.E. Suss, M. Stadermann, P.J. Pauzauskie, J.H. Satcher, J. Biener, and T.F. Baumann. Mechanically robust 3d graphene macroassembly with high surface area. *Chemical Communications*, 48(67):8428–8430, 2012. doi: http://dx.doi.org/10.1039/C2CC33979J.

[129] S. Yin, Z. Niu, and X. Chen. Assembly of graphene sheets into 3d macroscopic structures. *Small*, 8(16):2458–2463, 2012. doi: http://dx.doi.org/10.1002/smll.201102614.

[130] Y. Zhao, C. Hu, Y. Hu, H. Cheng, G. Shi, and L. Qu. A versatile, ultralight, nitrogen-doped graphene framework. *Angewandte Chemie International Edition*, 51(45):11371–11375, 2012. doi: http://dx.doi.org/10.1002/anie.201206554.

[131] P.M. Sudeep, T.N. Narayanan, A. Ganesan, M.M. Shaijumon, H. Yang, S. Ozden, P.K. Patra, R. Vajtai M. Pasquali, S. Ganguli, A.K. Roy, M.R. Anantharaman, and P.M. Ajayan. Covalently interconnected three-dimensional graphene oxide solids. *ACS Nano*, 7(8):7034–7040, 2013. doi: http://dx.doi.org/10.1021/nn402272u.

[132] S. Nardecchia, D. Carriazo, M.L. Ferrer, M.C. Gutierrez, and F. del Monte. Three dimensional macroporous architectures and aerogels built of carbon nanotubes and/or graphene: synthesis and applications. *Chemical Society Review*, 42(2): 794–830, 2013. doi: http://dx.doi.org/10.1039/C2CS35353A.

[133] A. Schuchardt, Y.K. Mishra T. Braniste, M. Deng, M. Mecklenburg, M.A. Stevens-Kalceff, S. Raevschi, K. Schulte, L. Kienle, R. Adelung, and I. Tiginyanu. Three-dimensional aerographite-gan hybrid networks: Single step fabrication of porous and mechanically flexible materials for multifunctional applications. *Scientific Reports*, 5:8839, 2013. doi: http://dx.doi.org/10.1038/srep08839.

[134] K.H. Kim, Y. Oh, and M.F. Islam. Graphene coating makes carbon nanotube aerogels superelastic and resistant to fatigue. *Nature Nanotechnology*, 7(9):562–566, 2015. doi: http://dx.doi.org/10.1038/nnano.2012.118.

[135] Z. Lin, X. Gui, Q. Gan, W. Chen, X. Cheng, M. Liu, Y. Zhu, Y. Yang, A. Cao, and Z. Tang. In-situ welding carbon nanotubes into a porous solid with super-high compressive strength and fatigue resistance. *Scientific Reports*, 5:11366, 2015. doi: http://dx.doi.org/10.1038/srep11336.

[136] Y.K. Mishra, S. Kaps, A. Schuchardt, I. Paulowicz, X. Jin, D. Gedamu, S. Freitag, M. Claus, S. Wille, A. Kovalev, S.N. Gorb, and R. Adelung. Fabrication of Macroscopically Flexible and Highly Porous 3D Semiconductor Networks from Interpenetrating Nanostructures by a Simple Flame Transport Approach. *Particle & Particle Systems Characterization*, 30(9):775–783, 2013. doi: http://dx.doi.org/10.1002/ppsc.201300197.

[137] Y.K. Mishra, S. Kaps, A. Schuchardt, I. Paulowicz, X. Jin, D. Gedamu, S. Wille, O. Lupan, and R. Adelung. Versatile fabrication of complex shaped metal oxide nano-microstructures and their interconnected networks for multifunctional applications. *KONA Powder and Particle Journal*, 31:92–110, 2014. doi: http://dx.doi.org/10.14356/kona.2014015.

[138] Y.K Mishra, G. Modi, V. Cretu, V. Postica, O. Lupan, T. Reimer, I. Paulowicz, V. Hrkac, W. Benecke, L. Kienle, and R. Adelung. Direct growth of freestanding zno tetrapod networks for multifunctional applications in photocatalysis, uv photodetection, and gas sensing. *ACS Applied Materials & Interfaces*, 7(26): 14303–14316, 2015. doi: http://dx.doi.org/10.1021/acsami.5b02816.

[139] V. Postica, J. Gröttrup, R. Adelung, O. Lupan, A.K. Mishra, N.H. de Leeuw, N. Ababii, J.F.C. Carreira, J. Rodrigues, N.B. Sedrine, M.R. Correia, T. Monteiro, and Y.K Mishra V. Sontea. Multifunctional materials: A case study of the effects of metal doping on zno tetrapods with bismuth and tin oxides. *Advanced Functional Materials*, 27(6):1604676, 2017. doi: http://dx.doi.org/10.1002/adfm.201604676.

[140] M. Mecklenburg, A. Schuchardt, Y.K. Mishra, S. Kaps, R. Adelung, A. Lotnyk, L. Kienle, and K. Schulte. Aerographite: Ultra Lightweight, Flexible Nanowall, Carbon Microtube Material with Outstanding Mechanical Performance. *Advanced Materials*, 24(26):3486–3490, 2012. doi: http://dx.doi.org/10.1002/adma.201200491.

[141] I. Tiginyanu, L. Ghimpu, J. Gröttrup, V. Postolache, M. Mecklenburg, M.A. Stevens-Kalceff, V. Ursaki, N. Payami, R. Feidenhansl, K. Schulte, R. Adelung, and Y.K. Mishra. Strong light scattering and broadband (UV to IR) photoabsorption in stretchable 3D hybrid architectures based on Aerographite decorated by ZnO nanocrystallites. *Scientific Reports*, 6:32913, 2016. doi: http://dx.doi.org/10.1038/srep32913.

[142] R. Meija, S. Signetti, A. Schuchardt, K. Meurisch, D. Smazna, M. Mecklenburg, K. Schulte, D. Erts, O. Lupan, B. Fiedler, Y.K. Mishra, R. Adelung., and N.M.

Pugno. Nanomechanics of individual aerographite tetrapods. *Nature Communications*, 8:14982, 2017. doi: http://dx.doi.org/10.1016/j.carbon.2016.10.034.

[143] G. Cao and X. Chen. Buckling of single-walled carbon nanotubes upon bending: Molecular dynamics simulations and finite element method. *Physical Review B*, 73 (15):155435, 2006. doi: http://dx.doi.org/10.1103/PhysRevB.73.155435.

[144] L. Jasulaneca, R. Meija, A.I. Livshits, J. Prikulis, S. Biswas, J.D. Holmes, and D. Erts. Determination of Young's modulus of Sb_2S_3 nanowires by in situ resonance and bending methods. *Beilstein Journal of Nanotechnology*, 7:278–283, 2016. doi: 10.3762/bjnano.7.25.

[145] N.T. Ngo, D. Almécija, J.E. Sader, B. Daly, N. Petkov, J.D. Holmes, D. Erts, and J.J. Boland. Ultimate-Strength Germanium Nanowires. *Nano Letters*, 6(12):2964–2968, 2006. doi: http://dx.doi.org/10.1021/nl0619397.

[146] B. Wu, A. Heidelberg, and J.J. Boland. Mechanical properties of ultrahigh-strength gold nanowires. *Nature Materials*, 4(7):525–529, 2007. doi: http://dx.doi.org/10.1038/nmat1403.

[147] L.G. Brazier. On the Flexure of Thin Cylindrical Shells and Other Thin Sections. *Proceedings of the Royal Society of London A: Mathematical, Physical and Engineering Sciences*, 116(773):104–114, 1927. doi: http://dx.doi.org/10.1098/rspa.1927.0125.

[148] R. Hill. *The Mathematical Theory of Plasticity*. Oxford University Press, 2008.

[149] N.M Pugno. Young's modulus reduction of defective nanotubes. *Applied Physics Letters*, 90(4):043106, 2007. doi: http://dx.doi.org/10.1063/1.2425048.

[150] M-F. Yu, O. Lourie, M.J. Dyer, K. Moloni, and and R.S. Ruoff T.F. Kelly. Strength and Breaking Mechanism of Multiwalled Carbon Nanotubes Under Tensile Load. *Science*, 287(5453):637–640, 2000. doi: http://dx.doi.org/10.1126/science.287.5453.637.

[151] D.A. Dikin, S Stankovich, E.J. Zimney, R.D. Piner, G.H.B. Dommett, G. Evmenenko, S.T. Nguyen, and R.S. Ruoff. Preparation and characterization of graphene oxide paper. *Nature*, 448(7153):457–460, 2007. doi: http://dx.doi.org/10.1038/nature06016.

[152] M.R. Falvo, G.J. Clary, R.M. Taylor, V. Chi, S. Washburn F.P. Brooks, and R. Superfine. Bending and buckling of carbon nanotubes under large strain. *Nature*, 389 (6651):582–584, 1997. doi: http://dx.doi.org/10.1038/39282.

[153] B.I. Yakobson, C.J. Brabec, and J. Bernholc. Nanomechanics of Carbon Tubes: Instabilities beyond Linear Response. *Physical Review B*, 76(14):2511–2514, 1996. doi: http://dx.doi.org/10.1103/PhysRevLett.76.2511.

[154] D. Zaccaria, D. Bigoni, G. Noselli, and D. Misseroni. Structures buckling under tensile dead load. *Proceedings of the Royal Society A*, 467(2130):1686–1700, 2011. doi: http://dx.doi.org/10.1098/rspa.2010.0505.

[155] A. Pedrielli, S. Taioli, G. Garberoglio, and N.M. Pugno. Designing graphene based nanofoams with nonlinear auxetic and anisotropic mechanical properties under tension or compression. *Carbon*, 111:796–806, 2017. doi: http://dx.doi.org/10.1016/j.carbon.2016.10.034.

[156] W. Miller, C.W. Smith, F. Scarpa, and K.E. Evans. Flatwise buckling optimization of hexachiral and tetrachiral honeycombs. *Composites Science and Technology*, 70 (7):1049–1056, 2010. doi: http://dx.doi.org/10.1016/j.compscitech.2009.10.022.

[157] Q. Chen, N.M. Pugno, K. Zhao, and Z. Li. Mechanical properties of a hollow-cylindrical-joint honeycomb. *Composite Structures*, 109:68–74, 2014. doi: http://dx.doi.org/10.1016/j.compstruct.2013.10.025.

[158] Q. Chen, Q. Shi, S. Signetti, F. Sun, Z. Li, F. Zhu, S. He., and N.M. Pugno. Plastic collapse of cylindrical shell-plate periodic honeycombs under uniaxial compression: experimental and numerical analyses. *International Journal of Mechanical Sciences*, 111–112:125–133, 2016. doi: http://dx.doi.org/10.1016/j.ijmecsci.2016.03.020.

[159] T. Giesa, M. Arslan, N.M. Pugno, and M.J. Buehler. Nanoconfinement of Spider Silk Fibrils Begets Superior Strength, Extensibility, and Toughness. *Nano Letters*, 11(11):5038–5046, 2011. doi: http://dx.doi.org/10.1021/nl203108t.

[160] L.J. Gibson and M.F. Ashby. *Cellular Solids - Structure and Properties*. Cambridge University Press, 2nd edition, 1999.

[161] K.R.F. Andrews, G.L. England, and E. Ghani. Classification of the axial collapse of cylindrical tubes under quasi-static loading. *International Journal of Mechanical Sciences*, 25(9–10):687–696, 1983. doi: http://dx.doi.org/10.1016/0020-7403(83)90076-0.

[162] S. Nedjari, G. Schlatter, and A. Hébraud. Thick electrospun honeycomb scaffolds with controlled pore size. *Materials Letters*, 142:180–183, 2015. doi: http://dx.doi.org/10.1016/j.matlet.2014.11.118.

[163] M.B. Applegate, J. Coburn, B.P. Partlow, J.E. Moreau, J.P. Mondia, B. Marelli, D.L. Kaplan, and F.G. Omenetto. Laser-based three-dimensional multiscale micropatterning of biocompatible hydrogels for customized tnumber engineering scaffolds.

Proceedings of the National Academy of Sciences, 112(39):12052–12057, 2015. doi: http://dx.doi.org/10.1073/pnas.1509405112.

[164] A. de Touzalin, C. Marcus, F. Heijman, I. Cirac, R. Murray, and T. Calarco. Quantum Manifesto - A New Era of Technology, 2016. URL `http://qurope.eu/manifesto`.

The mechanics of impacts is not yet well understood due to the complexity of materials behaviour under extreme stress and strain conditions and is thus of challenge for fundamental research, as well as relevant in several areas of applied sciences and engineering. The involved complex contact and strain-rate dependent phenomena include geometrical and materials non-linearities, such as wave and fracture propagation, plasticity, buckling, and friction. The theoretical description of such non-linearities has reached a level of advance maturity only singularly, but when coupled -due to the severe mathematical complexity- remains limited. Moreover, related experimental tests are difficult and expensive, and usually not able to quantify and discriminate between the phenomena involved. In this scenario, computational simulation emerges as a fundamental and complementary tool for the investigation of such otherwise intractable problems. The aim of this PhD research was the development and use of computational models to investigate the behaviour of materials and structures undergoing simultaneously extreme contact stresses and strain-rates, and at different size and time scales. We focused on basic concepts not yet understood, studying both engineering and bio-inspired solutions. In particular, the developed models were applied to the analysis and optimization of macroscopic composite and of 2D-materials-based multilayer armours, to the buckling-governed behaviour of aerographite tetrapods and of the related networks, and to the crushing behaviour under compression of modified honeycomb structures. As validation of the used approaches, numerical-experimental-analytical comparisons are also proposed for each case.

Stefano Signetti received the Master's degree *cum laude* in Civil Engineering in 2013 from the Politecnico di Torino, Italy. He is also an alumnus of the Alta Scuola Politecnica programme (VII cycle, 2011-2012). He then moved to the University of Trento, Italy, to undertake the PhD studies, which covered the computational modelling of the mechanics of bio-inspired and graphene-based materials and structures under extreme load conditions. He has practiced traditional japanese martial arts for more than twenty years. He is also a mountain, astrophysics and amateur radio enthusiast.